NTNU
Norwegian University of
Science and Technology

Turbomachinery design for Rankine cycles in waste heat recovery applications

Roberto Agromayor Otero

Natural Gas Technology
Submission date: June 2017
Supervisor: Lars Olof Nord, EPT

Norwegian University of Science and Technology
Department of Energy and Process Engineering

NTNU
Norwegian University
of Science and Technology

Department of Energy
and Process Engineering

EPT-M-2017-03

MASTER THESIS

for

Student Roberto Agromayor Otero

Spring 2017

Turbomachinery design for Rankine cycles in waste heat recovery applications

Background and objective

Large amounts of industrial surplus heat are currently unutilized around the globe. Waste heat recovery has therefore the potential of being a major factor in reaching national and international energy and environment goals. Direct use of the heat, for example in a district heating system, could be the most efficient and cost-effective alternative, but is in many cases not a feasible option. Thus, heat-to-power conversion often becomes the most attractive alternative. Electricity has very high flexibility for distribution and re-use.

The thesis work involves a detailed study of turbine designs for Rankine cycles. Specifically, the application should be geared towards waste heat recovery in industry. It will build on the working fluid screening and process simulations in the specialization project.

The main objective of the work is to develop a 1D model for expander technology applicable for the cycles that were analyzed in the specialization project.

The following tasks are to be considered:

1. Literature study on turbomachinery design methods.
2. Selection of turbine technology (radial inflow, radial outflow, axial, hybrid).
3. Develop a 1D mean-line turbine model, preferably in MATLAB.
4. Identify research challenges in turbine design for waste heat recovery applications using natural working fluids. The identified challenges can be analyzed during PhD studies.

Within 14 days of receiving the written text on the master's thesis, the candidate shall submit a research plan for his project to the department.

When the thesis is evaluated, emphasis is put on processing of the results, and that they are presented in tabular or graphic form in a clear manner, and that they are analyzed carefully.

The thesis should be formulated as a research report with summary, conclusion, literature references, table of contents, etc. During the preparation of the text, the candidate should make an effort to produce a well-structured and easily readable report. In order to ease the evaluation of the thesis, it is important that the cross-references are correct. In the making of the report, strong emphasis should be placed on both a thorough discussion of the results and an orderly presentation.

The candidate is requested to initiate and keep close contact with his/her academic supervisor(s) throughout the working period. The candidate must follow the rules and regulations of NTNU as well as passive directions given by the Department of Energy and Process Engineering.

Risk assessment of the candidate's work shall be carried out according to the department's procedures. The risk assessment must be documented and included as part of the final report. Events related to the candidate's work adversely affecting the health, safety or security, must be documented and included as part of the final report. If the documentation on risk assessment represents a large number of pages, the full version is to be submitted electronically to the supervisor and an excerpt is included in the report.

Pursuant to “Regulations concerning the supplementary provisions to the technology study program/Master of Science” at NTNU §20, the Department reserves the permission to utilize all the results and data for teaching and research purposes as well as in future publications.

The final report is to be submitted digitally in DAIM. An executive summary of the thesis including title, student's name, supervisor's name, year, department name, and NTNU's logo and name, shall be submitted to the department as a separate pdf file. Based on an agreement with the supervisor, the final report and other material and documents may be given to the supervisor in digital format.

☐ Work to be done in lab (Water power lab, Fluids engineering lab, Thermal engineering lab)
☐ Field work

Department of Energy and Process Engineering, 17 January 2017

Lars O. Nord
Academic Supervisor

Research Advisor:

Abstract

Rankine Cycles are an effective and efficient manner to convert waste thermal energy into power. Numerous fluids can be used in Rankine cycles, including water, hydrocarbons, hydrofluorocarbons, siloxanes, alcohols or even mixtures of fluids. The performance of Rankine cycles is highly dependent on the optimization of the operating conditions and the design of its components. The expander is, perhaps, the most important component of the Rankine cycle, as it is the device where the energy of the working fluid is converted into mechanical work. There are several expander technologies available, including axial, radial, and hybrid turbines, as well as positive displacement machines. The performance of Rankine cycles is greatly influenced by the efficiency of the expander and, as a result, the optimization of the expander is one of the critical tasks for the design of Rankine cycles.

This work is focused on simple and recuperated Rankine cycles using axial turbines. A waste heat recovery case study was proposed, where the heat source is a 10 kg/s mass flow rate of hot air at 250 °C (with a low temperature limit of 100 °C) and the heat sink is liquid water at 10 °C. 80 pure substances from the REFPROP library were considered as possible working fluids and a screening methodology was developed for the selection of the working fluid. In addition, methodologies for the optimization of simple and recuperated Rankine cycles and axial turbines of any number of stages were developed and implemented in MATLAB.

These methodologies were applied to the case study to find optimal Rankine cycles and axial turbine designs in order to identify possible research challenges within Rankine cycles and turbomachinery for waste heat recovery applications. In particular, it was found that the low speed of sound poses a challenge for the turbine design and that the usual assumption of using axial repeating stages may lead to unfeasible designs for the cases where the volume ratio across the turbine is high.

Acknowledgements

I would like to thank my main supervisor, Professor Lars Olof Nord, for his continuous trust and support and for allowing me to work independently, helping me to find my own path. I have high hopes for our achievements in the years to come, but none of them would be possible if it was not for your interest and openness the first day that I met you and asked you to be the supervisor of my Specialization Project.

I would also like to mention Professor Bernhard Müller and Professor Reidar Kristoffersen, who introduced me to the world of Computational Fluid Dynamics. Your teaching methods may be regarded as the polar opposite of each other, but I reckon that both are complementary and the knowledge I gained in your courses has been essential for my education here at NTNU. You have changed the way I look at many topics, including fluid dynamics (computational or otherwise), differential equations, and numerical methods.

I cannot forget to thank Brede Hagen, Geir Skaugen, Peter Nekså, and Trond Andersen, the SINTEF researchers involved in the COPRO project with whom I had interesting discussions and enjoyable trips. Special thanks goes to Geir Skaugen for his advice and guidance. Your knowledge of optimization and equations of state has helped me to overcome some of the challenges that I faced during this Master Thesis.

I want to thank Ángel Alvarez Pardiñas and Eduardo Liz Marzán for their friendship and for all the advice that they have given me to the present day and that they will most likely give me in the future.

Furthermore, I want to thank my friend David Pérez Piñeiro. Your fresh eagerness to learn and your ever so watchful standpoint against complacency has inspired me to give the best version of myself raise my goals in life.

Special thanks go to my dear friend Jairo Rúa Pazos for his friendship, for the time spent in fruitful discussions about science and engineering, and most importantly, for dealing with me during these last two years in Trondheim. I have great expectations for the next three years doing our PhDs at NTNU (I told you about it, didn't I?), but I hope that our friendship will last much longer than that.

Finally, I would like to thank my parents for their support and for showing interest in my work and life constantly. You have always believed in me and motivated me to reach the point where I am now and you will surely help me to fly even higher in the years to come.

Table of Contents

List of Tables

List of Figures

Nomenclature

Symbols

$\bar{R}$	Universal gas constant	8.3144598 kJ/kmol·K
$\dot{E}$	Exergy flow rate	W
$\dot{m}$	Mass flow rate	kg/s
$\dot{Q}$	Heat flow rate	W
$\dot{W}$	Power	W
Ma	Mach number	–
Re	Reynolds number	–
$\tilde{s}$	Specific entropy predicted from a loss correlation	kJ/kg·K
A	Area	m^2
a	Speed of sound	m/s
B	Tip clearance loss empirical parameter	–
c	Blade chord	m
c_{eq}	Vector of equality constraints	
c_{ineq}	Vector of inequality constraints	
c_p	Isobaric heat capacity	kJ/kg·K
c_v	Isochoric heat capacity	kJ/kg·K
d_s	Specific diameter	–
e	Specific exergy	kJ/kg
f	Objective function	
f_{Ma}	Mach number correction factor	–
f_{Re}	Reynolds number correction factor	–
f_{AR}	Aspect ratio correction factor	–
f_{hub}	Hub Mach number correction factor	–

H	Blade height	m
h	Specific enthalpy	kJ/kg
H/b	Blade axial aspect ratio	–
H/c	Blade aspect ratio	–
I	Rothalpy	kJ/kg
i	Incidence angle	rad or $^\circ$
K_1	First compressibility correction factor	–
K_2	Second compressibility correction factor	–
K_3	Third compressibility correction factor	–
K_p	Profile loss compressibility correction factor	–
K_s	Secondary loss compressibility correction factor	–
l	Blade camber length	m
lb	Vector of lower bounds for the degrees of freedom	
M	Molecular mass	kg/kmol
n	Number of stages	–
o	Opening	m
p	Pressure	kPa or bar
R	Gas constant or degree of reaction	kJ/kg·K or –
r_h/r_t	Blade hub to tip radii ratio	–
s	Specific entropy or blade spacing	kJ/kg·K or m
s/b	Blade spacing to axial chord ratio	–
s/c	Blade spacing to chord ratio	–
ss	Stage spacing	m
T	Temperature	K or $^\circ$C
t	Blade thickness	m
t_{cl}	Clearance gap thickness	m
t_{max}	Blade maximum thickness	m
t_{te}	Blade trailing edge thickness	m

u	Specific internal energy or blade speed	kJ/kg or m/s
ub	Vector of upper bounds for the degrees of freedom	
v	Absolute flow velocity	m/s
w	Specific work or relative flow velocity	kJ/kg or m/s
x	Vector of degrees of freedom	
Y	Pressure loss coefficient	–
Y_{cl}	Tip clearance loss coefficient	–
Y_p	Profile loss coefficient	–
Y_{shock}	Leading edge shock correction factor	–
Y_s	Secondary loss coefficient	–
Y_{te}	Trailing edge loss coefficient	–
y_{te}	Trailing edge loss multiplication factor	–
Z	Compressibility factor or Ainley loading parameter	–
z	Number of blades of the stage	–

Greek Letters

α	Absolute flow angle	rad or °
β	Relative flow angle	rad or °
$\Delta\phi^2$	Kinetic energy loss coefficient	–
$\Delta T'$	Minimum temperature difference in a heat exchanger	K or °C
Δ	Increment	
δ	Deviation angle	rad or °
δ_{fl}	Flaring angle	rad or °
$\eta_{I\,plant}$	First law plant efficiency	–
$\eta_{I\,cycle}$	First law cycle efficiency	–
$\eta_{I\,recov}$	Heat recovery efficiency	–
$\eta_{II\,plant}$	Second law plant efficiency	–
$\eta_{II\,cycle}$	Second law cycle efficiency	–

$\eta_{II\,recov}$	Exergy recovery efficiency	–
$\eta_{polytropic}$	Polytropic efficiency of turbine or pump	–
η_{ts}	Total-to-static efficiency	–
η_{tt}	Total-to-total efficiency	–
γ	Heat capacity ratio	–
λ	Secondary loss parameter of the AM loss system	–
μ	Dynamic viscosity	Pa·s
ω	Angular speed	rad/s
ω_s	Specific speed	–
ϕ	Flow coefficient	–
ψ	Helmholtz energy or work coefficient	kJ/kg or –
ρ	Density	kg/m^3
σ	Stage solidity	–
τ	Torque	N·m
θ	Blade metal angle	rad or $^\circ$
ξ	Stagger angle	rad or $^\circ$
ζ	Energy loss coefficient	–

Acronyms

AM	Ainley-Methieson loss system
AMDC	Dunham-Came modification to the AM loss system
AMDCKO	Kacker-Okapuu modification to the AMDC loss system
BWR	Back Work Ratio
CFC	Chlorofluorocarbon
CFD	Computational Fluid Dynamics
EOS	Equation Of State
GWP	Global Warming Potential
HCFC	Hydrochlorofluorocarbon

HEOS	Helmholtz (energy explicit) Equations Of State
HFC	Hydrofluorocarbon
HFO	Hydrofluoroolefin
NPSH	Net Positive Suction Head
ODE	Ordinary Differential Equation
ODP	Ozone Depletion Potential
ORC	Organic Rankine cycle
PFC	Perfluorocarbon
PR	Peng-Robinson equation of state
SKR	Soave-Redlich-Kwong equation of state
SQP	Sequential Quadratic Programming

Subscripts

0	Stagnation state
$0, rel$	Relative stagnation state
1	Section at the inlet of the stator
2	Section between the stator and rotor
3	Section at the outlet of the rotor
θ	Tangential (circumferential) velocity component
c	Heat sink (cold)
$cond$	Relative to the condenser
$crit$	Critical property
$evap$	Relative to the evaporator (primary heat exchanger)
exp	Relative to the expander
f	Working fluid
h	Heat source (hot)
in	State at the inlet of the turbine
liq	Liquid saturation property

m	Meridional velocity component
o	Dead state (exergy)
out	State at the outlet of the turbine
$pump$	Relative to the pump
R	Rotor row
r	Radial velocity component or reduced property
S	Stator row
s	Isentropic process
sat	Saturation property
$turb$	Relative to the turbine
vap	Vapor saturation property
x	Axial velocity component

Chapter 1

Introduction

1.1 Project background

This Master Thesis is one of the requirements for the completion of my integrated PhD programme in Engineering at the Department of Energy and Process Engineering, NTNU. This work is part of the KPN project (ENERGIX): Competitive Power Production from Industrial Surplus Heat – COPRO, led by SINTEF Energy Research in collaboration with the NTNU. I wrote this Master thesis under the supervision of associate professor Lars Olof Nord (main supervisor), professor Bernhard Müller, and professor Petter Nekså.

1.2 Motivation

Large amounts of industrial surplus thermal energy are not being utilized around the globe. For this reason, waste heat recovery has the potential of being a major factor in reaching national and international energy and environmental goals. Direct use of the thermal energy, for example in a district heating system, could be the most efficient and cost-effective alternative, but, in many cases, it is not a feasible option. Thus, heat-to-power conversion often becomes the most attractive alternative.

The conversion of waste heat into power is accomplished through a thermodynamic cycle that drives a turbine to generate electrical power. Electricity has high flexibility for distribution and re-use. The optimization of thermodynamic cycles and turbomachinery for waste heat recovery applications is a complex and interesting area or research with a great potential to increase energy efficiency in industrial processes.

1.3 Objectives

The objectives of this project are:

1. Perform a literature study on working fluids, cycle layouts, and turbine technologies for waste heat recovery applications.

2. Develop a screening methodology for the selection of the working fluid.

3. Select a a thermodynamic cycle layout and develop a steady-state cycle optimization program in MATLAB.
4. Select a turbine technology and develop an algebraic mean-line turbine optimization program in MATLAB.
5. Analyze a waste heat recovery case study, find a suitable working fluid, and optimize the thermodynamic cycle and turbine technology.
6. Identify research challenges in turbine design for waste heat recovery applications. These challenges may be analyzed during the PhD.

1.4 Organization

This project comprises four chapters (including this introduction) and one appendix. This section summarizes the contents of each chapter and it intends to serve as a road map.

The technical background of waste heat recovery including a motivation for the use of Rankine cycles is given in Chapter 2. In addition, a description of Rankine cycle configurations, components, and working fluids is included. After this, the thermodynamics of the expansion in Rankine cycles are covered, focusing on real gas effects and the speed of sound along the expansion. Then, a motivation for the selection of axial turbines as expander technology is given and the fundamentals of axial turbines, the main loss mechanisms, and the correlations used to estimate them are discussed. The chapter is finished with a section covering the fundamentals of optimization that is relevant for the optimization of Rankine cycles and axial turbines.

The waste heat recovery case study considered in this work is described in Chapter 3. In addition, the methodologies used for the fluid screening and for the Rankine cycle and axial turbine optimization are presented. The optimization methodologies focus on the variables selected as degrees of freedom, the definition of the objective function, and the optimization constraints. The algorithms used to simulate and optimize Rankine cycles and axial turbines are explained in detail.

In Chapter 4 the methodologies for the fluid screening, Rankine cycle optimization, and turbine optimization are applied to the case study. In particular, the results for two illustrative examples, a simple-saturated cycle using hexane as working fluid with a three-stage axial turbine and a recuperated-transcritical cycle using R152a as working fluid with a two-stage axial turbine, are discussed in detail. In addition, two sensitivity analyses are included, one for the impact of the turbine efficiency on the cycle performance and the other for the impact of the number of stages in the turbine design . The chapter is finished with a section summarizing the main research challenges identified in this work, an evaluation of the objectives set out in the previous section, and a proposal of future research lines within turbomachinery for Rankine cycles in waste heat recovery applications.

Finally a small database with information of all the fluids considered in this work is included in Appendix A. The fluid screening methodology is based on the information contained in this database.

Chapter 2

Technical background

2.1 Climate change and energy trends

Energy is one of the most valuable resources in our society and the energy consumed worldwide does not cease to increase year after year. Despite the strong motivation to increase the amount of energy obtained from renewable sources, in 2014 more than 85% of the primary energy consumption still came from the combustion of fossil fuels responsible for the emission of large amounts of carbon dioxide. The energy consumption and CO_2 emissions in the world are shown in Fig. 2.1 and Fig. 2.2, respectively. The data of these graphs was obtained from the U.S Energy Information Administration (2016).

As detailed in Nord (2010), a solid scientific consensus indicates that the global warming is unequivocal and that it is caused by the increased concentration of greenhouse effect gases. These gases include carbon dioxide, methane and nitrous oxide, but carbon dioxide is the predominant greenhouse gas. In addition, there is an agreement that the increased concentration of these gases is caused mainly by human activities and natural causes only represent a minor effect. As a result, the combined task of fulfilling the energy demand while battling global warming is one of the biggest challenges that our society has to face.

Despite the efforts dedicated to the reduction of CO_2 emissions and the development of renewable energy sources, the world has only taken the first steps of the transition to a low-carbon energy society. If we intend to reach a sustainable energy scenario we should aim be to replace entirely the fossil fuel energy sources by renewable energies. At best, this transition will take place gradually in the next decades, but CO_2 emissions have to be drastically reduced in the short term in order to reduce the costs and increase the prospects for effective global warming mitigation.

In addition to the increase of the share of renewable energies, CO_2 emissions will have to be reduced by additional means. These include the transition to less polluting fossil fuels (from coal to natural gas or hydrogen), the development of new technologies such as Carbon Capture and Storage (CCS) or the increase of energy efficiency in the industry. In this context, the recovery of waste heat is an effective manner to increase energy efficiency and this work is focused on this subject.

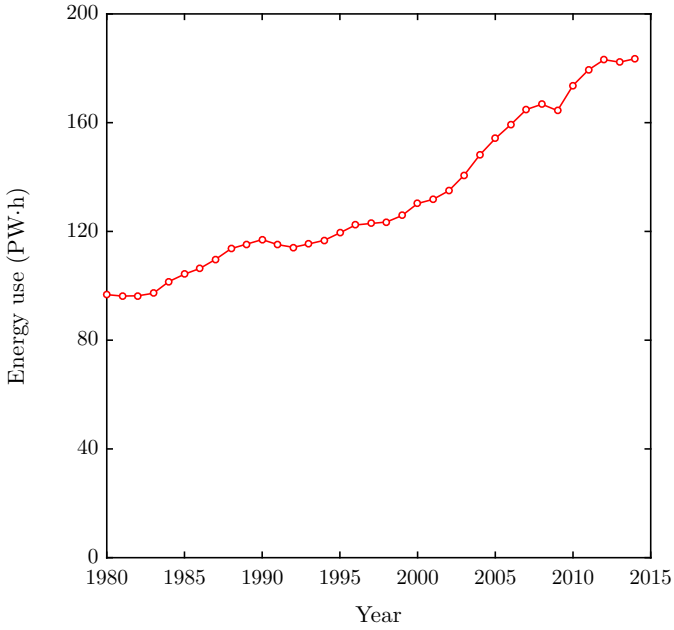

Figure 2.1: Energy use in the world from 1980 to 2014.

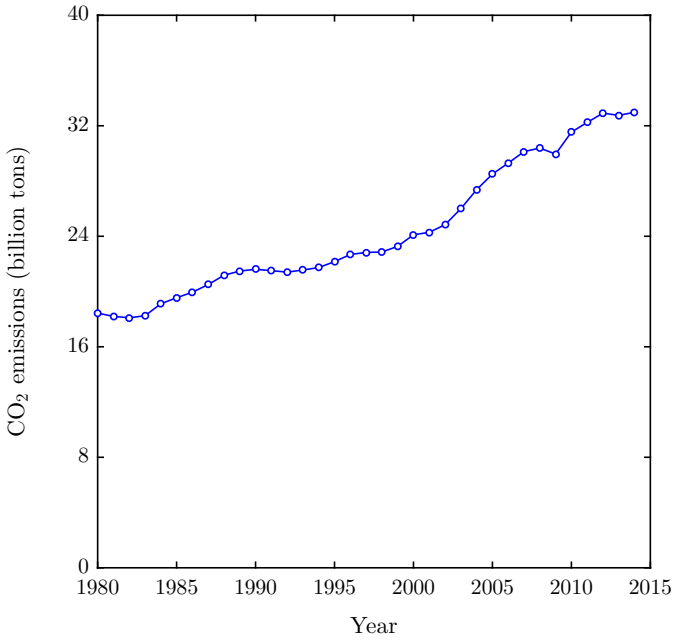

Figure 2.2: CO_2 emissions in the world from 1980 to 2014.

2.2 Waste heat recovery

The recovery of waste heat started to gain a lot interest since the last decades of the twentieth century, see for example Sternlicht (1982) or Larjola (1995). The basic idea is to convert thermal energy into work only if it cannot be used in the process (heat integration) or in other direct applications such as in district heating. In this case, thermal energy can be regarded as waste heat that can be potentially transformed into work.

This unused thermal energy is attractive not only because there are large amounts available in the world, but also because it is accesible at individual locations where it can be converted into work relatively easily. The conversion to work increases the energy efficiency of the industrial process and reduces the specific carbon dioxide emissions. Besides the value of the power generated from the waste heat and the reduction of greenhouse gas emissions, the amount of thermal energy released to the atmosphere and its temperature are reduced, so that possible thermal pollution problems are mitigated as discussed in Quoilin et al. (2013).

There are many applications where waste heat recovery is possible, as reviewed in Quoilin et al. (2013) and more thoroughly in Colonna et al. (2015). These applications include:

- The cement industry, where around 40% of the heat required during the production of cement is in the flue gases at temperatures ranging from 200 °C to 400 °C.
- The iron and steel industries, where the thermal energy of the exhaust gases used to cool the electric arc furnaces and rolling mills can be recovered. This industry requires very diverse processes and the temperature of the waste heat varies greatly.
- The glass industry, where the relatively hot gas (400 °C to 500 °C) leaving the oven that melts the raw material can be used to generate power.
- Besides industrial processes it is also possible to recover waste heat from the exhaust gases of internal combustion engines including diesel engines and gas turbines (400 °C to 900 °C). Examples of engine exhaust heat recovery are found in the offshore oil and gas sector, in pipeline gas recompression stations, or in stationary and marine diesel engines.

Waste heat sources can be classified according to their temperature level as: low temperature ($T < 230$ °C), medium temperature (230 °C $< T <$ 650 °C) and high temperature ($T > 650$ °C). This classification is shared by various authors including Colonna et al. (2015) and Li and Wang (2016).

Converting waste thermal energy into work can be a challenging task depending on the temperature of the heat source. Conventional gas Brayton cycles and steam Rankine cycles are not well suited for low to medium temperature heat sources.

The analysis of real gas Brayton cycles, see Macchi and Astolfi (2016, Chapter 1), reveals that the efficiency is low when the maximum cycle temperature is below 400 °C (if the ambient is used as heat sink). The reason for this is that, as the ratio of the maximum and minimum temperatures of a Brayton cycle becomes small, the impact of turbomachinery

irreversibilities increases, to the point where the back work ratio[1] becomes larger than one, leading to negative thermal efficiencies.

The analysis of real Rankine cycles, see Macchi and Astolfi (2016, Chapter 1), shows that the thermodynamic performance is, to some extent, independent of the working fluid and that water could be as good a fluid candidate as any other substance. However, there are technical limitations associated with steam Rankine cycles at low temperatures. Probably, the main limitation is that, due to the shape of the saturation curve of water in the T–s diagram, it is possible to have a high liquid content at the end of the expansion (*wet expansion*) that would be detrimental for the integrity of turbine blades. If the liquid content at the outlet of the expansion is constrained, a large degree of superheating is required, and this, in turn, would penalize the thermal performance of the cycle. This limitation is illustrated in the T–s diagrams of Fig. 2.3.

Other non-conventional fluids, such as hydrocarbons, fluorinated compounds, or siloxanes can be more favorable than water for the range of temperatures below 400 °C. The selection of working fluid is one of the main challenges for the design of Rankine cycles in waste heat recovery applications and it is discussed in Section. 2.4.

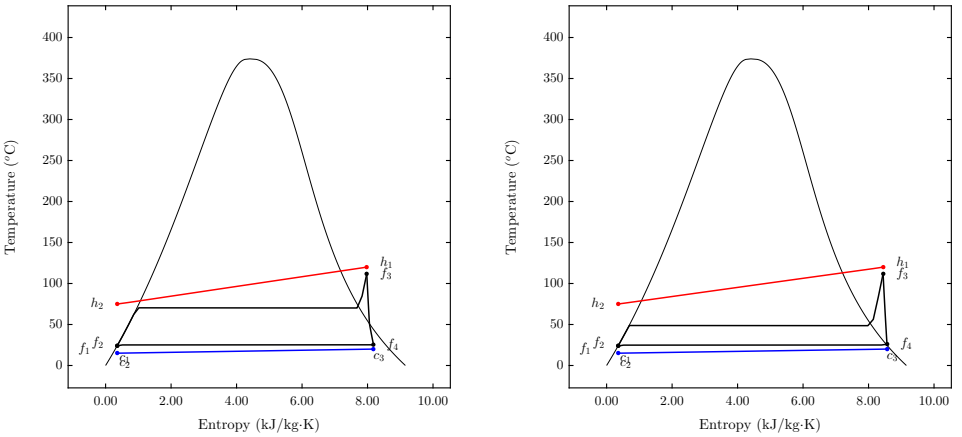

(a) Unconstrained liquid content.

(b) Constrained liquid .

Figure 2.3: T–s diagrams of two low temperature steam Rankine cycles (120 °C hot source inlet temperature). The liquid content at the outlet of the expander is unconstrained for a) and constrained for b). The thermal efficiency of b) is lower than a) because of the high degree of superheating required to avoid liquid at the outlet of the expander. This superheating leads to large temperature differences between the heat source and the working fluid, increasing the exergy destruction in the main heat exchanger.

[1]The back work ratio, BRW, of a Brayton cycle is the ratio of compressor to turbine power. In general, the back work ratio of a power cycle is the ratio of input to output power.

2.3 Rankine cycles

Rankine cycles are closed thermodynamic cycles where the working fluid is continuously vaporized and expanded to convert thermal energy into work. The fundamentals of Rankine cycles can be found in any textbook of classical thermodynamics such as in Moran and Shapiro (2011, Chapter 8) and they are not covered in this work. Instead, the distinctive aspects of Rankine Cycles for waste heat recovery applications are treated here.

2.3.1 Cycle layouts and configurations

The most elementrary Rankine cycle layout is the simple Rankine cycle. This cycle layout is shown in Fig. 2.4 and it consists of four components, pump, primary heat exchanger[2], expander, and condenser. The liquid working fluid is pumped to increase its pressure before it is vaporized and expanded to generate power. The vapor (or possibly a two-phase fluid) at the outlet of the expander is cooled and condensed before it is pumped again, completing the closed loop. As discussed in Moran and Shapiro (2011), it is possible to incorporate several modifications to the simple Rankine cycle layout to increase the thermal efficiency and the specific power, including multiple pressure levels, reheating, regeneration, and recuperation. Rankine cycle architectures common in waste heat recovey applications have been reviewed by Lecompte et al. (2015b).

Multiple pressure level cycles can attain a higher thermodynamic efficiency than their single pressure counterparts because they allow a better temperature match in the primary heat exchanger, leading to smaller exergy losses due to heat transfer. Despite thermal efficiencies can be higher, multiple evaporation pressure cycles are more complex and expensive. For this reason, they are rarely adopted in heat recovery applications and they are not considered in this work.

Reheating is a common practice in conventional steam power plants in order to increase the thermal efficiency and to avoid low-quality steam at the outlet of turbines. However, liquid content at the end of the expansion is not usually a problem for the working fluids commonly used in waste heat recovery applications[3] and reheating is not usually adopted. For this reason, reheating is not considered in this work either.

Regeneration and recuperation are also a common practice in conventional steam power plants and there are many different possible layouts including combinations of open and closed heat exchangers. In waste heat recovery applications, recuperation with a single internal heat exchanger is the only common strategy. The recuperated cycle layout is shown in Fig. 2.5, where the recuperator is used to preheat the fluid entering the evaporator with the fluid leaving the expander.

This work is focused on single-pressure cycles considering both the simple and the recuperated layouts. Reheating and regeneration are not considered. Depending on the pres-

[2]The word evaporator is commonly used for the primary heat exchanger in the field of waste heat recovery. However, in this work, the word evaporator was reserved for the subcritical heat exchanger where the phase transition from liquid to vapor occurs (economizer-evaporator-superheater) in order to avoid confusions.

[3]Fluids used in waste heat recovery applications are usually of the *dry* or *isentropic* type and the end of the expansion falls in the superheated vapor region, see subsection 2.4.1.

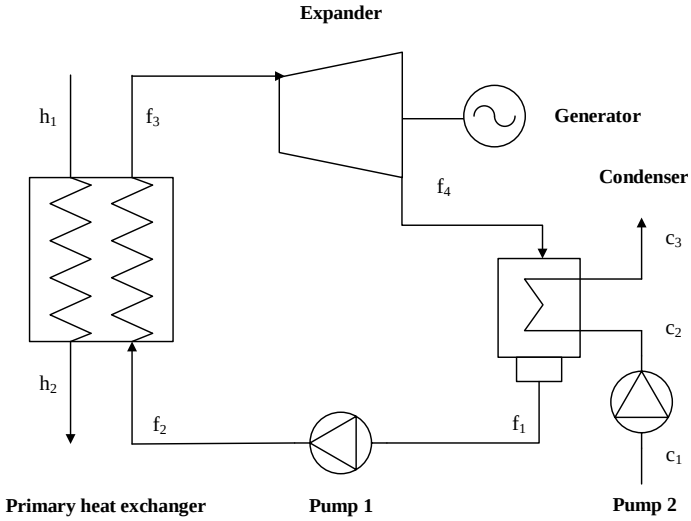

Figure 2.4: Simple cycle layout. The abbreviations h, f, and c are used for hot stream, working fluid, and cool stream, respectively.

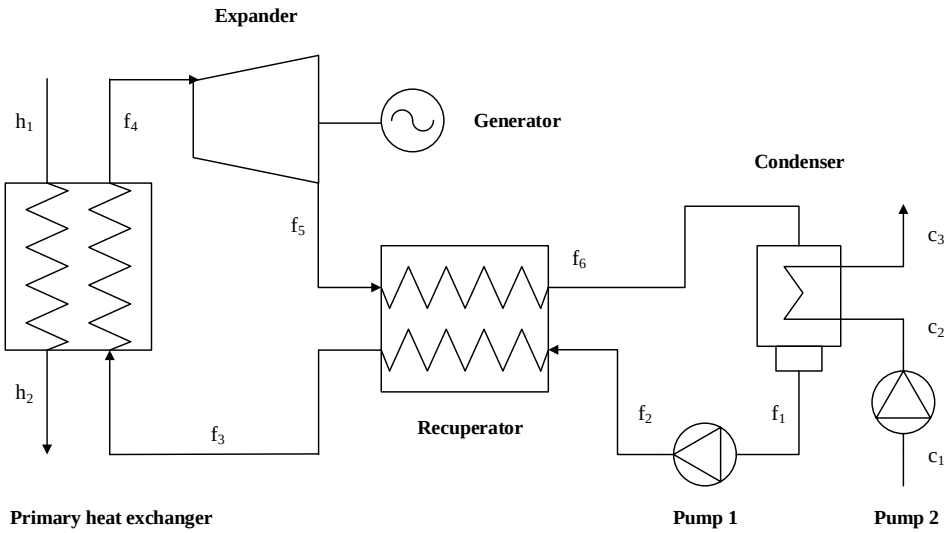

Figure 2.5: Recuperated cycle layout. The abbreviations h, f, and c are used for hot stream, working fluid, and cool stream, respectively.

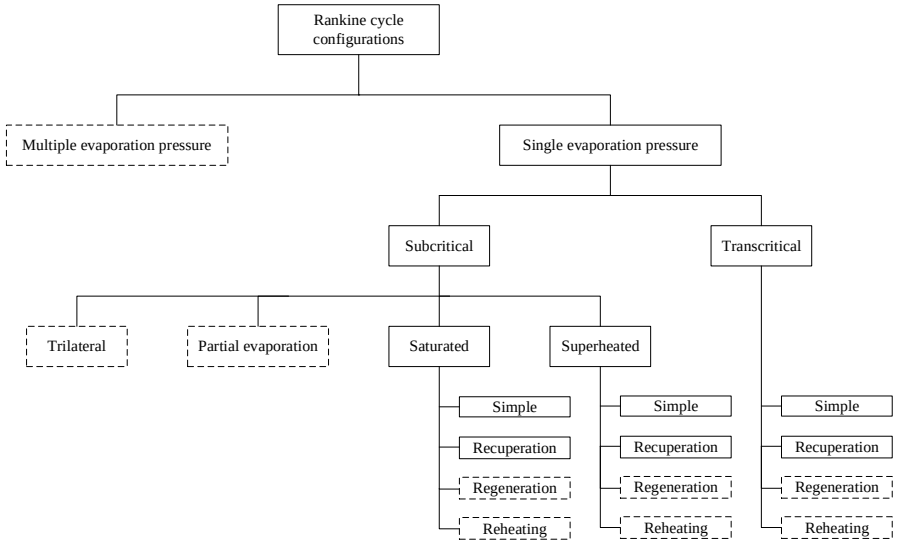

Figure 2.6: Summary of Rankine cycle layouts and configurations. Cycles studied in this work are inside solid boxes while cycles *not* studied in this work are inside dashed boxes.

sure at the inlet of the expander, cycles can be classified into subcritical and transcritical[4]. In addition, there are several types of subcritical cycles depending on the state at the inlet of the expander: trilateral cycles (saturated liquid), partial evaporation cycles (two-phase fluid), saturated cycles (saturated vapor), and superheated cycles (superheated vapor).

The expansion in trilateral and partial evaporation cycles always occurs within the two-phase region preventing the use of turbines to extract the energy from the fluid. For this reason, only saturated, superheated, and transcritical cycles were considered in this work. A summary of the cycle layouts and configurations studied in this work is presented in Fig. 2.6. The characteristics of these cycle configurations are described in more detail in the following subsections.

2.3.2 Saturated, superheated, and transcritical configurations

The saturated and superheated cycle configurations are subcritical cycles characterized by an isothermal phase change from liquid to vapor in the primary heat exchanger. The T–s diagrams of saturated and superheated Rankine cycles are shown in Figs. 2.7a – 2.7b and Figs. 2.7c – 2.7d, respectively. Conversely, in transcritical cycles, the pressure of the working fluid through the primary heat exchanger is supercritical and the fluid is heated at a gliding temperature from subcooled liquid to superheated vapor without a distinct phase change. The T–s diagrams of transcritical Rankine cycles are shown in Figs. 2.7e – 2.7f.

Subcritical cycles are the most common configuration in waste heat recovery applica-

[4]In transcritical cycles the heat addition occurs at supercritical pressures while the heat rejection occurs at subcritical pressures. In supercritical cycles both the heat addition and rejection occurt at supercritical pressures. As a consequence condensation is not possible in supercritical cycles. See Chen (2011).

tions, Macchi and Astolfi (2016, Chapter 3). In saturated cycles, the fluid is heated from subcooled liquid to saturated vapor in the primary heat exchanger and then it is expanded. Whereas, in superheated cycles, the fluid is further heated before the expansion. Saturated cycles are more compact because the primary heat exchanger does not require a superheater unit.

Transcritical cycles can be very advantageous to make use of finite heat capacity sources (gliding temperature). Nearly all heat sources in waste heat recovery applications, such as exhaust gases or cooling liquids, are of this type. Infinite heat capacity sources (constant temperature) are not common in heat recovery applications. See Zhai et al. (2016) for a detailed discussion of the different types of heat sources and their characteristics.

The main advantage of transcritical cycles is that, with a proper selection of the cycle variables, it is possible to match the heating curve of the working fluid with the temperature variation in the main heat exchanger, as shown in Figs. 2.7e to 2.7f. As a result, the heat transfer takes place at a low temperature difference and the irreversibility of the process is small. A discussion of the low irreversibility of heat transfer at gliding temperatures (focusing in fluid mixtures) can be found in Angelino and Colonna (1998). Astolfi et al. (2014) suggested that transcritical cycles are the optimal solution from the thermodynamic point of view when the ratio of the critical temperature of the fluid and the inlet temperature of the heat source lies in the range from 0.88 to 0.92.

$$0.88 \leq T_{crit}/T_{in\,source} \leq 0.92 \tag{2.1}$$

Even if transcritical cycles are very attractive from a thermodynamic point of view, they might not be the optimal solution from a techno-economic perspective. One of the limitations of transcritical cycles is that pump power consumption is large compared to subcritical Rankine cycles[5]. As a consequence, transcritical cycles are more sensible than subcritical cycles to the efficiency of the pump. The cost of multistage pumps with high efficiency is one of the reasons why the transcritical cycles are not commonly adopted, as surveyed in Colonna et al. (2015).

2.3.3 Recuperated cycles

The use of a recuperator in Rankine cycle is beneficial from a *thermodynamic point of view* if two conditions are fulfilled:

1. The fluid at the outlet of the expander is a superheated vapor at a temperature T.
2. There exists a limitation for the lower temperature of the heat source. In particular, the temperature of the heat source can not be reduced below T.

Indeed, if both conditions are fulfilled, the superheated vapor leaving the expander can

[5]The back work ratio of transcritical cycles using low-critical-temperature fluids can be of the order of 30%. This is very high compared with the back work ratio of subcritical cycles using high-critical-temperature fluids, such as conventional steam cycles. The back work ratio of cycles using fluid with high critical temperatues is often lower than 1%.

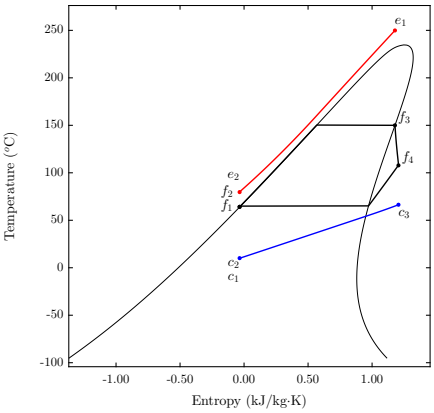

(a) Simple saturated cycle using hexane.

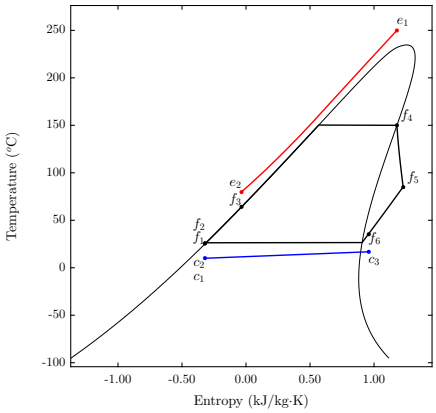

(b) Recuperated saturated cycle using hexane.

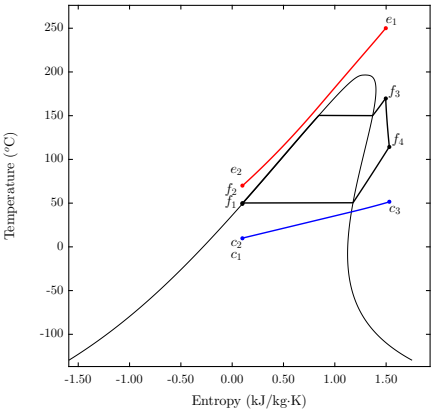

(c) Simple superheated cycle using pentane.

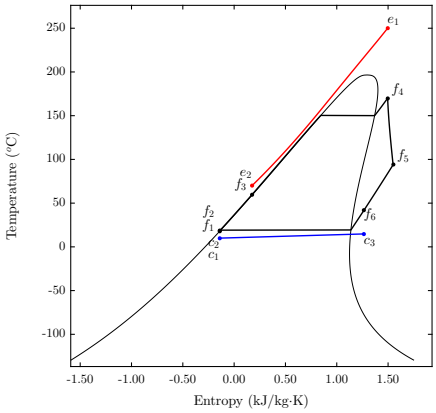

(d) Recuperated superheated cycle using pentane.

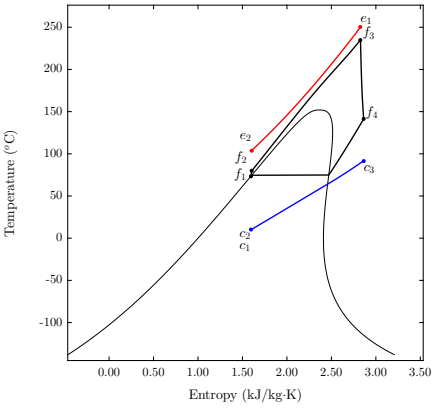

(e) Simple transcritical cycle using butane.

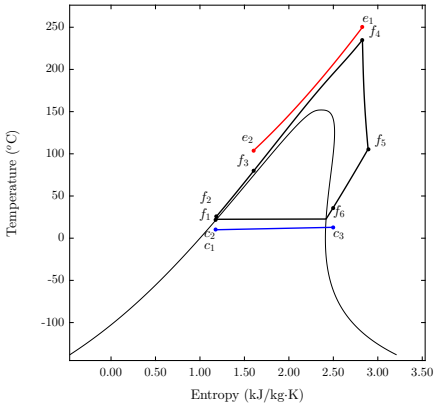

(f) Recuperated transcritical cycle using butane.

Figure 2.7: Examples of the different configurations of Rankine cycles discussed in this section using butane, pentane and hexane as working fluids.

be used to preheat the liquid entering the primary heat exchanger without limiting the exploitation of the heat source.

Many authors propose the use of a recuperator when the fluid leaving the expander is superheated vapor, but neglect the second condition regarding the low temperature limit of the heat source. When the second condition is not fulfilled in applications with gliding temperature heat sources (such as in waste heat recovery or geothermal energy), the use of the recuperator will indeed *increase* the efficiency of the Rankine cycle, but it will also *decrease* utilization of the heat source and the overall thermal efficiency of the plant will not be improved. This was recognized by some authors including Astolfi et al. (2014).

In many cases, there exist a physical limitation for the lowest temperature of the heat source. For instance, in geothermal systems, the outlet temperature of the heat source should be high enough to keep salts in solution. In waste heat recovery applications, the temperature of exhaust gases containing sulfur dioxide should be kept above its dew point to avoid condensation and formation of sulfuric acid, which in turn would lead to corrosion problems. Similarly, when a hot air stream from an industrial process is available for waste heat recovery, its temperature is rarely reduced to ambient temperature, instead, the nominal temperature of the downstream gas cleaning processes imposes a lower temperature limit for the heat recovery.

Even if there is no limitation for the lowest temperature of the heat source, using a recuperator might still be beneficial from a *techno-economic point of view*. This is because the recuperator cools the vapor leaving the turbine, decreasing the load and the size of the condenser. As the condenser is usually a costly component of the system, Colonna et al. (2015), using recuperated cycles should not be excluded a priori even if the second requirement stated in this section is not fulfilled.

2.3.4 Cycle components

The technologies for the main components of Rankine cycles for waste heat recovery applications are described in this section. From a thermodynamic perspective, these components are heat exchangers, expander, and pump. In practice, Rankine cycles require other components for safe and stable operation, but they are not relevant for a steady-state thermodynamic analysis and they are not covered in this work.

This section is based on the reviews from Quoilin et al. (2013) and Colonna et al. (2015), as well as Macchi and Astolfi (2016, Chapter 3).

Primary heat exchanger

The technology used for the primary heat exchanger depends on the cycle configuration. In subcritical cycles, the primary heat exchanger consists of a economizer, an evaporator, and, possibly, a superheater, while, in transcritical cycles or in cycles using mixtures as working fluids, a one-through primary heat exchanger is used.

Thermal energy can be transferred directly from the heat source to the working fluid or indirectly using an intermediate fluid loop. The advantage of direct heating is that it allows to achieve higher maximum fluid temperatures and energy efficiencies. The use of

an intermediate fluid loop is advised in high temperature applications to avoid hot spots during the heat exchange, which could lead to the decomposition of the working fluid. Indirect heating was not considered in this work.

Shell and tubes heat exchangers are the most common architecture for the economizer and superheater. There are two alternatives for the arrangement of the hot and cold fluids:

1. The hot fluid is in the shell side and working fluid flows within the tubes. The advantage of this configuration is that the fluid with higher pressure is in the tubes side and, therefore, the walls of the shell can be slim, decreasing the weight and the cost of the heat exchanger. The drawback of this configuration is that the hot fluid usually has a higher tendency to fouling and the cleaning of the shell side is a complex task that usually involves the use of chemical products.
2. The working fluid is in the shell side and hot fluid flows within the tubes. For this configuration, the tubes usually have a higher tendency to fouling, but this side can be cleaned mechanically in a simpler way. The disadvantage of this option, is that the fluid with higher pressure is on the shell side and the vessel of the heat exchanger has to be thicker to withstand the high pressures.

The evaporator is usually arranged as a kettle reboiler. The hot fluid flows through a two-pass tube arrangement surrounded by a volume of the working liquid in equilibrium with its own vapor. The working fluid leaves the heat exchanger as saturated vapor and a demister section is required to avoid carry-over of liquid droplets, since they could damage the expander in cycles without superheater.

Condenser

Two main technologies are available for the condenser, water cooled condensers and air cooled condensers.

1. Water cooled condensers are preferred when abundant water is available from a river, a lake, or the sea because they allow to achieve lower cycle temperatures and higher efficiencies. This type of condensers usually have a limitation for the maximum temperature increase of the water across the heat exchanger due to environmental reasons related to thermal pollution. Water cooled condensers also use the kettle configuration with the water flowing inside the tubes.
2. Air cooled condensers are used when water is not available or when it is scarce. As the heat transfer coefficients on the air side are low, large surface areas are required for this type of heat exchangers. The large areas on the air side imply large pressure drops, which in turn lead to high power consumption of the fans. These condensers use advanced fin designs on the air side to compensate for the low heat transfer coefficients and achieve large areas per unit of volume.

Recuperator

The recuperator is usually a cross flow heat exchanger with the high pressure liquid inside the tubes and the low pressure vapor outside the tubes. Finned tubes are used to increase

the heat transfer area of the vapor side and compensate for the lower heat transfer coefficients. Recuperators are designed to limit the pressure drop on the vapor side as much as possible, as it affects the expander outlet pressure directly. For this reason, when the expander is a turbine, the recuperator is usually placed right after the diffuser in order to reduce pressure losses between both components.

Expander

An expander is a machine that extracts energy from a fluid flow and converts it into useful work. Expander technologies can be divided into two main categories, turbines and positive displacement machines.

Turbines are formed by a sequence or stator and rotor stages. The fluid is accelerated and expanded in the channels of the stator and then it is deflected, exchanging momentum with the blades of the rotor. As a result of the change of angular momentum of the fluid, a torque is applied to the shaft of the turbine. This torque can drive an electric generator that converts the mechanical energy into electrical power.

Turbines used in waste heat recovery applications can be classified into four categories, according to the relative motion of the fluid with respect to the shaft:

- *Radial inflow*. This kind of machines are very compact and they are meant for power outputs of the order of magnitude from tens to hundreds of kilowatts, but there are also some examples of the order of megawatts. These turbines are characterized by a single centripetal stator and a single centripetal (or mixed-flow) rotor. As the expansion is only divided into two cascades, highly supersonic flows are frequent and strong shocks may occur, specially at off-design conditions.

- *Radial outflow*. The power range of these turbines is wide and covers from tens of kilowatts to megawatts. The advantage of this kind of turbines over radial inflow ones is that they can accommodate several stages of rotor-stator cascades in a relatively compact machine. This allows to avoid highly supersonic flows.

- *Axial*. These turbines are suitable for the power range from hundreds of kilowatts to megawatts. This architecture can accommodate many stages, enabling to reduce the stage loading and to avoid highly supersonic flows. In spite of this, the number of stages is usually kept as low as possible to achieve compact designs.

- *Hybrid*. These turbines integrate a radial inflow stage followed by one or more axial stages. The advantage of this configuration is that it may be more compact that axial turbines and it may help to avoid the highly supersonic flows common in radial inflow turbines. This architecture is not as technologically mature as the other turbine configurations. Hybrid turbines with one of more radial outflow stages followed by axial stages are also possible.

For small power outputs (below 100 kW) the design of efficient turbines is very challenging and positive displacement machines are preferred. In this type of machines, finite volumes of fluid are trapped, expanded, and discharged in a cyclic manner, transforming

the thermal energy of the fluid into mechanical power that can drive an electric generator. There are many different available architectures, but the scroll and the screw expanders are the the most common configurations.

Pump

Variable-speed, multistage, centrifugal pumps are usually adopted in Rankine cycles for waste heat recovery applications. In traditional steam Rankine cycles, the pump consumption is very low compared with the power delivered by the turbine and its efficiency does not play an important role in the net plant efficiency. However, in waste heat recovery applications, specially in transcritical cycles, the pump can account for an important share of the expander power output and the pump efficiency becomes an important parameter of the system.

In order to avoid cavitation, the net positive suction head (NPSH) of the pump should be high enough. Some of the alternatives to avoid cavitation are to locate the pump some distance below the outlet of the condenser (submergence) or to cool the working fluid below the saturated temperature. Nevertheless, the degree of subcooling should be small because it is detrimental for the system from a thermodynamic point of view.

2.4 Working fluids

The choice of working fluid is the most important degree of freedom of a Rankine cycle, Macchi and Astolfi (2016, Chapter 1). There is a large number of possible working fluids, including inorganic substances, hydrocarbons, fluorinated compounds, siloxanes, ethers, or alcohols. Moreover, mixtures of these substances are also possible, but they are not considered in this work.

In this section, a classification of working fluids is presented and the characteristics of the ideal working fluid are described. In addition, a section about thermodynamic properties and equations of state is included.

2.4.1 Classification of working fluids

The two most common criteria to classify working fluids for Rankine cycles are the chemical composition and the slope of the vapor saturation line.

Chemical composition

Working fluids can be classified intofhazrd two main types, inorganic and organic substances. At the same time, organic compounds can be classified into the classes summarized in Table 2.1. A comprehensive list of working fluids for waste heat recovery applications, with their classification and properties, is included in Appendix A.

Table 2.1: Classes of organic working fluids for waste heat recovery applications.

Classes		
Alkanes	Chlorofluorocarbons (CFC)	Linear Siloxanes
Alkenes	Hydrochlorofluorocarbons (HCFC)	Cyclid siloxanes
Alkynes	Hydrofluorocarbons (HFC)	Ketones
Cycloalkanes	Hydrofluoroolefins (HFO)	Alcohols
Aromatics	Perfluorocarons (PFC)	Carbonate esters
	Haloalkanes	Ethers

Slope of the vapor saturation line

Working fluids can also be classified according to the slope of their bubble line in the T–s diagram. Most literature classifies working fluids as *wet*, *dry* or *isentropic* if the slope of the vapor saturation line is negative, positive or, infinite (vertical line), respectively.

The shape of the vapor saturation curve depends on the molecular structure of the working fluid. Simple fluids with few atoms are of the *wet* type while more complex molecules with many atoms are of the *dry* type. Molecules of intermediate complexity are of the *isentropic* type. Figs. 2.8 to 2.11 show the the temperature-entropy diagrams and molecular structures of water, propane, and hexamethyldisiloxane to illustrate this classification.

This working fluid classification gives some information about the possible use of a recuperator. Indeed, if the fluid is of the *dry* type, an isentropic (or nearly isentropic) expansion from the vapor saturation line (such as in a saturated cycle) will end on the superheated vapor region. For this reason, there will always be recuperation potential when using *dry* fluids. Conversely, if the fluid is *isentropic*, or if it is *wet* and the expansion ends in the two phase region, there will not be recuperation potential.

2.4.2 Characteristics of the ideal working fluid

This section describes the characteristics of the ideal working fluid for a Rankine cycle following the criteria given in the reviews Chen et al. (2010) and Quoilin et al. (2013). Other references are particularly stated. No single fluid satisfies all the properties listed in this section and fluid selection is always a compromise between different criteria.

Thermodynamic and physical properties

- The critical temperature of the working fluid should be higher than the ambient temperature to make the condensation process possible.
- The maximum pressure of the cycle should not be excessive to avoid mechanical stress problems and safety concerns.
- The saturation pressure in the condenser should be above atmospheric pressure. Sub-atmospheric condensation pressures may lead to air infiltration problems.
- The melting point of the working fluid should be below the ambient temperature

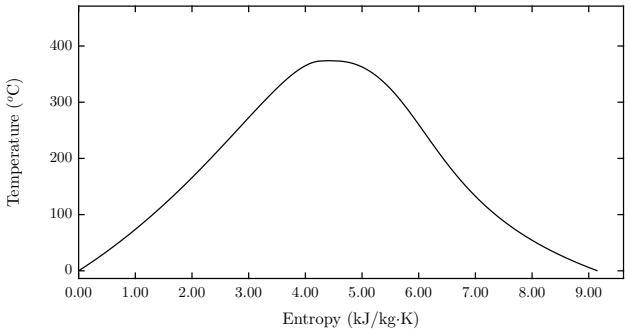

Figure 2.8: Temperature-entropy diagram of water, a simple molecule.

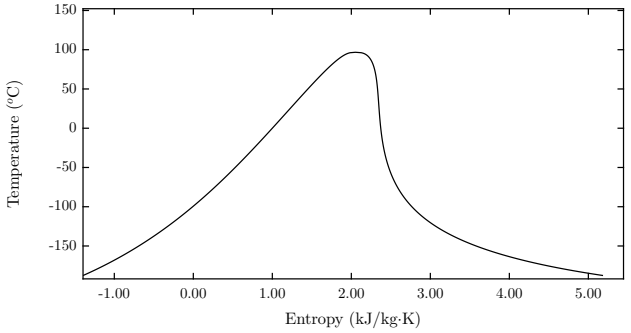

Figure 2.9: Temperature-entropy diagram of propane, an intermediate molecule.

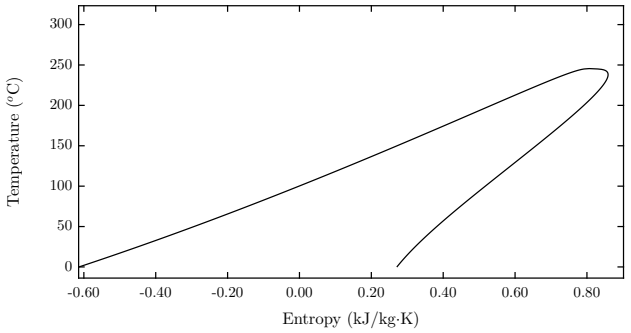

Figure 2.10: Temperature-entropy diagram of hexamethyldisiloxane (MM), a complex molecule.

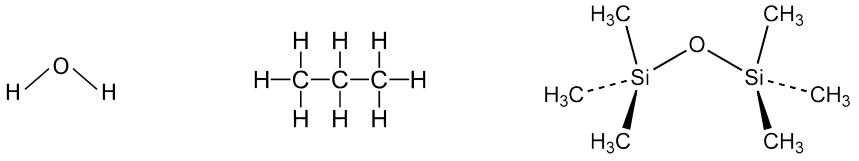

Figure 2.11: Molecular structures of water, propane, and hexamethyldisiloxane.

throughout the year to avoid solidification during shutdown time.

- The fluid should have good thermal properties. The viscosity should be low and the heat conductivity should be high. This leads to high Reynolds and Nusselt numbers, low friction losses, and good heat transfer coefficients.

- The fluid should have high liquid and vapor densities to reduce the size of the heat exchangers.

- The slope of the vapor saturation curve in the temperature entropy diagram should be positive or nearly isentropic. A negative slope of the vapor saturation curve may lead to liquid content in the later stages of the expansion that can be detrimental for the integrity of the expander.

Non-corrosivity

A fluid compatible with he container materials should be used to avoid corrosion problems. The use of deaerators or chemical treatments can be considered to avoid corrosion, but this increases the cost of the system.

Chemical stability

The fluid should be resistant to decomposition over the whole temperature range of the cycle. The fluid should also be chemically stable in the presence of lubricants and the container materials. The chemical stability of the fluid is essential when the whole life of the power cycle is considered. Chemical stability is a complex topic discussed in Macchi and Astolfi (2016, Chapter 5).

Environmental aspects

Two main environmental factors should be considered when selecting an appropriate working fluid:

- Ozone Depletion Potential (ODP) should be null or very close to zero.

- Global Warming Potential (GWP) should be as low as possible.

Information about Ozone Depletion and Global Warming, as well as tabulated values of the ODPs and GWPs of many commom working fluids can be found in Daniel and Velders (2006) and Forster et al. (2007). Tabulated values of ODPs and GWPs for many different substances are summarized in Appendix A.

Safety

Characteristics like non-toxicity, non-flammability and non-explosiveness are desirable for a working fluid, even if they are not always critically necessary. The ASHRAE (2000) refrigerant safety classification is a good indicator of the hazard level of the working fluid.

Availability and cost

The substance should have low cost and be available in large quantities. Inorganic substances like water, carbon dioxide, and ammonia, as well as hydrocarbons meet these requirements while traditional fluorinated refrigerants are more expensive.

2.4.3 Thermophysical properties

The reliability of the simulation and optimization of Rankine cycles and turbomachinery depends a lot on the accuracy of the thermodynamic properties. Thermodynamic properties can be described by Equations of State (EOS) of different complexity and accuracy. An equation of state is a relationship between thermodynamic properties, that is, they allow to compute dependent thermodynamic properties as a function of independent thermodynamic properties. Equations of state can be written using different sets of independent variables and, for pure substances, two independent variables are required to completely determine a thermodynamic state.

There are many different equations of state including the ideal gas law and cubic[6] equations, such as the Peng-Robinson (PR) and Soave-Redlich-Kwong (SKR) equations of state. Despite these simple equations can describe thermodynamic properties accurately in some regions, their accuracy is limited in some cases including computations near the critical point with strong real gas effects.

Because of these weaknesses, more advanced equations of state are required to compute the thermodynamic properties in Rankine cycles. These equations are known as multiparameter equations of state and they are much more accurate and harder to implement than simple cubic equations. There are several families of multiparameter equations of state, but the fundamental Helmholtz-energy-explicit equations of state (HEOS) are now dominating the high-accuracy formulations for the computation of thermodynamic properties, Macchi and Astolfi (2016, Chapter 4). These equations are explicit in the Helmholtz energy function and they are formulated using temperature-density as independent variables. This can be expressed mathematically as $\psi = \psi(T, \rho)$. All other thermodynamic properties, such as pressure or speed of sound, can be computed through derivatives of the Helmholtz energy. Despite these equations are formulated using temperature-density as inputs, other sets of variables more natural in Rankine cycles, such as pressure-enthalpy, and in turbomachinery, such as enthalpy-entropy, can also be used as independent variables. However, the computational routines require interpolations and iterations to handle different sets of variables and the computational time is highly dependent on the inputs.

The quality of an equation of state can be measured according to three characteristics: accuracy, robustness, and speed, see Skaugen et al. (2016). The accuracy indicates how well does the equation of state predict the thermodynamic properties of the substance. Equations of state usually require iterations (such as the solution of a third order polynomial for the case of cubic equations) and the robustness measures the ability of an equation of state to converge for a wide range of input properties. Finally, the speed is related to

[6]The terminology cubic equation of state comes from the fact that these equations involve the solution of a cubic polynomial to find the specific volume as a function of pressure and temperature.

the computational cost of the equation of state. Simple equations, such as the ideal gas law or cubic equations are very fast and robust, but they accuracy is low. Conversely, advanced multiparameter equations of state are very accurate, but they are computationally expensive and they may not converge for all states (specially for complex inputs such as enthalpy-entropy). Accuracy, robustness and speed are often, if not always, incompatible and the most suitable equation of state depends on the interest of the user.

2.4.4 Fluid property libraries

There are many libraries available for the computation of thermodynamic and transport properties including REFPROP, CoolProp, or FluidProp.

REFPROP, Lemmon et al. (2013), was developed by the National Institute of Standards and Technology (NIST) and it is the standard library for the properties of pure fluids and mixtures. This library contains Helmholtz energy equations of state, as well as models for the transport properties, published in the open literature for a large number substances. This library was developed in FORTRAN and there are interfaces available for several programming languages.

In this work, REFPROP, in conjunction with an interface for MATLAB, The MathWorks Inc (2016), was used for the computation of the thermodynamic properties. REFPROP was chosen despite the low speed of Helmholtz energy equations of state because the computational cost of the optimizations carried out in this work, after some code optimization, was small (of the order of minutes).

2.5 Organic Rankine cycles

Besides two notable exceptions, carbon dioxide and ammonia, most of the working fluids proposed for Rankine cycles in waste heat recovery applications are organic fluids. For this reason, these cycles are usually known as Organic Rankine Cycles (ORC)[7]. They have been the focus of many studies in the open literature because they are well suited for renewable energy and waste heat recovery applications.

The purpose of this section is to emphasize the main differences between organic Rankine cycles and conventional steam Rankine cycles. In addition, the main areas of application of organic Rankine cycles are described and a classification for organic Rankine cycle power plants that summarizes most of the content of this chapter (to this point) is included.

2.5.1 Comparison of steam and organic Rankine cycles

Part of the material of this section is not new and was presented previously in this chapter. Despite this, it is included to highlight the differences between organic and steam Rankine cycles. A similar discussion can be found in Quoilin (2011).

[7] The term organic just refers to the nature of the working fluid. There are no conceptual differences between Rankine cycles and organic Rankine cycles.

Slope of the saturation vapor curve

The saturation vapor curve of water has a negative slope (*wet expansion*) while the slope of most oganic substances used in Rankine cycles is negative (*dry expansion*). For this reason, in most organic Rankine cycles, the expansion ends in the superheated vapor region and the problems related with liquid content at the end of the expansion are avoided. Superheating is not necessary (but might the optimal solution) and cycles with reheating are not common.

Maximum temperatures

The maximum temperatures in conventional steam cycles can be higher than 450 °C, while organic Rankine cycles are meant for lower temperatures. For this reason the thermal efficiency of organic Rankine cycles is intrinsically lower. In addition, thermal stresses in the primary heat exchanger are lower and centrifugal stresses in the expander are not so critical in organic Rankine cycles, reducing the cost of these systems.

Back work ratio

In conventional steam power cycles, the pumping power is much lower than the expansion power, as a result, the back work ratio is very low (of the order of 1% or lower). This is a desirable characteristic for a power cycle. In the case of organic Rankine cycles, the back work ratio is highly dependent on the working fluid and cycle configuration. For subcritical cycles using heavy working fluids such as siloxanes the back work ratio can be very low (of the order of 1%), but for transcritical configurations using lighter fluids the back work ratio can be higher than 30 %, see Macchi and Astolfi (2016, Chapter 3).

Condensing pressure

High condensing pressures at ambient temperature are favorable to avoid air infiltration into the cycle. In steam cycles, the saturation pressure is low (1.23 kPa at 10 °C), while for organic Rankine cycles the condensing pressure depends a lot on the choice of working fluid, it ranges from extremely low for heavy fluids such as MD3M, dodecamethylpentasiloxane, (0.0015 kPa at 10 °C) to super-atmospheric for lighter substances like butane (148.45 kPa at 10 °C).

Specific enthalpy difference

The specific enthalpy change in the primary heat exchanger is lower for organic fluids than it is for water. As a result, for a given heat input to the cycle, the required flow rates are higher for organic Rankine cycles. Similarly, the specific enthalpy difference across the expander is also smaller for organic fluids.

Expander design

In steam power cycles, the pressure ratio and enthalpy drop across the expander are high and the mass flow rate is low. This involves the use of complex turbines with several expansion stages. On the other hand, when organic fluids are used, the pressure ratio and specific work are relatively low and the mass flow rate is high. This allows for the design

of simpler and more compact turbines with fewer stages.

However, due to their higher molecular mass, organic fluids have a lower speed of sound than water and supersonic flows are usually encountered in turbomachinery. For this reason, the fluid dynamic optimization of the turbine becomes an crucial step in the design of a successful organic Rankine cycle.

2.5.2 Classification

There are many different criteria to classify organic Rankine cycles, an attempt to give a comprehensive classification is given in Table 2.2. This table follows the classification given in Colonna et al. (2015) with some minor changes and summarizes most of the content of this chapter to this point.

Table 2.2: Classification of organic Rankine cycles.

Maximum cycle temperature [a]		**Power capacity**	
Low temperature	$<$150 ^{o}C	Micro	$<$3 kW
Medium temperature	150-250 ^{o}C	Mini	3-50 kW
High temperature	$>$250 ^{o}C	Small	50-500 kW
		Medium	0.5-5 MW
		Large	$>$5 MW
Working fluid class		**Thermal energy source**	
Hydrocarbons	Alkanes, alkenes, cycloalkanes, aromatics	Solar	
Fluorocarbons [b]	CFC, HCFC, HFC, HFO, PFC	Geothermal	
Siloxanes	Cyclic, linear	Biomass	
Other organic substance	Alcohols, ketones, ethers, esters	Industrial waste heat	
Mixtures		Engine waste heat	
Cycle configuration		**Cooling medium**	
Saturated	Simple-recuperated, single-multi pressure	Air	
Superheated	Simple-recuperated, single-multi pressure	Water	
Transcritical	Simple-recuperated, single pressure	CHP fluid	
Expander type		**Heating medium**	
Turbine	Radial inflow, radial outflow, axial	Direct	liquid, gas
Volumetric expander	Scroll, screw, piston, vane	Indirect	thermal oil loop, water loop

[a] The classification of low-medium-high temperature for ORC applications does not coincide with the classification of low-medium-high temperature heat sources given in section 2.2.
[b] Chlorofluorocarbon (CFC), hydrochlorofluorocarbon (HCFC), hydrofluorocarbon (HFC), hydrofluoroolefin(HFO), perfluorocarbon (PFC).

2.6 Thermodynamics of expansion for Rankine cycles

In the context of Rankine cycles, an expansion is a process where the pressure and the enthalpy of the working fluid are reduced to extract energy from it. In Rankine cycles for waste heat recovery applications, the the properties of the working fluid during the expansion often deviate largely from the ideal gas behavior and the speed of sound is lower than in conventional gas and steam turbines. This section aims to answer three questions regarding the thermodynamics of expansion processes:

1. What is the ideal expansion process?
2. How to measure the efficiency of a real expansion process?
3. How strong can the real gas effects be along the expansion?

2.6.1 Ideal expansion process

When the state at the inlet and the pressure at the outlet of an adiabatic turbine are fixed, the ideal process that gives the maximum work is an isentropic expansion. In real turbines, the entropy is increased due to irreversibilities such as friction or shock waves, see Section 2.9.

The reason why the maximum work is obtained for an isentropic expansion is a consequence of the first and second laws of thermodynamics and the fact that the lines of constant pressure in the h–s diagram have positive slopes. For the case of an adiabatic expansion, if the kinetic energy is neglected, the first law of thermodynamics indicates that the specific work is given by the enthalpy difference between inlet and outlet:

$$w = h_1 - h_2 \tag{2.2}$$

In addition, the second law of thermodynamics imposes that the entropy of the flow must increase or remain constant for the limiting case of a reversible process:

$$s_2 \geq s_1 \tag{2.3}$$

As the lines of constant pressure in the h–s diagram always have positive slopes the maximum work output is obtained by an isentropic process:

$$w_{max} = h_1 - h_{2s} \tag{2.4}$$

Any entropy increase will lead to a lower power output. This is illustrated in Fig. 2.12. The fact that the lines of constant pressure always have positive slope can be proved from thermodynamic relations. Consider the second Gibbs relation:

$$\mathrm{d}h = T\,\mathrm{d}s + \mathrm{d}p/\rho \tag{2.5}$$

Eq. 2.5 suggests that the canonical variables for enthalpy are entropy and pressure, that

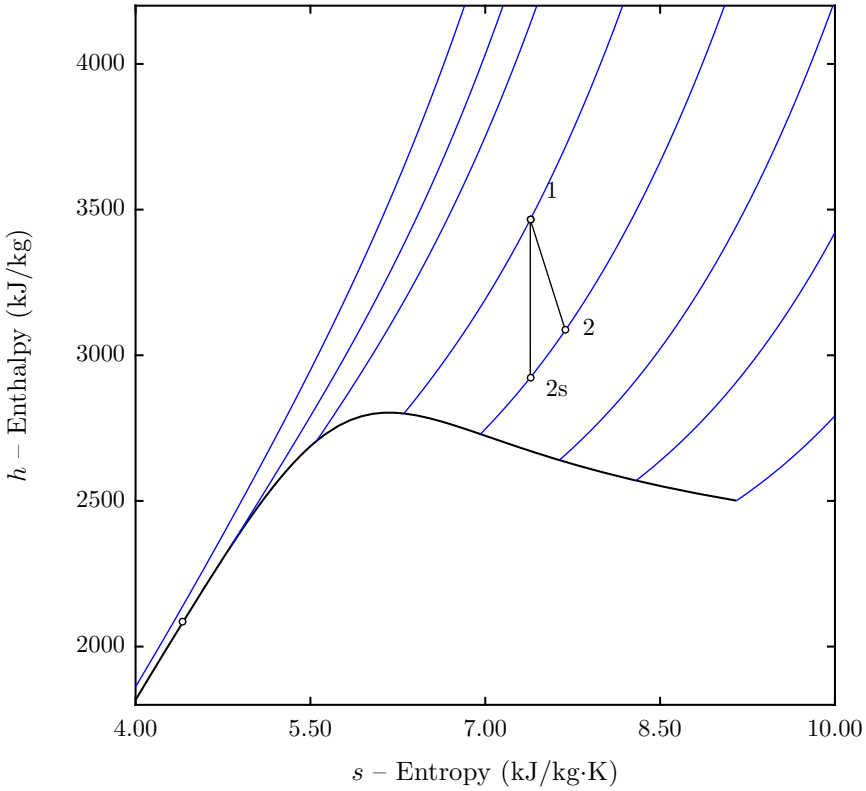

Figure 2.12: Comparison of an isentropic and a real expansion in a steam turbine.

is, $h = h(s, p)$. The exact differential of enthalpy is then given by:

$$\mathrm{d}h = \left(\frac{\partial h}{\partial s}\right)_p \mathrm{d}s + \left(\frac{\partial h}{\partial p}\right)_s \mathrm{d}p \tag{2.6}$$

The slope of the constant pressure lines in the h–s diagram is found by comparison:

$$\left(\frac{\partial h}{\partial s}\right)_p = T \tag{2.7}$$

As the absolute temperature is always positive, the slope of the constant pressure lines is always positive, as we wanted to prove.

2.6.2 Definition of efficiency

The efficiency of the expansion can be defined as the ratio of the actual work to the ideal (maximum) work that can be extracted from the fluid. The actual work is unambiguous, but the ideal work depends on how the ideal process is defined.

Isentropic efficiency

As proven in Section 2.6.1, the maximum work is obtained for an isentropic expansion. When the kinetic energy is neglected the actual work is given by Eq. 2.2 and the ideal work is given by Eq. 2.4. The efficiency is defined as:

$$\eta_s = \frac{w}{w_s} = \frac{h_1 - h_2}{h_1 - h_{2s}} \tag{2.8}$$

This efficiency is known as isentropic efficiency. The limitation of this definition is that it does not account for the kinetic energy of the flow. Since the velocity at the inlet and outlet of turbomachinery can be high, it is necessary to use other efficiency definitions that account for kinetic energy.

Effects of kinetic energy

If kinetic energy is taken into account, the first law of thermodynamics indicates that the specific work is given by the differences of stagnation enthalpy between inlet and outlet:

$$w = h_{01} - h_{02} = (h_1 - h_2) + \frac{1}{2}(v_1^2 - v_2^2) \tag{2.9}$$

The definition of the *ideal specific work* depends upon whether the exit kinetic energy is useful (total-to-total efficiency) or it is wasted (total-to static-efficiency).

Total-to-total isentropic efficiency

If the outlet kinetic energy is useful, the ideal expansion is to the same stagnation pressure as the actual process. The ideal work output is given by:

$$w_s = h_{01} - h_{02s} = (h_1 - h_{2s}) + \frac{1}{2}(v_1^2 - v_2^2) \tag{2.10}$$

This efficiency is known as the *total-to-total efficiency*:

$$\eta_{tt} = \frac{w}{w_s} = \frac{h_{01} - h_{02}}{h_{01} - h_{02s}} \tag{2.11}$$

The total-to-total efficiency is relevant when the outlet kinetic energy is not wasted, for example, at the outlet of an aircraft gas turbine.

Total-to-static isentropic efficiency

If the kinetic energy is not useful, the ideal expansion is to the same static pressure as the actual process with zero kinetic energy at the outlet. The ideal work output is given by:

$$w_s = h_{01} - h_{2s} = h_{01} - h_{02s} + \frac{1}{2}v_2^2 \tag{2.12}$$

This efficiency is known as the *total-to-static efficiency*:

$$\eta_{ts} = \frac{w}{w_s} = \frac{h_{01} - h_{02}}{h_{01} - h_{2s}} = \frac{h_{01} - h_{02}}{h_{01} - h_{02s} + v_2^2/2} \tag{2.13}$$

Comparing Eq. 2.11 and Eq. 2.13 reveals that the total-to-total efficiency is always greater to the total-to-static efficiency. The total-to-total efficiency accounts for the internal losses within the turbine, while the total-to-static efficiency accounts for the internal losses and the kinetic energy wasted at the outlet. For this reason, the total-to-static efficiency is relevant when the outlet kinetic energy is not used, such as in turbine without diffuser.

The design and optimization of a diffuser was out of the scope of this work and, as a consequence, the total-to-static efficiency was used as objective function for the turbomachinery optimization, see Section. 3.4.1.

Polytropic efficiency

The isentropic efficiencies defined in the previous sections are suitable to analyze the performance of a particular turbine design. However, the polytropic efficiency is more suited for the thermodynamic optimization of the whole cycle because it can be regarded as independent of the pressure ratio, see Dixon and Hall (2013).

An expansion can be divided into one or several stages. If a turbine has more than one stage, and all the stages have the same isentropic efficiency, the overall turbine efficiency will be different than the stage efficiency. As the number of stages increases, the stage efficiency and the overall efficiency drift further apart. In the limit, when there is an infinite number of stages, the stage efficiency is known as the polytropic efficiency. The polytropic efficiency for an expansion is defined as:

$$\eta_{polytropic} = \frac{\delta w}{\delta w_s} = \frac{\mathrm{d}h}{\mathrm{d}h_s} = \frac{\mathrm{d}h}{\mathrm{d}p/\rho} \tag{2.14}$$

Where Eq. 2.5 was used to relate the isentropic enthalpy change with the pressure change. Knowing the polytropic efficiency, ,the inlet state, and the pressure at the end of the expansion, the state at the outlet can be determined solving the ordinary differential equation defined by Eq. 2.15 from p_1 to p_2.

$$\frac{\mathrm{d}h}{\mathrm{d}p} = \rho \cdot \eta_{polytropic} \tag{2.15}$$

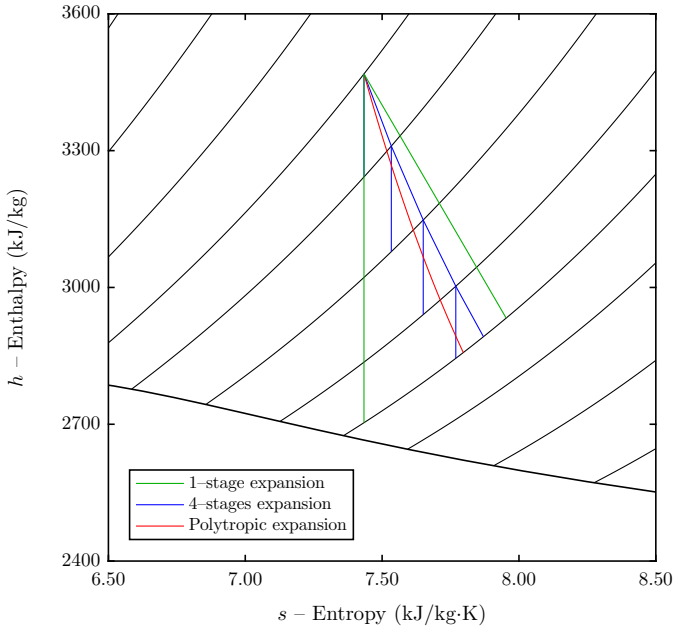

Figure 2.13: Comparison of a single-stage, four-stage, and polytropic expansions of steam in the h–s diagram (the black line at the the bottom is the vapor saturation curve). The same numerical value of efficiency was used for the three expansions.

To illustrate the concepts of this section, Fig. 2.13 shows the h–s diagram for expansion of steam for one stage, a finite number of stages, and an infinite number of stages. The same value of stage efficiency and polytropic efficiency were used for the three cases. It can be observed that the state at the outlet of the turbine depends on the number of stages of the expansion. In this work, the polytropic efficiency was used to model the turbine (and the pump) during the cycle optimization, see Section 3.3.5.

2.6.3 Compressibility factor

The compressibility factor, Z, is a thermodynamic property used to describe the deviance of the thermodynamic properties of a real gas (or in general any substance) from those expected for an ideal gas. The compressibility factor is defined as:

$$Z = \frac{p}{\rho R T} \tag{2.16}$$

Where $R = \bar{R}/M$, $\bar{R} = 8.3144598$ J/mol·K is the universal gas constant, and M is the molar mass[8] of the substance. The compressibility factor can be interpreted as the ratio of

[8] Often called molecular weight, although technically incorrect.

the ideal gas density to the actual density of the gas at the same temperature and pressure:

$$Z = \frac{\rho_{ideal}(T,p)}{\rho_{real}(T,p)} \tag{2.17}$$

If $Z > 1$ the actual density of the gas is lower than that of an ideal gas and if $Z < 1$ the actual density of the gas is higher than that of the ideal gas.

Real gas effects often arise at the first stages of the expansion in Rankine cycles and Z is an useful parameter to asses the deviation from the ideal gas behavior. As an illustrative example, Fig. 2.14 shows the compressibility factor of carbon dioxide as function of the reduced temperature and pressure. The variation of Z for the range of pressures typical in Rankine cycles is highlighted in Fig. 2.15. Although these graphs are only quantitatively accurate for carbon dioxide, they are qualitatively true any substance.

In the limit when the pressure approaches zero (low density limit) the compressibility factor of all substances approaches unity and the equation of state reduces to the ideal gas law. It can be observed that, the compressibility factor for the range of pressures and temperatures typical for the expansion in Rankine cycles is always less than unity, Fig. 2.15. For a given pressure, the compressibility factor of a gas is reduced as the temperature approaches the saturation vapor line. In addition, the largest deviations from the ideal gas behavior occur close to the critical point[9].

Although it is not usual, the thermodynamic trajectory of the expansion in the compressibility factor chart for several illustrative examples (saturated, superheated, and transcritical Rankine cycles) will be considered in Section 2.6.5.

2.6.4 Speed of sound

The speed of sound, a, is a thermodynamic property defined as the distance traveled per unit time by a sound wave, that is, an infinitely small pressure disturbance that propagates through a solid or fluid. The speed of sound is an important parameter for the study of compressible flow because the flow regime depends on the ratio of the fluid velocity to the speed of sound. This ratio is known as Mach number:

$$\mathrm{Ma} = \frac{v}{a} \tag{2.18}$$

When the Mach number of the flow is low[10], there are not large compressibility effects due to velocity changes and the flow can be regarded as incompressible. However, as the Mach number approaches and exceeds one, small changes in velocity lead to large changes in thermodynamic properties. The analysis of subsonic flows is simpler than that of supersonic flow. In addition, supersonic flows lead to higher losses in turbomachinery and the velocity of the fluid is often limited to subsonic flows or not too supersonic flows.

[9] $Z \approx 0.2$ at the critical point, this means that the density of a gas at the critical state is approximately 5 times larger than the ideal gas density at the corresponding pressure and temperature.

[10] Compressibility effects can be neglected when $\mathrm{Ma} < 0.3$, see Fox et al. (2011) or Dixon and Hall (2013)

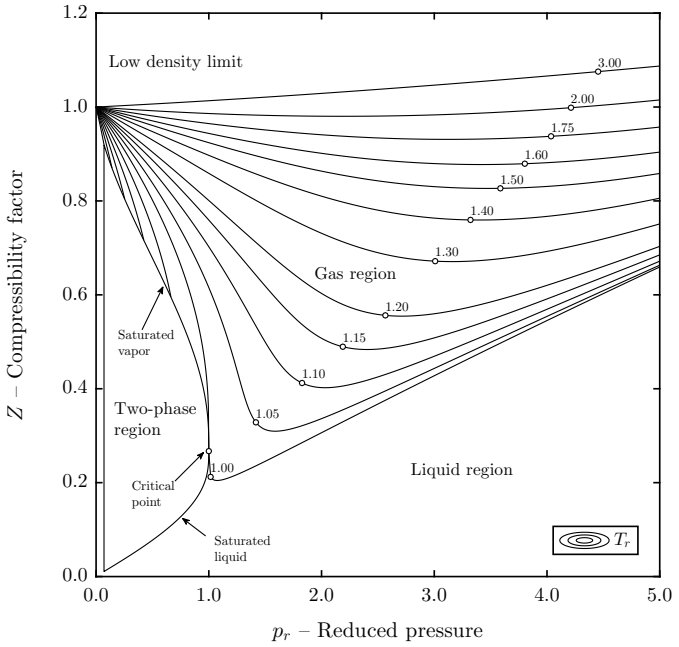

Figure 2.14: Compressibility factor of CO_2 as a function of reduced temperature and pressure. A wide thermodynamic region is covered in the figure.

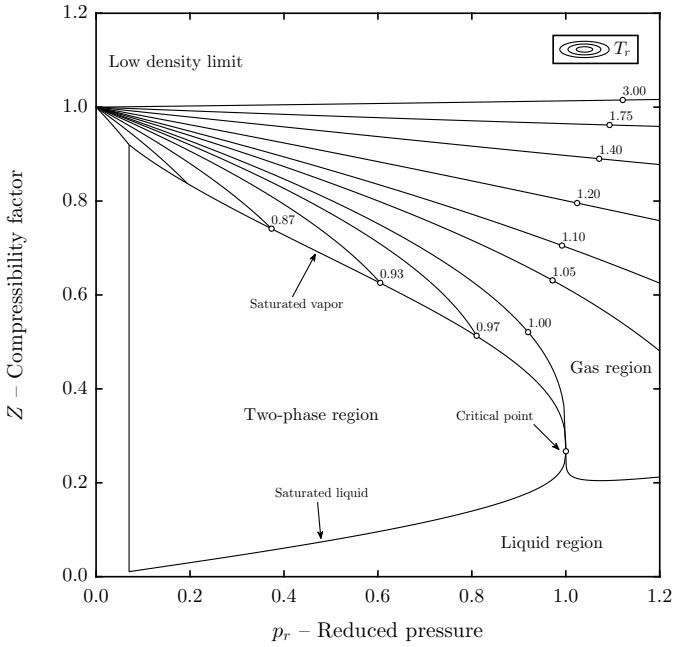

Figure 2.15: Compressibility factor of CO_2 as a function of reduced temperature and pressure. The thermodynamic region relevant for expansions in Rankine cycles is covered in the figure.

The speed of sound of an ideal gas is just a function of the temperature of the gas and it is given by the known relation:

$$a = \sqrt{\gamma R T} \tag{2.19}$$

Where $\gamma = c_p/c_v$ is the heat capacity ratio and $R = \bar{R}/M$, depends on the molar mass of the working fluid.

The speed of sound is high for light simple molecules (low molecular mass and high heat capacity ratio) and low for heavy complex molecules (high molecular mass and low heat capacity ratio). This is illustrated in Fig. 2.16 and Fig. 2.17, where the ideal gas speed of sound and the ideal gas heat capacity ratio are plotted for several substances common in Rankine cycles. It can be observed that the heat capacity ratio decreases with the temperature and it is higher for simple diatomic molecules, as nitrogen, than for complex organic substances, such as hexamethyldisiloxane (MM).

Despite γ decreases with the temperature, Fig. 2.17, the ideal gas speed of sound, Fig. 2.16, always increases as the temperature increases. This is not always the case for a real gas. When the working fluid does not behave as an ideal gas, the speed of sound is a function of two independent thermodynamic properties, such as temperature and pressure. As an illustrative example, Fig. 2.18 shows the speed of sound of nitrogen as function of the reduced temperature and pressure. The variation of a for the range of pressures typical in Rankine cycles is highlighted in Fig. 2.19. Although these graphs are only quantitatively accurate for nitrogen, they are qualitatively true any substance.

The dependence of the speed of sound upon pressure is not often discussed in thermodynamics and fluid mechanics textbooks because most analyses in compressible flow deal with ideal gases. Fig. 2.19 shows that there can be large differences between the ideal gas speed of sound ($p_r = 0.00$ isoline) and the actual speed of sound. It can be observed that the saturated vapor speed of sound is always lower than the ideal gas speed of sound and that the speed of sound reaches a minimum at the critical point[11]

Although it is not usual, the thermodynamic trajectory of the expansion in the speed of sound chart for several illustrative examples (saturated, superheated, and transcritical Rankine cycles) will be considered in Section 2.6.5.

[11] The speed of sound of nitrogen at the critical point is $a \approx 100$ m/s while the corresponding ideal gas speed of sound $a \approx 250$ m/s. Using the ideal gas speed of sound will probably lead to miss-predictions of the flow regime (subsonic or supersonic) in these cases.

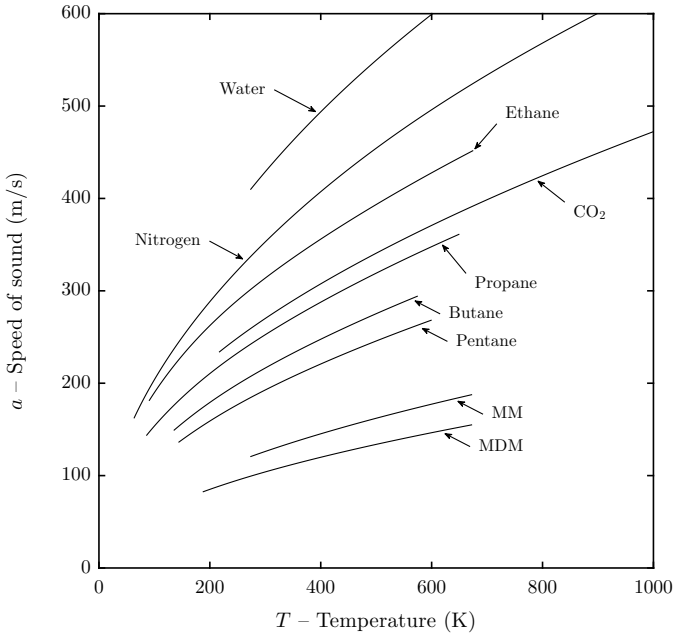

Figure 2.16: Ideal gas speed of sound of several substances as a function of temperature.

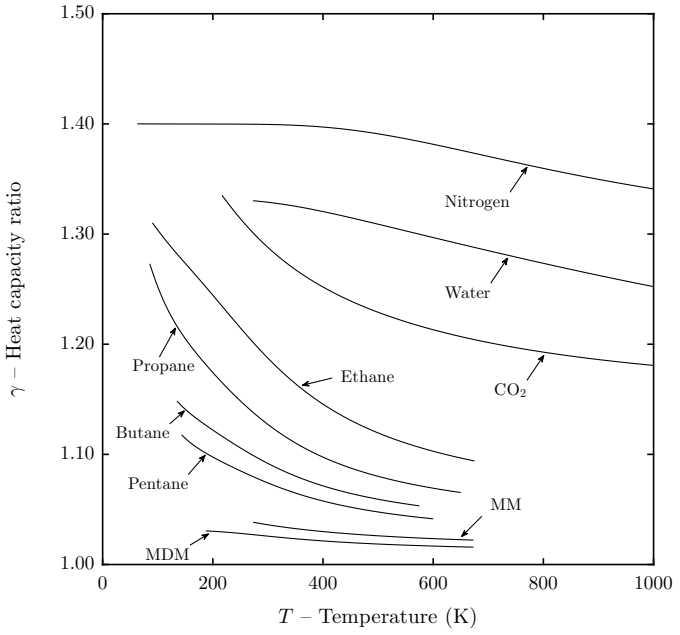

Figure 2.17: Ideal gas heat capacity ratio of several substances as a function of temperature.

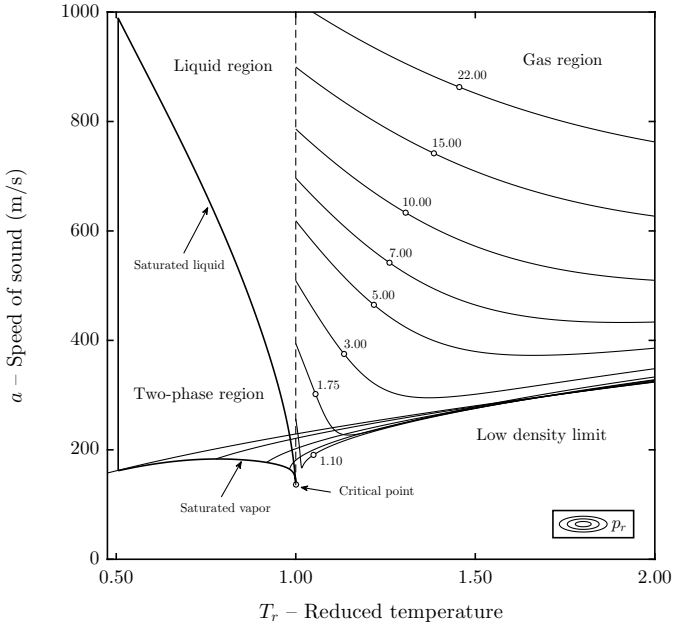

Figure 2.18: Speed of sound of nitrogen as a function of reduced temperature and pressure. A wide thermodynamic region is covered in the figure.

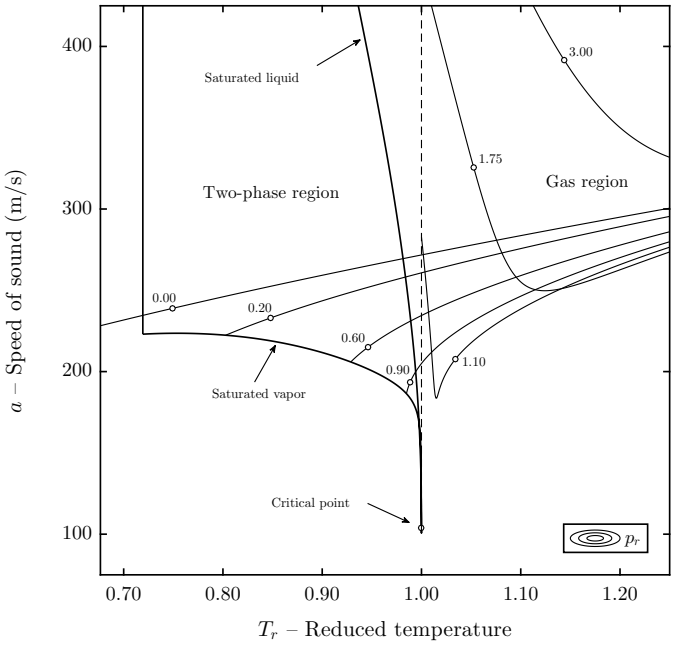

Figure 2.19: Speed of sound of nitrogen as a function of reduced temperature and pressure. The thermodynamic region relevant for expansions in Rankine cycles if covered in the figure.

2.6.5 Saturated, superheated, and transcritical expansions

The compressibility factor is an useful variable to asses the real gas effect along the expansion in Rankine cycles. In addition, the speed of sound can also be studied to gain insight into the Mach number limitations within the turbine.

For the sake of illustration, three examples where considered: expansion of MM from saturated vapor, expansion of toluene from superheated vapor, and expansion of pentane from transcritical conditions. The expansion was assumed to be isentropic and the compressibility factor and speed of sound were plotted along the expansion in Fig. 2.20. The ideal gas speed of sound (corresponding to the $p_r = 0.00$ isoline) was highlighted in red.

It can be observed that the compressibility factor is always lower than one (the gas density is higher than the ideal gas density). In addition, the strongest real gas effects are present in the transcritical expansion of pentane, followed by the saturated expansion of MM. The compressibility factor is close to one for the case of superheated expansion of toluene, due to the low reduced pressure. One important feature is that the compressibility factor approaches one at end of the expansion for all cases. This means that the strongest real gas effects occur at the inlet of the turbine and the working fluid approaches the ideal gas behavior as the pressure is reduced.

Regarding the speed of sound, it can be observed that the real gas speed of sound is always lower than the ideal gas speed of sound. In addition, the speed of sound can increase or decrease along the expansion depending on the real gas effects. A particularly strange effect occurs for the expansion of pentane from transcritical conditions: the speed of sound first decreases as it approaches the critical temperature (strong real gas effects), then increases as the pressure is reduced (the real gas effects become weaker), and finally decreases again at the end of the expansion as temperature decreases and the compressibility factor approaches one (ideal gas) , see Eq. 2.19.

The purpose of this analysis was to illustrate that real gas effects ($Z < 1$ and $a < \sqrt{\gamma RT}$) can be very significant in Rankine cycles and that accurate equations of state are necessary to obtain reliable results from the cycle and turbomachinery optimization.

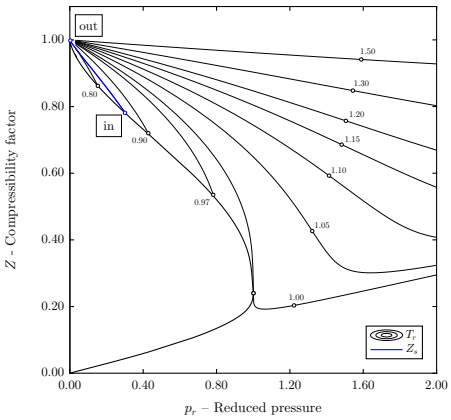

(a) Compressibility factor of MM.

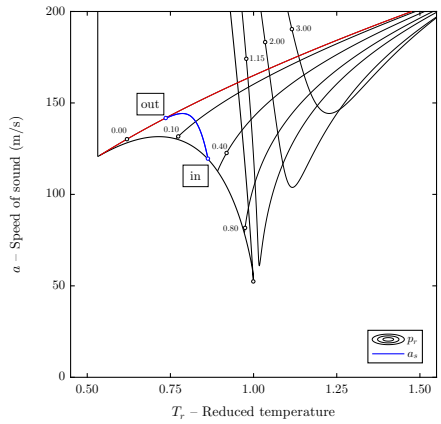

(b) Speed of sound of MM.

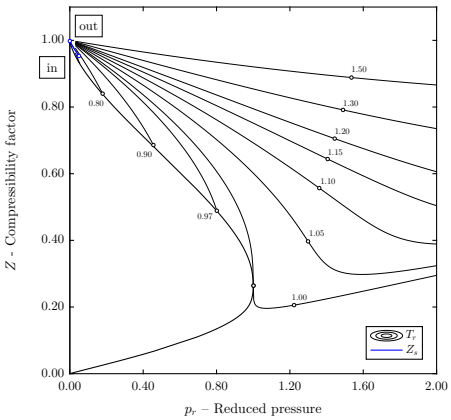

(c) Compressibility factor of toluene.

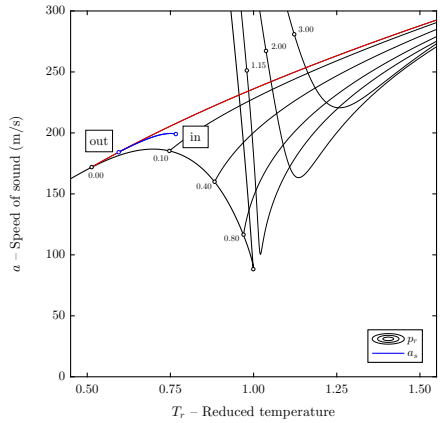

(d) Speed of sound of toluene.

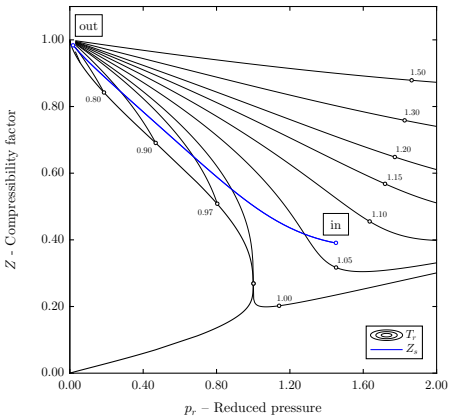

(e) Compressibility factor of pentane.

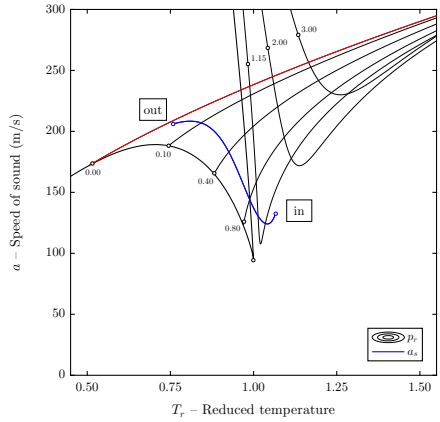

(f) Speed of sound of pentane.

Figure 2.20: Examples of the compressibilily factor and speed of sound for the expansion of saturated (a and b), superheated (c and d), and transcritical (e and f) Rankine cycles.

2.7 Selection of turbine technology

The aim of this short section is to justify the selection of the expander technology.

The power output for the waste heat recovery case study considered in this work is expected to be larger than 100 kW, see Sec. 3.1. For this reason positive displacement machines were discarded, see Sec. 2.3.4. In addition, radial outflow turbines were discarded because they are relatively unconventional and the open literature describing this technology is scarce, see Aungier (2006, Chapter 1), even if new research was carried on in the field of organic Rankine cycles, Macchi and Astolfi (2016, Chapter 11).

Both radial inflow and axial turbines are mature and openly-documented technologies, suitable for the power range of waste heat recovery applications (from hundreds of kilowatts to megawatts). As the scope of this work was wide, it was not possible analyze both technologies within the time frame of the Master Thesis. Axial turbines were chosen because other researchers of the COPRO project are currently doing similar efforts on radial inflow turbines and it seemed unwise to overlap efforts. Naturally, hybrid turbines were discarded because they require knowledge of both radial inflow and axial turbines.

2.8 Fundamentals of axial turbines

The purpose of this catch-all section is to introduce, as softly as possible, the fundamental physical concepts of axial turbines, the nomenclature and conventions used in this work, and some of the main equations that were used to optimize axial turbines. The contents covered in this section can be summarized as:

1. Working principle of axial turbines.
2. Nomenclature and angle conventions for the velocity triangles and description of the geometry of blades, stages, and the axial turbine as a whole.
3. Euler's equation of turbomachinery and rothalpy.
4. Stage design parameters for axial turbines.
5. Equations for repeating-stage turbines.
6. Number of stages.
7. Specific speed and specific diameter.

The different types of losses in axial turbines and the correlations to estimate them are covered in Section 2.9 and Section 2.10, respectively.

2.8.1 Working principle

A turbine is a machine that extracts energy from a fluid flow and converts it into useful work. An axial turbine is a turbine in which the flow of the working fluid is parallel to the shaft. Axial turbines consist of one of more stages and each stage consists of a cascade of stationary blades, known as stator or nozzle section, and a cascade of rotating blades, known as rotor section.

The purpose of a blade cascade is to deflect the flow: stator blades deflect the flow to accelerate it and rotor blades deflect the flow to extract work from it. The fluid is accelerated and expanded in the converging[12] channels of the stator and then it is deflected exchanging momentum with the blades of the rotor. As a result of the change of angular momentum of the fluid, a torque is applied to the shaft of the turbine.

2.8.2 Nomenclature and conventions

An important difficulty one finds when first reading turbine literature is that the nomenclature, notation, and angle conventions are not uniform among different authors, countries (American and English traditions), and industries (steam turbine and gas turbine traditions). For this reason, the writer made an effort to state clearly the terminology and conventions used in this work.

In this section, the angle convention and notation used for the velocity triangles are presented and discussed. In addition, the geometry of blades, stages, and the axial turbine as a whole is described as a pretext to introduce the nomenclature used in this work. Besides the explanations contained in this section, a complete list of symbols was included to condense the notation used in this work and an extensive glossary was prepared for the convenience of the reader.

The glossary was prepared using several turbomachinery textbooks as references: Aungier (2006), Saravanamuttoo et al. (2009), Boyce (2011), Schobeiri (2012), and Dixon and Hall (2013). Due to the extension of this work, and to avoid repeating symbols for different physical quantities as much as possible, the notation used in this work could not match exactly that of any of these textbooks.

Velocity triangle description

As turbines are axi-symmetric it is natural to use cylindrical coordinates to describe the velocity field. In this coordinate system the absolute velocity, v, has three components:

- Axial component – v_x
- Radial component – v_r
- Tangential[13] component – v_θ

The absolute velocity and its components are related according to Eq. 2.20.

$$v^2 = v_x^2 + v_r^2 + v_\theta^2 \tag{2.20}$$

The velocity along the axi-symmetric stream surface is known as the meridional component of velocity and it is defined by Eq. 2.21.

$$v_m^2 = v_x^2 + v_r^2 \tag{2.21}$$

[12] The channels are converging in subsonic machines and converging–diverging in supersonic machines

[13] The tangential velocity component is also known as circunferental velocity or swirl velocity.

For the case of purely axial turbines the radial velocity is zero, $v_r = 0$, and the meridional velocity is equal to the axial velocity, $v_m = v_x$. The absolute swirl angle or tangential angle is the angle between the absolute and meridional velocities and it is given by Eq. 2.22.

$$\tan(\alpha) = \frac{v_\theta}{v_m} \tag{2.22}$$

The swirl angle is measured from the meridional direction towards the tangential direction. This is the usual convention in the gas turbine industry, see Saravanamuttoo et al. (2009), and it bounds the flow angles to the interval $[-\frac{\pi}{2}, \frac{\pi}{2}]$. The usual convention in the steam turbine industry is to measure the swirl angle from the tangential direction and this bounds the flow angles to the interval $[0, \pi]$. The reason why the gas turbine convention was preferred is computational. As the flow angle is limited to the interval $[-\frac{\pi}{2}, \frac{\pi}{2}]$, single input[14] inverse trigonometric functions can be used directly.

Regarding the sign convention for the velocity components, the positive axial direction is taken along the shaft axis from the inlet of the turbine to the outlet and the positive radial direction is taken as the turbine radius increases. The positive circunferential direction is taken in the direction of the blade speed. The blade speed is defined by the product of the angular speed of the shaft and the local radius of the blade, as indicated by Eq. 3.76.

$$u = \omega \cdot r \tag{2.23}$$

The flow within the rotor is characterized by the relative velocity, that is, the velocity of the flow with respect to the local blade speed. Mathematically, the relative velocity is defined as the difference between the absolute velocity and the local velocity of the blade.

$$w_x = v_x \tag{2.24}$$

$$w_r = v_r = 0 \tag{2.25}$$

$$w_\theta = v_\theta - u \tag{2.26}$$

The relative flow angle is defined as the angle between the relative flow direction and the meridional direction and it is defined by Eq. 2.27.

$$\tan(\beta) = \frac{w_\theta}{v_m} = \frac{v_\theta - u}{v_m} \tag{2.27}$$

The relative and the absolute flow angles are related through Eq. 2.28.

$$\tan(\alpha) - \tan(\beta) = \frac{u}{v_m} \tag{2.28}$$

A velocity triangle illustrating the flow velocities and angles is sketched in Fig. 2.21.

[14] Most programming languages implement both *single input* and *double input* inverse trigonometric functions, such as $\arctan\theta$. Single input functions return the angle in the interval $[-\frac{\pi}{2}, \frac{\pi}{2}]$ while double input functions require an additional input to specify the quadrant of the output angle.

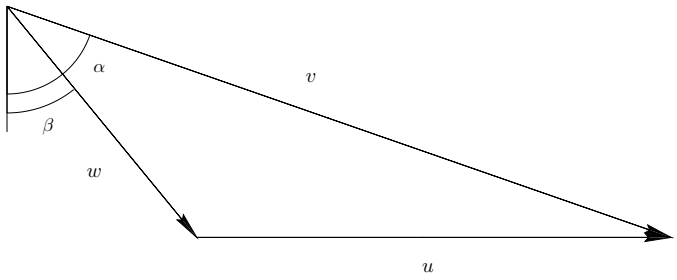

Figure 2.21: Generic velocity triangle showing the notation and conventions used in this work.

Blade description

The terminology for turbine blades follows closely the terminology of aircraft wing profiles. The origin of this terminology goes back to the decade of 1930, when the National Advisory Committee for Aeronautics – NACA performed a series of experiments using airfoil shapes designed systematically, Jacobs et al. (1933). The terminology used in this work has now become a well-known standard for airfoil profiles and turbine blades, Anderson (2010). The main geometric characteristics of a turbine blade are sketched in Fig. 2.22.

Blades are characterized by a mean camber line halfway between the suction and the pressure surfaces. The arclength of the camber line is known as the camber length, l. The most forward point of the camber line is the leading edge and the most rearward point is the trailing edge. The chord line is the straight line connecting the leading and the trailing edge. The length of the chord line is simply referred as the chord of the blade, c. The camber of the blade is the distance between the chord line and the camber line, measured perpendicular to the chord line. The thickness, t, is the distance between the pressure and suction surfaces, measured perpendicular to the camber line. The performance of a blade is highly influenced by the maximum thickness, t_{max}, and the trailing edge thickness, t_{te}.

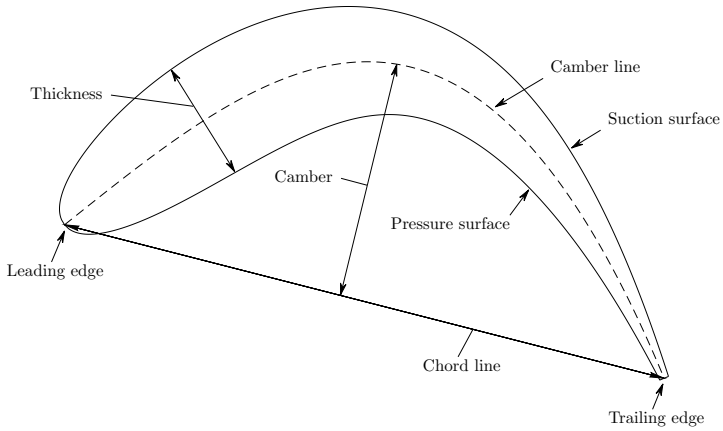

Figure 2.22: Geometry of a turbine blade.

Stage description

The main geometric characteristics of a turbine stage are sketched in Fig. 2.23. In order to deflect the flow, several turbine blades are grouped to form a cascade. The cascade of stationary blades is known as stator and the cascade of moving blades is known as rotor. A stator and a rotor cascade form a turbine stage. The axial distance between the outlet of the stator and the inlet of the rotor cascades is known as the stage spacing, ss.

The circumferential separation between two blades is known as the pitch or spacing, s. The spacing to chord ratio, s/c, is an essential parameter for the optimization of the blade cascade. Low values of the space to chord ratio imply high guidance of the flow but also high friction, while high values lead to low friction and high flow deviation. The inverse of the space to chord ratio is known as the solidity of the cascade, $\sigma = c/s$.

The angle between the chord line and the axial direction is the stagger angle or setting angle, ξ. The projection of the chord onto the axial direction is known as the axial chord, b. The spacing to axial chord ratio is defined as s/b. Chord, axial chord, and setting angle are related according to Eq. 2.29:

$$b = c \cdot \cos(\xi) \tag{2.29}$$

The relative angle of the flow at the inlet of the rotor, α_1, or rotor, β_2, should be close to the blade inlet angle, θ_1. This is the case for the design conditions, but for the case of part-load operation, there will be a positive or negative incidence, i. The incidence angle is defined as the flow inlet angle minus the blade inlet angle:

$$i = \alpha_1 - \theta_1 \qquad \text{For the case of stator blades} \tag{2.30}$$

$$i = \beta_2 - \theta_1 \qquad \text{For the case of rotor blades} \tag{2.31}$$

In general the relative angle at the outlet of the stator , α_2, or rotor, β_3, will be different than the blade outlet angle, θ_2. This is because the blades can not turn the flow completely and some deviation, δ, exists at the outlet. The deviation angle is defined as the flow outlet angle minus the blade outlet angle:

$$\delta = \alpha_2 - \theta_2 \qquad \text{For the case of stator blades} \tag{2.32}$$

$$\delta = \beta_3 - \theta_2 \qquad \text{For the case of rotor blades} \tag{2.33}$$

Finally, the opening, o, of the cascade is defined as the distance between the trailing edge of one blade and the suction surface of the next one, measured perpendicular to the outlet blade angle direction. The opening to spacing ratio is related to the blade outlet angle:

$$\frac{o}{s} \approx \cos(\theta_2) \tag{2.34}$$

The equation is only approximate because of the curvature of the suction surface.

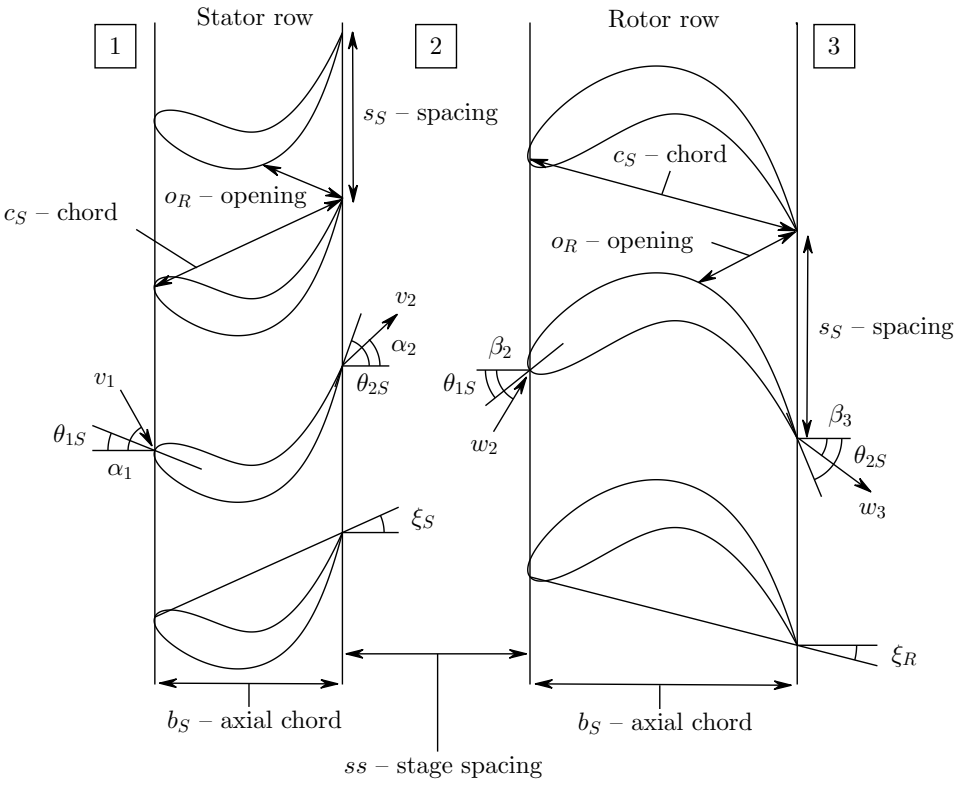

Figure 2.23: Geometry of a turbine stage.

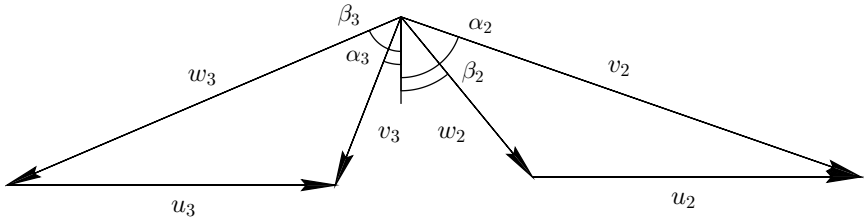

Figure 2.24: Velocity triangles for a turbine stage.

Axial turbine description

Some other geometric characteristics of a axial turbine are sketched in Fig. 2.25, where the axial view of of a three-three stage axial turbine is shown. The working fluid flows within the annular duct defined by the inner and outlet diameters. The hub is the surface defined by the inner diameter and the shroud is the surface defined by the outer diameter. The blade height is defined as the difference between the blade radius at the tip and the blade radius at the root. For the case of rotor blades, root sections are at the hub and tip sections are at the shroud, while, for stator blades, root sections are at the shroud and tip sections are at the hub.

Rotor blades are mounted to the rotating disks attached to the shaft and stator blades are mounted to the casing. The diaphragms are extensions of the stator blades that are located in between the rotor disks. The axial spacing between the rotor disks and stator diaphragms is known as disk–casing (or disk–diaphragm) clearance gap. Due to the velocity gradient between the disks and the diaphragms, some power is dissipated. This loss is known as disk–friction loss or disk–windage loss[15].

The radial spacing between the rotor blade tips and the casing is known as rotor clearance gap, $t_{cl\,R}$, and the radial spacing between the stator diaphragm and the shaft is known as stator clearance gap, $t_{cl\,S}$. The clearance loss is highly dependent upon the size of the clearance gap, see Section 2.9.1.

Axial turbines are usually flared to accommodate the changes of density during the expansion. This means that the blade height is increased along the turbine axis. The mean blade height is defined as the mean height between the inlet and the outlet.

$$H_S = \frac{H_1 + H_2}{2} \qquad \text{For the case of stator blades} \tag{2.35}$$

$$H_R = \frac{H_2 + H_3}{2} \qquad \text{For the case of rotor blades} \tag{2.36}$$

The flaring angle, δ_{fl}, should be limited to avoid flow separation close to the annulus walls, Saravanamuttoo et al. (2009). The flaring angle is defined as:

$$\tan(\delta_{fl\,S}) = \frac{H_2 - H_1}{2\,b_S} \qquad \text{For the case of stator blades} \tag{2.37}$$

$$\tan(\delta_{fl\,R}) = \frac{H_3 - H_2}{2\,b_R} \qquad \text{For the case of rotor blades} \tag{2.38}$$

The ratio of hub to tip radii, r_h/r_t, is an important parameter that influences the secondary losses of the cascade, see Section 2.9.1. Numerical values close to one imply short blades. In addition, the ratio of blade height to chord is known as the aspect ratio of the cascade, H/c. In a similar manner, the ratio of the blade height to the axial chord is known as the axial aspect ratio of the cascade, H/b.

[15] This loss is not considered in this work

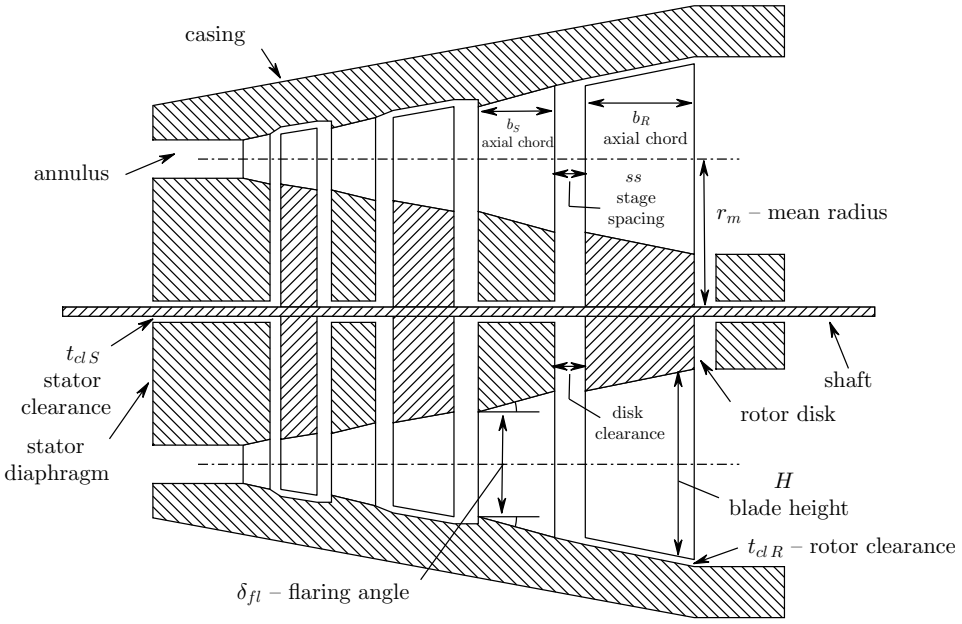

Figure 2.25: Geometry of a turbine blade.

2.8.3 Euler turbomachinery equation and rothalpy

The torque at the shaft of a turbine can be computed from the principle of angular momentum applied to a control volume containing the rotor, see Dixon and Hall (2013).

$$\tau = \dot{m} \cdot (r_2\, v_{\theta 2} - r_3\, v_{\theta 3}) \tag{2.39}$$

The power output from the rotor can be computed as the product of the torque and the angular speed:

$$\dot{W} = \omega\, \tau = \dot{m} \cdot (u_2 v_{\theta 2} - u_3 v_{\theta 3}) \tag{2.40}$$

The power from the rotor can also be obtained from the first law of thermodynamics

$$\dot{W} - \dot{Q} = \omega\, \tau = \dot{m} \cdot \left(h_2 - h_3 + \frac{1}{2} v_2^2 - \frac{1}{2} v_3^2 \right) \tag{2.41}$$

For the case of an adiabatic turbine, $\dot{Q} = 0$, combining Eq. 2.40 and Eq. 2.41 reveals the following relation:

$$h_2 + \frac{1}{2} v_2^2 - u_2\, v_{\theta 2} = h_3 + \frac{1}{2} v_3^2 - u_3\, v_{\theta 3} \tag{2.42}$$

The meaning of Eq. 2.42 is that, for any adiabatic rotating machine, there exists a property that is conserved. This property is known as rothalpy, I, and it is defined by Eq. 2.43.

$$I = h + \frac{1}{2} v^2 - u\, v_\theta \tag{2.43}$$

The definition of rothalpy given by Eq. 2.43 can be expressed in terms of the relative velocity after some algebra. The final result of these manipulations is given by Eq. 2.44

$$I = h + \frac{1}{2} w^2 - \frac{1}{2} u^2 \tag{2.44}$$

For the case of a purely axial turbine the blade velocity at the mean radius is equal at any axial section, $u = \text{constant}$, and the conservation of rothalpy can be intepreted as the conservation of the relative stagnation enthalpy:

$$h_{0,rel} = h + \frac{1}{2} w^2 = \text{constant} \tag{2.45}$$

Eq. 2.45 is an useful relation to compute the enthalpy at the outlet of a turbine rotor, given the enthalpy at the inlet and the relative velocities at the inlet and the outlet and it will be used in the turbine optimization algorithm described in Sec 3.4.5

2.8.4 Stage design parameters

According to Dixon and Hall (2013) and Saravanamuttoo et al. (2009), there are three main non-dimensional parameters that define the performance of an axial turbine stage: the flow coefficient, the work coefficient and the reaction ratio.

The classic assumption for the mean–line analysis of axial turbines is that the axial velocity, v_x, and the blade velocity, u, at the mean section are constant along the turbine. This assumption will be used in the rest of this work and the possibility to change the axial velocity or to use non–symmetric flaring[16] will not be investigated.

Flow coefficient

The flow coefficient is defined as the ratio of the meridional velocity to the blade speed. For a purely axial turbine the meridional velocity is equal to the axial velocity.

$$\phi = \frac{v_m}{u} = \frac{v_x}{u} \tag{2.46}$$

Low values of ϕ imply flow angles closer to the tangential direction (highly skewed velocity triangles) while high values lead to flow angles closer to the axial direction. This is illustrated in Fig. 2.26, where the velocity triangles for three representative values of ϕ are plotted. This figure was prepared using the equations presented in Section. 2.8.5.

In the case when the values of ϕ are low, the deflection of the flow is high and the turbine stage is said to be highly loaded. Highly loaded stages lead to more compact turbines but lower isentropic efficiencies.

Work coefficient

The work coefficient, also known as stage loading coefficient, is defined as the ratio of the stagnation enthalpy change across the stage to the square of the blade speed.

$$\psi = \frac{\Delta h_0}{u^2} \tag{2.47}$$

For a purely axial turbine with constant radius, the Euler turbomachinery equation can be used to reduce the previous expression to:

$$\psi = \frac{\Delta v_\theta}{u} \tag{2.48}$$

High values of ψ imply flow angles closer to the tangential direction while low values lead to flow angles closer to the axial direction. This is illustrated in Fig. 2.27, where the velocity triangles for three representative values of ψ are plotted.

In the case when the values of ψ are high, the deflection of the flow is high and the turbine stage is highly loaded, leading to fewer stages and lower isentropic efficiencies.

[16] Non–symmetric flaring leads to changes in the blade velocity along the turbine.

Degree of reaction

The degree of reaction, also known as reaction ratio or stage reaction, is defined as the ratio of the static enthalpy drop in the rotor to the static enthalpy drop in the stage:

$$R = \frac{h_2 - h_3}{h_1 - h_3} \tag{2.49}$$

The degree of reaction is a measure of the asymmetry of the velocity triangles and it is related to the ratio of pressure drop in the rotor to the pressure drop in the stage:

$$R \approx \frac{p_2 - p_3}{p_1 - p_3} \tag{2.50}$$

The effect of the reaction ratio on the stage velocity diagrams is illustrated in Fig. 2.26, where the velocity triangles are plotted for five values of the reaction ratio between zero and one. The reaction ratio of turbine stages is often close to $R = 0.50$. This value of reaction ratio leads to symmetrical velocity triangles.

Turbine stages where the reaction ratio is lower than $R = 0.50$ are known as impulse stages. Most of the pressure drop of an impulse stage occurs in the stator while the pressure in the rotor remains more or less constant. In impulse stages, the flow deflection in low is the stator and high in the rotor.

Turbine stages where the reaction ratio is higher than $R = 0.50$ are known as reaction stages. Most of the pressure drop of a reaction stage occurs in the rotor while the pressure in the stator remains more or less constant. In reaction stages, the flow deflection is high in the stator and low in the rotor.

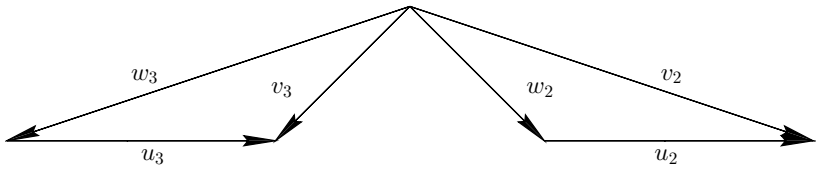

$\phi = 0.50 \qquad \psi = 2.00 \qquad R = 0.50$

(a)

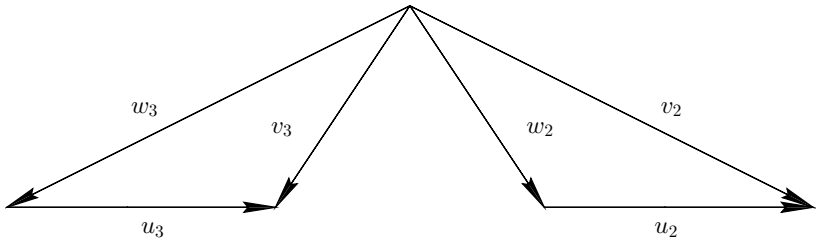

$\phi = 0.75 \qquad \psi = 2.00 \qquad R = 0.50$

(b)

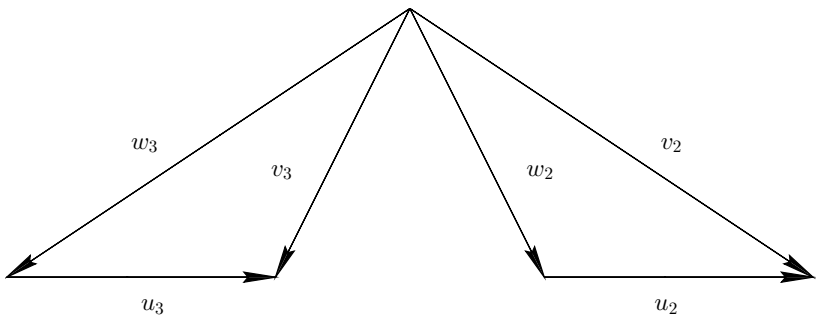

$\phi = 1.00 \qquad \psi = 2.00 \qquad R = 0.50$

(c)

Figure 2.26: Shape of the velocity triangles as a function of ϕ.

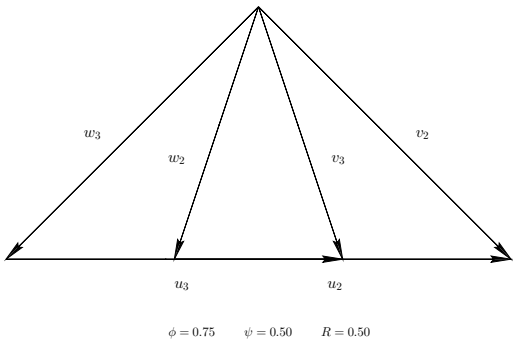

$\phi = 0.75$ $\psi = 0.50$ $R = 0.50$

(a)

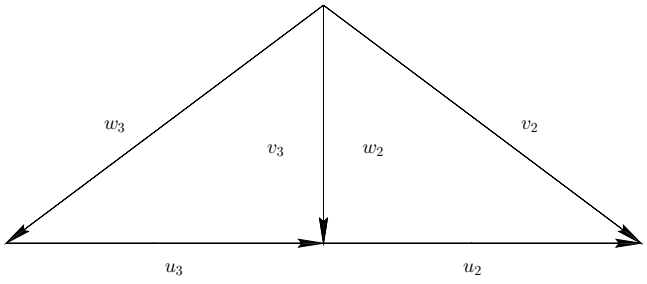

$\phi = 0.75$ $\psi = 1.00$ $R = 0.50$

(b)

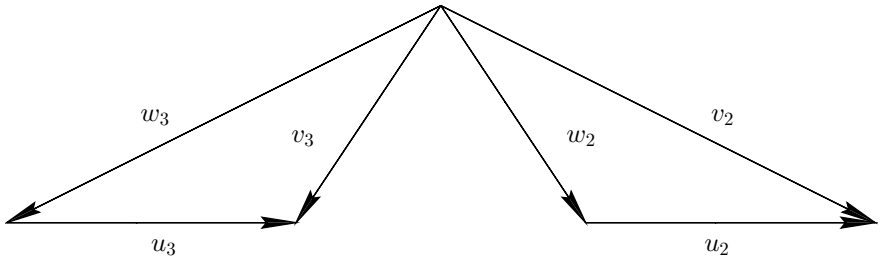

$\phi = 0.75$ $\psi = 2.00$ $R = 0.50$

(c)

Figure 2.27: Shape of the velocity triangles as a function of ψ.

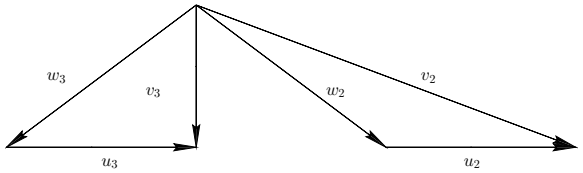

$\phi = 0.75 \qquad \psi = 2.00 \qquad R = 0.00$

(a)

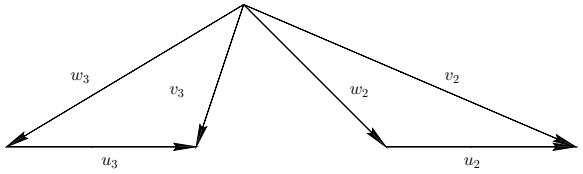

$\phi = 0.75 \qquad \psi = 2.00 \qquad R = 0.25$

(b)

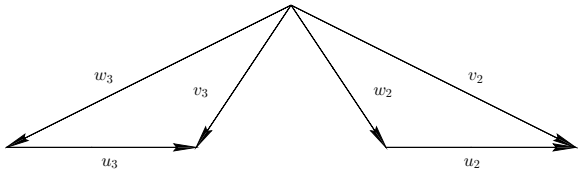

$\phi = 0.75 \qquad \psi = 2.00 \qquad R = 0.50$

(c)

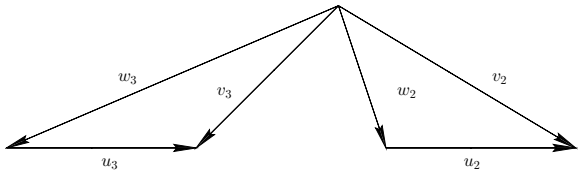

$\phi = 0.75 \qquad \psi = 2.00 \qquad R = 0.75$

(d)

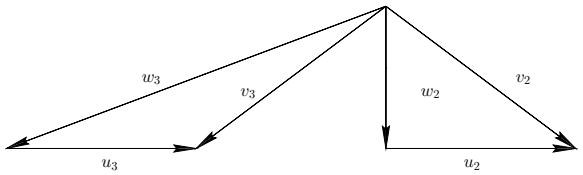

$\phi = 0.75 \qquad \psi = 2.00 \qquad R = 1.00$

(e)

Figure 2.28: Shape of the velocity triangles as a function of R.

2.8.5 Repeating turbine stages

Axial turbines usually have more than one stage and they are usually designed to have the same velocity triangles for all stages, Dixon and Hall (2013). The velocity triangles will be the same for all stages if and only if the following conditions are fulfilled:

$$v_x = \text{constant} \tag{2.51}$$

$$u = \text{constant} \tag{2.52}$$

$$\alpha_1 = \alpha_3 \tag{2.53}$$

If these conditions are met, the stages of the axial turbine are known as repeating stages or normal stages. Using the definitions of flow coefficient, work coefficient, and degree of reaction and doing some algebraic manipulations[17], the following relation to compute the absolute and relative flow angles can be proven for a repeating stage:

$$\tan(\alpha_2) = \frac{1}{\phi}\left(1 - R + \psi/2\right) \tag{2.54}$$

$$\tan(\alpha_3) = \frac{1}{\phi}\left(1 - R - \psi/2\right) \tag{2.55}$$

$$\tan(\beta_2) = -\frac{1}{\phi}\left(R - \psi/2\right) \tag{2.56}$$

$$\tan(\beta_3) = -\frac{1}{\phi}\left(R + \psi/2\right) \tag{2.57}$$

Eqs. 2.54 – 2.57 indicate that the flow angles of repeating stages are completely determined by the values of ϕ, ψ, and R.

2.8.6 Number of stages

Once the number of stages of the turbine, n, is set; the blade speed can be determined from the enthalpy drop in the turbine, Δh_0, (obtained from the cycle optimization) and the definition work coefficient:

$$u = \sqrt{\frac{\Delta h_0}{n \cdot \psi}} \tag{2.58}$$

Absolute and relative velocities follow easily from the flow angles determined using the stage design parameters. Designs with a large number of stages will be more efficient while turbines with few stages (or even single-stage turbines) will be more compact. The impact of the number of stages on the turbine design is discussed in Sec. 4.4.

[17] The algrebra can be found in Saravanamuttoo et al. (2009) or in Dixon and Hall (2013)

2.8.7 Specific parameters

The blade speed is defined by the mean radius and the angular speed of the shaft:

$$u = \omega \cdot r_m \tag{2.59}$$

Either the angular speed or the mean radius can be determined from the blade speed if the other one is specified. The optimal angular velocity and mean radius can change a lot from case to case (even by orders of magnitude) and it is not straightforward to give a good initial guess for any of these two variables.

However, it is possible to use parameters from the cycle optimization to scale these variables and form dimensionless groups. Two possible dimensionless parameters are the specific speed, ω_s, and the specific diameter, d_s:

$$\omega_s = \omega \cdot \frac{\dot{V}_{out,s}{}^{1/2}}{\Delta h_{0s}^{3/4}} = \omega \cdot \frac{(\dot{m}_{out}/\rho_{out,s})^{1/2}}{(h_{0,in} - h_{0,out,s})^{3/4}} \tag{2.60}$$

$$d_s = 2\, r_m \cdot \frac{\Delta h_{0s}^{1/4}}{\dot{V}_{out,s}{}^{1/2}} = 2\, r_m \cdot \frac{(h_{0,in} - h_{0,out,s})^{1/4}}{(\dot{m}_{out}/\rho_{out,s})^{1/2}} \tag{2.61}$$

The definition of these parameters follows from dimensional analysis when the isentropic volumetric flow at the outlet of the turbine, $\dot{V}_{out,s} = \dot{m}_{out}/\rho_{out,s}$, and the isentropic enthalpy change across the turbine, $\Delta h_s = (h_{in} - h_{out,s})$, are used to reduce the dimensions of the angular speed and the mean radius.

The specific speed and diameter are commonly used in the similarity study of turbomachinery, see Balje (1962). However, these parameters are not frequently used for the optimization of turbines. Despite this, the writer believes that they are useful because they scale the angular speed and the mean radius using variables from the cycle. This makes it easier to give an initial value[18] and reduces the numerical errors during the optimization

In this work, the specific speed was specified as a degree of freedom and the angular speed followed from the parameters of the cycle optimization:

$$\omega = \omega_s \cdot \frac{(h_{0,in} - h_{0,out,s})^{3/4}}{(\dot{m}_{out}/\rho_{out,s})^{1/2}} \tag{2.62}$$

The mean radius can then be obtained from the blade speed. Using the specific diameter as degree of freedom would be equivalent, but the specific speed was chosen because it is more common in the literature, to the best knowledge of this author.

[18] As a very rough rule, the specific diameter and speed will lie in the range 0–10.

2.9 Losses in axial turbines

A loss can be defined as any flow feature that reduces the power output from the turbine. Turbine losses can be classificed into two main categories, see Craig and Cox (1970) or Aungier (2006):

1. Losses that reduce the amount of energy transferred from the fluid to the rotor.
2. Other losses that reduce the amount of work available at the shaft coupling.

Losses can be quantified using different definitions, including the stagnation pressure loss coefficient or the enthalpy loss coefficient. In this section, the main losses in axial turbines are described and the loss coefficient definitions considered in this work are discussed. The second type of losses are not considered in the optimization algorithm of this work but they are included in this section for the sake of completeness. The empirical correlations used to estimate the loss coefficients are presented in Section. 2.10.

2.9.1 First type of losses

The first type of losses are caused by irreversible processes that lead to entropy generation within the flow. Some of the irreversible processes that lead to entropy generation in turbomachinery include viscous friction in boundary layers or free shear layers, heat transfer across finite temperature differences[19], and shock waves in high speed flows. As discussed in Section. 2.6.1., the energy transferred from the fluid to the rotor is maximum for an isentropic process and any increase of entropy within the flow will reduce the power output from the turbine. Traditionally, losses of the first type are divided into different components and analyzed independently[20]. These loss components include profile losses, secondary losses, clearance gap losses, trailing edge losses, and shock losses.

Profile loss

Profile loss is the loss generated in the blade boundary layers far away from the end walls (hub and tip). This loss is mostly affected by the incidence angle, flow deflection, blade thickness, chord length, and spacing between blades. The profile loss is small when the pressure gradient is favorable (the pressure decreases in the direction of the flow) and it is high for adverse pressure gradients. This is the reason why profile losses are higher for impulse stages than for reaction stages. The pressure in a impulse stage is more or less constant, while reaction stages always have favorable pressure gradients.

Secondary loss

Secondary loss, also known as end wall loss, is the loss generated in annulus boundary layers. This loss is localized at the tip and hub of the cascades and it is mainly influenced by the aspect ratio of the cascade and the blade loading (see *Ainley loading parameter* in Section. 2.10).

[19] This mechanism of entropy generation is relevant in gas turbines with blade cooling.

[20] Despite the historical breakdown of losses into different components, the different loss mechanisms are seldom really independent in practice, see Denton (1993).

Clearance loss

Clearance loss is the loss generated by the leakage flow over the tip clearances of the rotor blades. This loss is mainly influenced by clearance thickness, aspect ratio, and whether the blades are shrouded or not. The leakage loss associated with the stator clearance gap is ignored in all loss systems, to the best knowledge of the writer.

Trailing edge loss

This loss includes the entropy generated within trailing edge vortices shed by the blades and the mixing of the boundary layers of the upper and lower surfaces of the blades. This loss is mostly influenced by the trailing edge thickness, spacing, and opening.

Shock wave losses

This loss is associated with the entropy generated across shock waves within the flow. Shock waves are irreversible flow discontinuities[21] that can arise close to boundaries in supersonic flows. The magnitude of these losses increases as the Mach number of the flow increases. A shock wave in the suction surface of the blades may lead to the separation of the boundary layer due to the increase in static pressure. This is known as shock wave – boundary layer interaction and it leads to additional losses.

2.9.2 Second type of losses

The second type of losses are also known as parasitic losses and they include mechanisms that reduce the power output of the turbine but do not interfere with the flow within the blade rows. For this reason the second type of losses do not influence the isentropic efficiency of the turbine. These losses include bypass losses, disk friction losses, and clearance gap windage losses.

Bypass loss

Not all of the mass flow rate passes through the rotor blades, for instance, the leakage flow on the rotor blade tips does not do any work on the blades. The bypass loss accounts for the reduction of output power that occurs when part of the mass flow rate bypasses the rotor blades. This loss is mainly influenced by the tip clearance thickness and the geometry of the sealings.

Disk friction loss

Disk friction loss accounts for the power dissipated due to the velocity gradient in the clearance between the stator diaphragms and the rotor disk walls. The main factors that influence these losses are the disk radius, the speed of rotation, the clearance thickness between rotor and stator, and the viscosity of the fluid.

[21] Physically, shock waves are not real discontinuities. They are regions with a thickness of few mean molecular free paths and large property gradients. The entropy generation occurs due to heat conduction and viscous stresses within the shock wave. Despite this, shock waves are treated as discontinuities in most applications.

Clearance gap windage loss

This loss accounts for power dissipated due to the shear forces that exist between the rotor blade tips and casing and between stator diaphragms and shaft. This loss is mainly influenced by the clearance thickness between solid surfaces, the mean radius of the gap, the speed of rotation, and the viscosity of the fluid.

2.9.3 Definition of the loss coefficient

In this section two different definitions of the loss coefficient for rotor and stator cascades are presented and the advantages and disadvantages of each definition are discussed.

Stagnation pressure loss coefficient

There are many different ways to define the loss coefficients for a cascade. Perphaps, the most common loss coefficient is the stagnation pressure loss coefficient, see Denton (1993) or Saravanamuttoo et al. (2009). It is defined as the ratio of the difference in stagnation pressure between the inlet and the outlet of the cascade to the dynamic pressure at the outlet of the cascade. The definition of this coefficient for stator and rotor rows is given by Eq. 2.63 and Eq. 2.64, respectively

$$Y_S = \frac{p_{01} - p_{02}}{p_{02} - p_2} \tag{2.63}$$

$$Y_R = \frac{p_{02,rel} - p_{03,rel}}{p_{03,rel} - p_3} \tag{2.64}$$

From these definitions, it follows that the stagnation pressure drop across the cascade is proportional to the dynamic pressure at the outlet of the cascade. This can be recognized rearranging Eq. 2.63 and Eq. 2.64 into Eq. 2.65 and Eq. 2.66.

$$p_{02} = p_{01} - Y_S \cdot (p_{02} - p_2) \tag{2.65}$$

$$p_{03,rel} = p_{02,rel} - Y_R \cdot (p_{03,rel} - p_3) \tag{2.66}$$

This definition of loss coefficient is commonly adopted because it is relatively easy to calculate from cascade test data. One of the limitations of this definition is that it is not valid for radial turbines, although this is not a concern for the scope of this work.

Enthalpy loss coefficient

A different definition of the loss coefficient that is more useful for design purposes is the enthalpy loss coefficient (also known as energy loss coefficient), see Denton (1993) or Saravanamuttoo et al. (2009). The enthalpy loss coefficient is defined as the ratio of the difference of actual and isentropic enthalpies at the outlet of the cascade to the specific kinetic energy at the outlet of the cascade. The definition of this coefficient for stator and

rotor rows is given by Eq. 2.67 and Eq. 2.68.

$$\zeta_S = \frac{h_2 - h_{2s}}{\frac{1}{2}{v_2}^2} \tag{2.67}$$

$$\zeta_R = \frac{h_3 - h_{3s}}{\frac{1}{2}{w_3}^2} \tag{2.68}$$

From the definition of the enthalpy coefficient, it follows that the difference between the actual and the isentropic enthalpies at the outlet is proportional to the kinetic energy at the outlet of the cascade. This can be recognized rearranging Eq. 2.67 and Eq. 2.68 into Eq. 2.69 and Eq. 2.70.

$$h_2 = h_{2s} + \zeta_S \cdot \frac{1}{2}{v_2}^2 \tag{2.69}$$

$$h_3 = h_{3s} + \zeta_R \cdot \frac{1}{2}{w_3}^2 \tag{2.70}$$

Most of the empirical correlations used to estimate the losses during the design phase, including those presented Section 2.10, were originally developed for the stagnation pressure loss coefficient Y. This is because these correlations are based on experimental cascade data. Despite this, the definition of loss based on the enthalpy loss coefficient ζ will be used in the remainder of this work because it is more convenient during the design phase.

In this work the symbol Y will be used indistinctly for the stagnation pressure and enthalpy loss coefficients. This does not lead to important errors because the numerical value of both coefficients is very similar, specially at low Mach numbers. A formal justification of this claim can be found in Saravanamuttoo et al. (2009). Using perfect gas relations and taking only the first term of a binomial expansion, it can be proven that:

$$Y \approx (1 + \frac{\gamma - 1}{2}\mathrm{Ma}^2) \cdot \zeta \tag{2.71}$$

In this equation, Ma is the Mach number at the outlet of the cascade. In the limit when $\mathrm{Ma} \to 0$, that is, in the incompressible flow limit, $Y \approx \zeta$. Similarly, in the limit when $\gamma \to 1$, such as for turbines using complex organic substances as working fluid, $Y \approx \zeta$.

The reason why the enthalpy loss coefficient is more convenient during the design phase will be apparent when the optimization algorithm for axial turbines is described in Section 3.4.5. Other definitions of the loss coefficient such as the entropy loss coefficient, see Denton (1993), were not considered in this work.

2.10 Correlations for axial turbine losses

The loss systems considered in this work are based in the correlations presented in Ainley and Mathieson (1951a) and Ainley and Mathieson (1951b). These correlations became very popular for the preliminary design of axial turbines and were refined during the years. These improvements are described in the works by Dunham and Came (1970) and by Kacker and Okapuu (1982).

The Ainley-Mathieson and its derivatives are mean-line performance analyses that evaluate all losses at a single reference radius. This reference radius is taken as the arithmetic mean of the hub and tip radii, $r_m = (r_h + r_t)/2$. Other popular methods, as the one presented by Craig and Cox (1970), or the one proposed by Aungier (2006), are hub-to-shroud performance analyses that consider the geometry and losses at several radial locations along the blades. The advantage of hub-to-shroud methods is that they provide more data for the later stages of the turbine design. Of course, hub-to-shroud methods are also more complex than mean-line methods and the turbine designer has to analyze more variables in the early stages of the design. This writer decided to use a mean-line performance analysis because the scope of this work is to carry on a preliminary design of axial turbines for Rankine cycles.

In this section, the Ainley-Mathieson loss system and improvements by Dunham-Came and Kacker-Okapuu are described. The equations and graphs of these methods are adapted in this section to match the notation and sign conventions used in this work. The correlations are presented for rotor cascades, but they are also valid for stator cascades replacing the relative variables w and β by the absolute variables v and α and the subscripts 2 and 3 by 1 and 2, respectively. The three loss methods are available in the MATLAB optimization program developed in this work, but the Kacker-Okapuu improvement is expected to be the most accurate.

2.10.1 Ainley-Mathieson loss system

Description

The Ainley-Mathieson loss system (sometimes abbreviated as AM) was presented in Ainley and Mathieson (1951a) and Ainley and Mathieson (1951b). This method is a mean-line loss system developed to estimate the performance of axial turbines both for design and off-design conditions. The losses are evaluated at zero incidence ($i = 0$) and then corrected for cascades operating at positive or negative incidences. The effect of the incidence is not considered in this work because the optimization is performed only for the design conditions for which $i = 0$ in each blade cascade.

The general form of the Ainley-Mathieson loss system is:

$$Y = (Y_p + Y_s + Y_{cl}) \cdot y_{te} \tag{2.72}$$

Where y_{te} is not the trailing edge loss coefficient, but a multiplication factor to account for the trailing edge losses.

Profile loss

The profile loss coefficient at zero incidence is given by:

$$Y_p = \left[Y_{p,\,reaction} + \left(\frac{\beta_2}{\beta_3} \right)^2 \cdot \left(Y_{p,\,impulse} - Y_{p,\,reaction} \right) \right] \cdot \left(\frac{t_{max}/c}{0.20} \right)^{-\beta_2/\beta_3} \tag{2.73}$$

Essentially, Eq. 2.73 computes the profile loss coefficient of the cascade interpolating the loss coefficients of reaction and impulse cascades. The factor $Y_{p,\,reaction}$ is the profile loss coefficient of an axial entry reaction cascade, $\alpha_1 = 0$ for the case of stator blades and $\beta_2 = 0$ for the case of rotor blades. Similarly, the factor $Y_{p,\,impulse}$ is the profile loss coefficient of an impulse cascade having $\alpha_1 = -\alpha_2$ for the case of stator blades or $\beta_2 = -\beta_3$ for the case of rotor blades. Both coefficients are a function of the pitch to chord ratio and the outlet flow angle. The functional relation was presented graphically in the original work of Ailey and Mathieson and it is reproduced in Fig. 2.29 and Fig. 2.30.

The last term of the right hand side of Eq. 2.73 is a correction factor to account for the maximum thickness of the blades for the range $0.15 \leq t_{max}/c \leq 0.25$. If $t_{max}/c \leq 0.15$ or $t_{max}/c \geq 0.25$, then t_{max}/c should be taken equal to 0.15 or 0.25, respectively.

Secondary loss

The secondary loss coefficient is computed according to:

$$Y_s = \lambda \cdot Z \tag{2.74}$$

Where Z is known as the Ainley loading parameter, defined as:

$$Z = \left(\frac{C_L}{s/c} \right)^2 \frac{\cos(\beta_3)^2}{\cos(\beta_m)^3} \tag{2.75}$$

$$\left(\frac{C_L}{s/c} \right) = 2\cos(\beta_m)\ \left[\tan(\beta_2) - \tan(\beta_3) \right] \tag{2.76}$$

$$\tan(\beta_m) = \frac{1}{2} \left[\tan(\beta_2) + \tan(\beta_3) \right] \tag{2.77}$$

The parameter λ is a function of the cascade geometry:

$$\lambda = \lambda \left[\left(\frac{A_3 \cos(\beta_3)}{A_2 \cos(\beta_2)} \right)^2 / \left(1 + \frac{r_h}{r_t} \right) \right] \tag{2.78}$$

$$\frac{r_h}{r_t} = \frac{r_m - H/2}{r_m + H/2} \tag{2.79}$$

H denotes the mean blade height of the cascade. Ainley and Mathieson gave the functional relation for λ in graphical form, see Fig. 2.31.

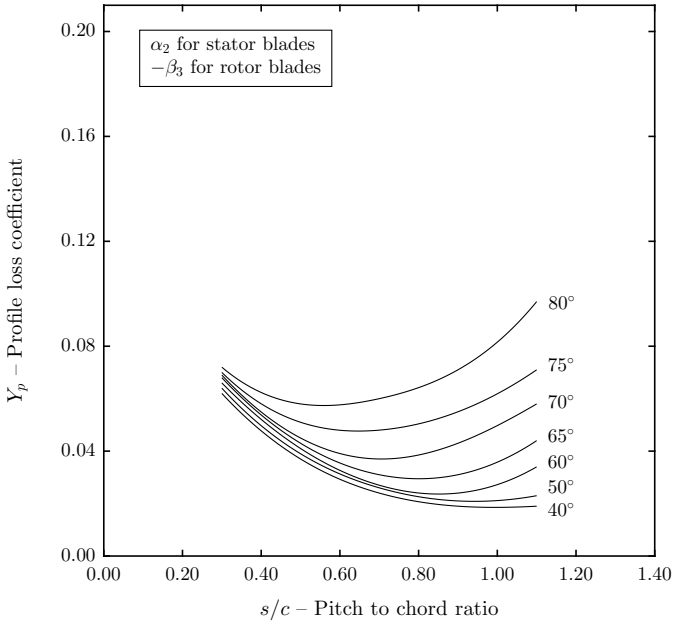

Figure 2.29: Profile loss of reaction blades.

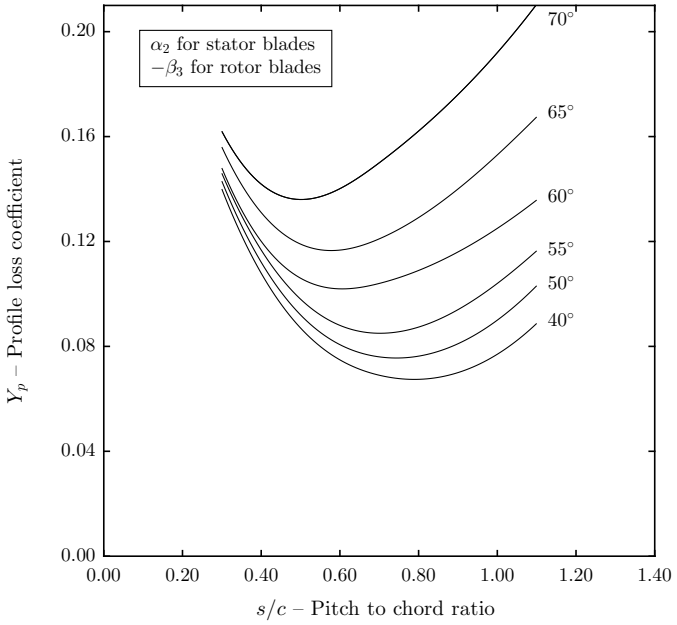

Figure 2.30: Profile loss of impulse blades.

Clearance loss

The clearance loss coefficient for a rotor cascade is computed according to:

$$Y_{cl} = B \cdot Z \cdot \left(\frac{t_{cl}}{H} \right) \tag{2.80}$$

Where Z is given by Eqs. 2.75 to 2.77.

The empirical parameter B is 0.50 for rotor blades with radial tip clearance and 0.25 for shrouded rotor blades. The clearance loss is negligible for stator blades with diaphragm extensions between the disks, see Fig. 2.25. In other words, $B = 0.00$ for stator cascades.

Trailing edge loss

The original Ainley-Mathieson loss system does not use a trailing edge loss coefficient, instead, it uses a multiplication factor y_{te} to account for the trailing edge losses, as indicated in Eq. 2.72. Multiplication factor is a function of the ratio of trailing edge thickness and blade spacing only:

$$y_{te} = y_{te}(t_{te}/s) \tag{2.81}$$

Ainley and Mathieson gave functional relation for y_{te} in graphical form, see Fig. 2.32.

Reynolds number correction factor

The method accounts for the effects of the Reynolds number applying a correction factor to the overall turbine efficiency:

$$(1 - \eta) = \left(\frac{\mathrm{Re}}{2 \cdot 10^5} \right)^{-1/5} \cdot (1 - \eta)_{\mathrm{Re}=2 \cdot 10^5} \tag{2.82}$$

This correction factor is recommended for Reynolds numbers as low as $\mathrm{Re} = 1 \cdot 10^4$. The exact definition of the turbine efficiency is not reported. The Reynolds number is defined as the arithmetic mean of the first stator and last rotor Reynolds numbers. The characteristic length for the Reynolds number is the blade chord and the density, viscosity, and velocity are evaluated at the outlet of the cascade.

$$\mathrm{Re} = (\mathrm{Re}_S + \mathrm{Re}_R)/2 \tag{2.83}$$

$$\mathrm{Re}_S = \frac{\rho_2 \, v_2 \, c_S}{\mu_2} \tag{2.84}$$

$$\mathrm{Re}_R = \frac{\rho_3 \, w_3 \, c_R}{\mu_3} \tag{2.85}$$

The Reynolds correction factor proposed in the Ainley-Mathieson loss system is quite rough and dated. It was presented to compare it with the Reynolds number correction factors of the Dunham-Came and Kacker-Okapuu loss systems.

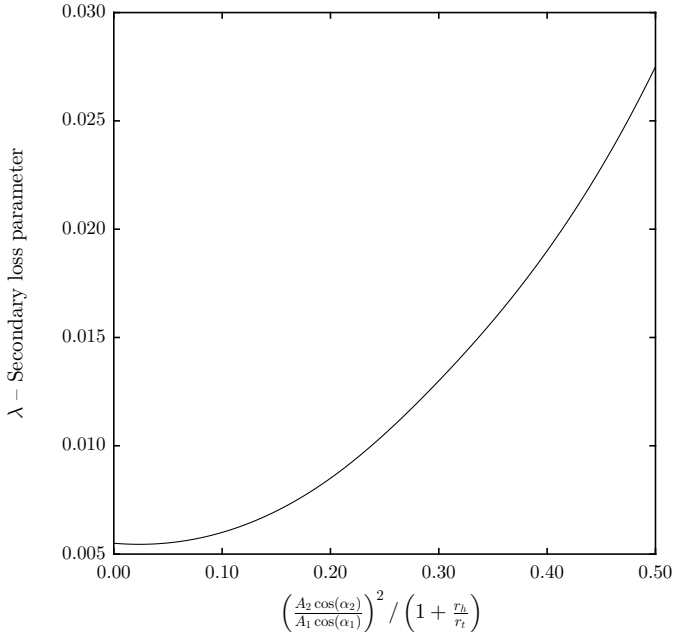

Figure 2.31: Secondary loss parameter.

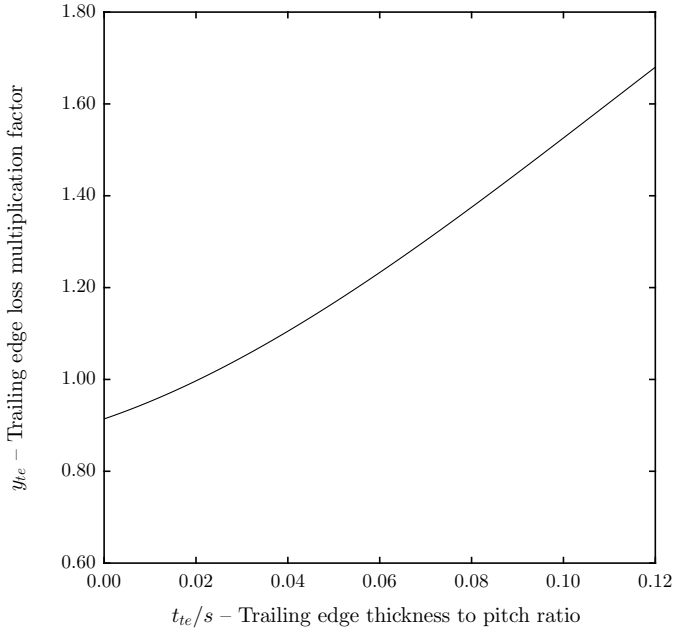

Figure 2.32: Trailing edge loss multiplication factor.

2.10.2 Dunham-Came loss system

The Dunham-Came loss system (sometimes abbreviated as AMDC) was presented in Dunham and Came (1970) and it is a refinement of the Ainley-Mathieson loss system. This method is also a mean-line loss system to estimate the performance of axial turbines both for design and off-design conditions.

The general form of the Dunham-Came loss system is

$$Y = (f_{\mathrm{Re}}\, f_{\mathrm{Ma}}\, Y_p + f_{\mathrm{Re}}\, Y_s + Y_{cl}) \cdot y_{te} \tag{2.86}$$

The Reynolds correction factor of the Ainley-Mathieson method affected the overall turbine efficiency while the Reynolds correction factor of the Dunham-Came method, f_{Re}, corrects the profile and secondary loss coefficients. In addition, the Dunham-Came loss system proposes a Mach number correction factor for the profile losses and new correlations for secondary and clearance losses.

Profile loss

As in the Ainley-Mathieson method, the profile loss coefficient, Y_p is given by Eq. 2.73. In addition, a correction factor, f_{Ma}, is used to account for the development of shock waves at the outlet of the row when the Mach number is larger than one:

$$f_{\mathrm{Ma}} = \begin{cases} 1 & \text{for} \quad \mathrm{Ma}_{3,\mathrm{rel}} \leq 1 \qquad (2.87) \\ 1 + 60 \cdot (\mathrm{Ma}_{3,\mathrm{rel}} - 1)^2 & \text{for} \quad \mathrm{Ma}_{3,\mathrm{rel}} > 1 \qquad (2.88) \end{cases}$$

$\mathrm{Ma}_{3,\mathrm{rel}}$ is the relative Mach number at the outlet of the rotor, Eq. 2.89.

$$\mathrm{Ma}_{3,\mathrm{rel}} = w_3 / a_3 \tag{2.89}$$

The variation of the correction factor upon the Mach number is shown in Fig. 2.33. This correction factor penalizes heavily supersonic velocities at the outlet of the row. Dunham and Came stated that the correlation for f_{Ma} is based on insufficient experimental data.

Secondary loss

The secondary loss coefficient for a stator cascade is computed according to:

$$Y_s = 0.0334 \cdot Z \cdot \frac{\cos(\beta_3)}{\cos(\beta_2)} \left(\frac{c}{H}\right) \tag{2.90}$$

Where Z is given by Eqs. 2.75 to 2.77.

Unlike the secondary loss coefficient of the Ainley-Mathieson method, the secondary loss coefficient of the Dunham-Came system depends upon the aspect ratio of the blades.

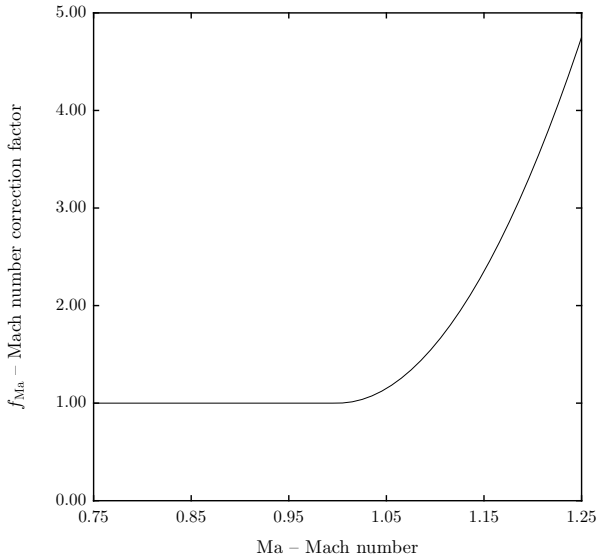

Figure 2.33: Correction factor for the Mach number.

Tip clearance loss

The clearance loss coefficient for a stator or a rotor stage is computed according to:

$$Y_{cl} = B \cdot Z \cdot \left(\frac{c}{H}\right) \cdot \left(\frac{t_{cl}}{H}\right)^{0.78} \tag{2.91}$$

Where Z is given by Eqs. 2.75 to 2.77.

The Dunham-Came loss system proposes $B = 0.47$ for rotor blades with plain tip, $B = 0.37$ for rotor blades with shrouded tips, and $B = 0.00$ for stator blades.

Trailing edge loss

The trailing edge loss is computed in the same way as in the AM loss system.

Reynolds number correction factor

The Reynolds number correction factor that affects the profile and the secondary loss, see Eq. 2.86, is computed according to:

$$f_{\mathrm{Re}} = \left(\frac{\mathrm{Re}}{2 \cdot 10^5}\right)^{-0.20} \tag{2.92}$$

In this equation, the Reynolds number is defined using the blade chord and the relative speed, viscosity, and density at the outlet of the cascade.

$$\mathrm{Re} = \frac{\rho_3 \, w_3 \, c}{\mu_3} \tag{2.93}$$

2.10.3 Kacker-Okapuu loss system

The Kacker-Okapuu loss system (sometimes abbreviated as AMDCKO) was presented in Kacker and Okapuu (1982) and it is a further improvement of the Ainley-Mathieson loss system. This method is also a mean-line loss system to estimate the performance of axial turbines only for design conditions.

The general form of the Dunham-Came loss system is:

$$Y = f_{\mathrm{Re}}\, f_{\mathrm{Ma}}\, Y_p + Y_s + Y_{cl} + Y_{te} \tag{2.94}$$

There are two main differences between the Dunham-Came and the Kacker-Okapuu loss systems: the trailing edge loss is accounted independently with a loss coefficient, Y_{te}, instead of the factor multiplication y_{te} and the Reynolds number correction factor only affects the profile loss and not the secondary loss.

Profile loss

The profile loss computed according to:

$$Y_p = 0.914 \cdot \left(\frac{2}{3} \cdot Y'_p \cdot K_p + Y_{shock} \right) \tag{2.95}$$

The Ainley-Mathieson and Dunham-Came methods assumed blades having a trailing edge thickness to pitch ratio, t_{te}/s, equal to 0.02 and used a multiplication factor to account for the trailing edge losses at other values of trailing edge thickness to pitch ratio. In the Kacker-Okapuu method, trailing edge losses are accounted independently and the profile loss is corrected to blades having zero trailing edge thickness with the factor 0.914.

The term 2/3 is included to account for advances in blade aerodynamic design during the time interval since the Ainley-Mathieson method was published, 1951, to the year when the Kacker-Okapuu was developed, 1982.

The term Y'_p is given by Eq. 2.96. This expression is similar to that of the Ainley-Mathieson and Dunham-Came loss systems. The new term $|\beta_2/\beta_3|$ is included to allow negative angles at the inlet of the rotor (and positive angles at the inlet of the stator). As in the Ainley-Mathieson method, $Y_{p,\,reaction}$ and $Y_{p,\,impulse}$ are be obtained from the graphical data presented in Fig. 2.29 and Fig. 2.30.

$$Y'_p = \left[Y_{p,\,reac} - \left(\frac{\beta_2}{\beta_3} \right) \left| \frac{\beta_2}{\beta_3} \right| \cdot (Y_{p,\,imp} - Y_{p,\,reac}) \right] \cdot \left(\frac{t_{max}/c}{0.20} \right)^{-\beta_2/\beta_3} \tag{2.96}$$

The factor K_p accounts for compressible flow effects when the Mach number within the cascade is subsonic but larger than one. These effects tend to accelerate the flow, make the boundary layers thinner, and decrease the profile losses. K_p is a function on the inlet and outlet Mach numbers and it is computed from Eqs. 2.97 to 2.101.

$$K_p = 1 - K_2 \cdot (1 - K_1) \tag{2.97}$$

$$K_1 = \begin{cases} 1 & \text{for} \quad \mathrm{Ma}_{3,rel} < 0.20 \quad (2.98) \\ 1 - 1.25 \cdot (\mathrm{Ma}_{3,rel} - 0.20) & \text{for} \quad 0.20 < \mathrm{Ma}_{3,rel} < 1.00 \quad (2.99) \\ 0 & \text{for} \quad \mathrm{Ma}_{3,rel} > 1.00 \quad (2.100) \end{cases}$$

$$K_2 = \left(\frac{\mathrm{Ma}_{2,rel}}{\mathrm{Ma}_{3,rel}} \right)^2 \quad (2.101)$$

The term Y_{shock} accounts for the relatively weak shock waves that may occur at the leading edge of the cascade due to the acceleration of the flow. This effect is particularly important close to the hub of the blades. After some algebra, the equations proposed in the Kacker-Okapuu method can be summarized as Eq. 2.102, where f_{hub} is given graphically in Fig. 2.34 and it is a function of the hub to tip radii ratio only.

$$Y_{shock} = 0.75 \cdot (f_{hub} \cdot \mathrm{Ma}_{2,rel} - 0.40)^{1.75} \cdot \left(\frac{r_h}{r_t} \right) \cdot \left(\frac{p_{02,rel} - p_2}{p_{03,rel} - p_3} \right) \quad (2.102)$$

$$\frac{r_h}{r_t} = \frac{r_m - H_2/2}{r_m + H_2/2} \quad (2.103)$$

Finally, as in the case of the Dunham-Came loss system, the correction factor used to account for shock waves at the outlet of the row, f_{Ma}, is given by Eqs. 2.87 to 2.89. Kacker and Okapuu questioned the accuracy of this correction factor but they did not suggest any better alternative.

Secondary loss

The secondary loss is computed according to:

$$Y_s = 1.2 \cdot K_s \cdot \left[0.0334 \cdot f_{AR} \cdot Z \cdot \left(\frac{\cos(\beta_3)}{\cos(\beta_2)} \right) \right] \quad (2.104)$$

The factor 1.2 is included to correct the secondary loss for blades with zero trailing edge thickness. Trailing edge losses are accounted independently.

The factor K_s accounts for compressible flow effects when the Mach number within the cascade is subsonic but larger than one. These effects tend accelerate the flow, make the end wall boundary layers thinner, and decrease the secondary losses. K_s is computed from Eq. 2.105, where K_p is given by Eq. 2.97 and K_3 is given by Eq. 2.106. K_3 is a function of the axial blade aspect ratio, H/b, only.

$$K_s = 1 - K_3 \cdot (1 - K_p) \quad (2.105)$$

$$K_3 = \left(\frac{1}{H/b} \right)^2 \quad (2.106)$$

f_{AR} accounts for the blade aspect ratio, H/c, and it is given by Eq. 2.107 or Eq. 2.108.

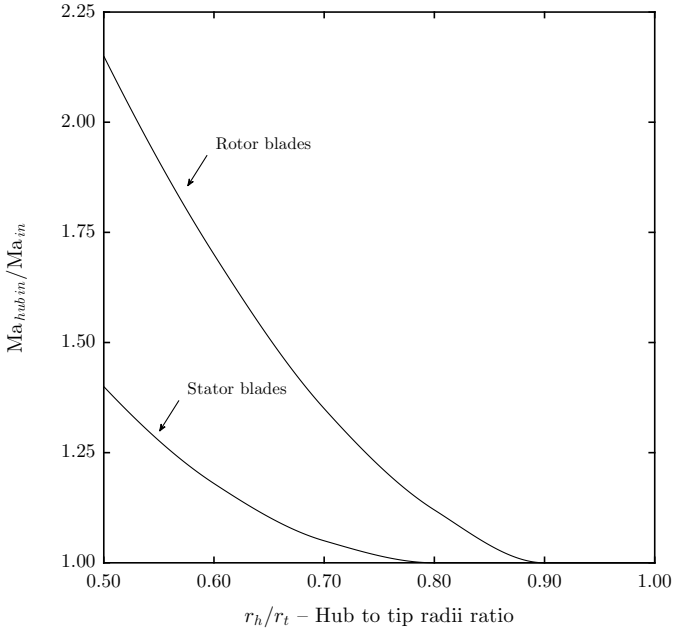

Figure 2.34: Ratio of Mach number at the hub to Mach number at the mean radius.

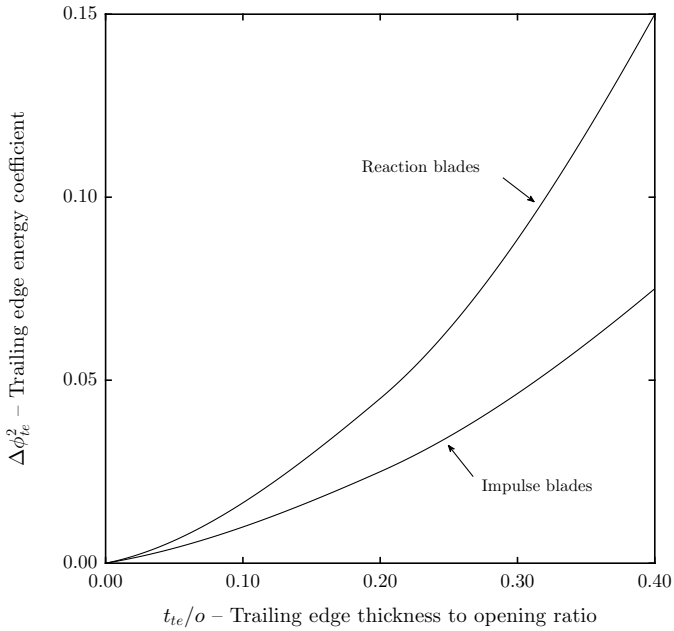

Figure 2.35: Trailing edge energy loss coefficient for impulse and reaction blades.

$$f_{AR} = \begin{cases} \dfrac{1 - 0.25 \cdot \sqrt{2 - H/c}}{H/c} & \text{for} \quad H/c < 2 \quad (2.107) \\ \dfrac{1}{H/c} & \text{for} \quad H/c > 2 \quad (2.108) \end{cases}$$

Finally, Z is given by Eqs. 2.75 to 2.77.

Tip clearance loss

The clearance loss coefficient for a stator or a rotor stage is computed according to:

$$Y_{cl} = B \cdot Z \cdot \left(\frac{c}{H}\right) \cdot \left(\frac{t_{cl}}{H}\right)^{0.78} \quad (2.109)$$

In this equation, Z is given by Eqs. 2.75 to 2.77. The Kacker-Okapuu loss system proposes $B = 0.37$ for rotor blades with shrouded tips, and $B = 0.00$ for stator blades. In addition, Kacker and Okapuu warn that using $B = 0.47$ over-predicts the loss for rotor blades with plain tips.

Trailing edge loss

The trailing edge is computed according to:

$$Y_{te} \approx \zeta = \frac{1}{\phi^2} - 1 = \frac{1}{1 - \Delta\phi^2} - 1 \quad (2.110)$$

The parameter $\Delta\phi^2$ is computed by interpolation of impulse and reaction blades as in the case of profile losses. The interpolation formula is given by Eq. 2.111.

$$\Delta\phi^2 = \Delta\phi^2_{reaction} - \left(\frac{\beta_2}{\beta_3}\right)\left|\frac{\beta_2}{\beta_3}\right| \cdot (\Delta\phi^2_{impulse} - \Delta\phi^2_{reaction}) \quad (2.111)$$

$\Delta\phi^2_{reaction}$ and $\Delta\phi^2_{impulse}$ are the energy coefficients of reaction and impulse blades and they are a function of the trailing edge thickness to opening ratio, t_{te}/o, only. The functional relation was given graphically and it is reproduced in Fig. 2.35.

Reynolds number correction factor

The Reynolds number correction factor that affects the profile loss only, see Eq. 2.94, is computed according to:

$$f_{\mathrm{Re}} = \begin{cases} \left(\dfrac{\mathrm{Re}}{2 \cdot 10^5}\right)^{-0.40} & \text{for} \quad \mathrm{Re} < 2 \cdot 10^5 \quad (2.112) \\ 1 & \text{for} \quad 2 \cdot 10^5 < \mathrm{Re} < 1 \cdot 10^6 \quad (2.113) \\ \left(\dfrac{\mathrm{Re}}{1 \cdot 10^6}\right)^{-0.20} & \text{for} \quad \mathrm{Re} > 1 \cdot 10^6 \quad (2.114) \end{cases}$$

2.11 Optimization

In this section, some fundamental concepts and nomenclature related to constrained optimization are presented. The contents of this section are relevant for both the optimization of Rankine cycles and turbomachinery. Every optimization problem comprises three essential steps: (1) choosing an objective function of interest, (2) selection of the independent variables, and (3) definition of constraints that limit the range of search. A general optimization problem can be set out as:

$$\min f(x) = \begin{cases} lb \leq x \leq ub & (2.115) \\ c_{ineq}(x) \leq 0 & (2.116) \\ c_{eq}(x) = 0 & (2.117) \end{cases}$$

Where f is the objective function, x is the vector of degrees of freedom, lb and ub are the lower and upper bounds for the degrees of freedom, $c_{ineq}(x)$ is the vector of inequality constraints, and $c_{eq}(x)$ is the vector of equality constraints. Optimization algorithms, such as the ones available in the *Optimization Toolboox* and *Global Optimization Toolboox* of MATLAB, can solve this problem once all the terms are defined.

2.11.1 Objective function

The objective function can be any indicator of interest that has to be minized or maximized. Most optimization algorithms are designed to minimize an objective function but they can be maximize an objective function introducing a minus sign.

$$\text{Minimize} \implies f \tag{2.118}$$

$$\text{Maximize} \implies -f \tag{2.119}$$

The objective functions used in this work to optimize Rankine cycles and turbomachinery are discussed in Section 3.3.1 and Section 3.4.1, respectively.

2.11.2 Degrees of freedom

The degrees of freedom are the parameters of the system that may be varied independently, such as the temperature at the inlet of the turbine or the stage design parameters. The size of the search space and the computational cost of the problem increase as the number of degrees of freedom increases.

The choice of the degrees of freedom is not unique and some sets of degrees of freedom might be more computationally efficient than others. The degrees of freedom used in this work to optimize Rankine cycles and turbomachinery are discussed in Section 3.3.3 and Section 3.4.3, respectively.

2.11.3 Constraints

There are two types of constraints, equality constraints, c_{eq} and inequality constraints, c_{ineq}. Equality constraints can be regarded as equations that the optimal solution has to satisfy in order to be feasible. Conversely, inequality constraints impose some limits that cannot be violated such as the minimum temperature difference in a heat exchanger or the maximum flaring angle allowed in an axial turbine design. An inequality constraint is said to be active if the constrained variable is in the limit and the equality sign holds. Otherwise, the constraint is said to be inactive. By definition, equality constraints are always active.

In addition to inequality constraints, in most algorithms, it is possible to define lower and upper bounds for the degrees of freedom. Bounds for the degrees of freedom are computationally easier to handle than inequality constraints. Using the right set of degrees of freedom may allow to convert optimization constraints into bounds, increasing the chances of finding an optimal solution and reducing the computational cost of the problem.

2.11.4 Optimization algorithm

Optimization algorithms can be classified in two families, gradient-based algorithms and direct-search methods.

If the computational model[22] is smooth, optimization algorithms that use the gradient of the objective function to find the optimum solution can be used. These optimization algorithms converge relatively fast but they are sensitive to the initial guess for the degrees of freedom and they may find local optima solutions instead of finding the global optimum. However, these methods are not well suited for non-smooth problems.

If the computational model is not smooth, direct-search methods can be used to find the optimum solution. These methods methods do not rely on the gradient of the objective function and they are capable of quickly finding promising regions of the search space. However, the rate of convergence can be orders of magnitude lower than gradient-based methods. The risk of finding local optima solution is lower for direct search methods.

In this work, gradient-based algorithms were preferred because the computational models were smooth and a fast optimization tool was desired. The risk of finding local optima solutions was minimized repeating the simulations from different starting values for the degrees of freedom.

[22] A computational model will be smooth if the objective function and all constraints are smooth.

Chapter 3

Case study and methodology

3.1 The case study

The case study for this work is a waste heat recovery application where the heat source is a 10 kg/s hot stream of air at 250 °C. The minimum temperature of the heat source is limited by a hypothetical downstream gas cleaning facility to 100 °C. The heat sink available is liquid water at ambient temperature and pressure. The parameters of the case study are summarized in Table 3.1.

Both simple and recuperated Rankine cycles are proposed to convert the thermal energy from the waste heat source into power. Axial turbines of any number of stages are adopted to extract the energy from the working fluid and convert it into work. 80 substances contained in the REFPROP library are considered as possible working fluid candidates.

The objective of this chapter is to describe the methodology for the fluid screening and optimization of Rankine cycles and axial turbines that was developed in this work. These methods will be applied to the case study described in this chapter and the results will be presented and discussed in Chapter 4.

Table 3.1: Specifications of the case study.

Variable name	Symbol	Value
Ambient pressure	p_o	101.325 kPa
Ambient temperature	T_o	10 ^{o}C
Heat sink inlet temperature	T_{c1}	10 ^{o}C
Heat source inlet temperature	T_{h1}	250 ^{o}C
Heat source minimum outlet temperature	$T_{h2,min}$	100 ^{o}C
Heat source mass flow rate	$\dot{m}_h$	10 kg/s
Heat sink fluid	Water	
Heat source fluid	Air	composition
	Nitrogen	78.12%
	Oxygen	20.96%
	Argon	0.92%

3.2 Fluid screening methodology

There is a large amount of substances that could be used as working fluids for Rankine cycles. Several criteria, including thermodynamic match with the heat source and sink, environmental concerns, chemical stability, or the cost and availability of the fluid can be used to reduce the number of fluid candidates.

In this work, 80 substances contained in the REFPROP library were considered and the following screening criteria were used to filter out inappropriate working fluids:

1. The ozone depletion potential of the working fluid has to be zero (ODP with respect to R11, as defined in the Montreal Protocol).
2. The global warming potential of the working fluid has to be lower than 150 (GWP over 100 years with respect to CO_2). This value is also adopted by Lecompte et al. (2015a) and it follows from the European Union regulations that aim to ban refrigerants with high global warming potentials.
3. The critical temperature has to be higher than the ambient temperature to make condensation possible.
4. The melting temperature at ambient pressure has to be lower than the ambient temperature to avoid fluid freezing during shutdown time.
5. The saturation pressure at ambient temperature has to be higher than 1 kPa to limit the vacuum in the condenser.
6. The minimum and maximum temperature limits of the equation of state have to be wider than temperature span of the thermodynamic cycle (ambient temperature of 10 °C and heat source temperature of 250 °C). This ensures chemical stability because the upper temperature limit of the equations of state of REFPROP is near the point of decomposition of the working fluid.

Other screening criteria including safety, chemical stability, corrosivity or cost were not considered in this work. A small database of 80 working fluids was prepared in Microsoft Excel to perform the fluid screening. The information contained in this database is included in Appendix A. The results of the fluid screening are presented in Section 4.1.

3.3 Rankine cycle optimization methodology

The Rankine cycle optimization methodology used in this work is described in this section. Both simple and recuperated layouts were considered and the steady-state cycle optimization algorithms for both cases were implemented in MATLAB. The methods described in this section were applied to the case study presented in Section 3.1 and the results of the optimization are presented in Section 4.2.

3.3.1 Objective function

The second law efficiency of the plant was selected as the objective function:

$$\text{Maximize} \implies f = \eta_{II\,plant} \tag{3.1}$$

Since the optimization algorithms of MATLAB are designed to minimize objective functions, the sign of the objective function is reversed:

$$\text{Minimize} \implies f = -\eta_{II\,plant} \tag{3.2}$$

The second law efficiency of the plant is defined as the ratio of the net power output of the cycle, $\dot{W}_{net}$[1], to the exergy flow at the inlet of the heat source, $\dot{E}_{h1}$[2]:

$$\eta_{II\,plant} = \frac{\dot{W}_{net}}{\dot{E}_{h1}} \tag{3.3}$$

Other thermodynamic objective functions could also be used, such as the first law efficiency of the plant. This variable is defined as the ratio of the net power output, $\dot{W}_{net}$, to the maximum heat flow rate that can be extracted from the heat source, $\dot{Q}_{max}$[3]:

$$\eta_{I\,plant} = \frac{\dot{W}_{net}}{\dot{Q}_{max}} \tag{3.4}$$

Both objective functions give the same thermodynamic optimum because they maximize the power output obtained from a fixed heat source. In this work, the second law efficiency was preferred because it gives insight about how much potential for improvement is left. Values of the first law efficiency were also reported because they are easier to interpret for readers not familiarized with exergy analysis.

In this work, the efficiency of the cycle was not used as objective function because the optimization algorithm would find a solution in which part of the energy from the hot source is not recovered. This can be explained as follows: if the heat source is not fully

[1] $\dot{W}_{net}$ is defined as the expansion power minus the power consumed by the pump.

[2] $\dot{E}_{in}$ can be interpreted as the maximum (reversible) work that would be obtained if the heat source was brought to ambient temperature and pressure.

[3] $\dot{Q}_{max}$ is the hypothetical heat flow rate that would be extracted from the heat source if the temperature was brought to ambient temperature and pressure.

recovered, the average temperature of heat transfer to the cycle would be higher and the exergy destruction for a given average temperature difference would be lower, increasing the cycle efficiency. Despite the increase in cycle efficiency, the overall plant efficiency (and the actual power output) would not be optimal.

The relation between plant second law efficiency, cycle second law efficiency, and exergy recovery efficiency is given by Eqs. 3.5 to 3.7.

$$\eta_{II\,cycle} = \frac{\dot{W}_{net}}{\dot{E}_{h1} - \dot{E}_{h2}} \tag{3.5}$$

$$\eta_{II\,recovery} = \frac{\dot{E}_{h1} - \dot{E}_{h2}}{\dot{E}_{h1}} \tag{3.6}$$

$$\eta_{II\,plant} = \eta_{II\,cycle} \cdot \eta_{II\,recovery} \tag{3.7}$$

In an similar manner, the relation between plant first law efficiency, cycle first law efficiency, and energy recovery efficiency is given by Eqs 3.8 to 3.10.

$$\eta_{I\,cycle} = \frac{\dot{W}_{net}}{\dot{Q}_{evap}} \tag{3.8}$$

$$\eta_{I\,recovery} = \frac{\dot{Q}_{evap}}{\dot{Q}_{max}} \tag{3.9}$$

$$\eta_{I\,plant} = \eta_{I\,cycle} \cdot \eta_{I\,recovery} \tag{3.10}$$

Table 3.2: Fixed parameters for cycle optimization.

Variable name	Symbol	Value
Temperature differences		
Min. temperature difference in the primary heat exchanger	$\Delta T'_{evap}$	10 ^{o}C
Min. temperature difference in the condenser	$\Delta T'_{cond}$	10 ^{o}C
Min. temperature difference in the recuperator	$\Delta T'_{recup}$	10 ^{o}C
Pressure drops		
Pressure drop in the primary heat exchanger (heat source)	$\Delta p_{h,evap}$	1%
Pressure drop in the primary heat exchanger (working fluid)	$\Delta p_{f,evap}$	1%
Pressure drop in the condenser (working fluid)	$\Delta p_{f,cond}$	1%
Pressure drop in the condenser (heat sink)	$\Delta p_{r,cond}$	1%
Pressure drop in the recuperator (hot side)	$\Delta p_{f,recup}$	1%
Pressure drop in the recuperator (cold side)	$\Delta p_{f,recup}$	1%
Turbomachinery efficiency		
Pump polytropic efficiency	η_{pump}	70%
Expander polytropic efficiency	η_{exp}	75%

3.3.2 Fixed parameters

In this work, the temperature differences and pressure drops in heat exchangers are considered as fixed parameters. The polytropic efficiency of turbine and pump are also considered as fixed parameters. The fixed input parameters for the cycle optimization are summarized in Table 3.2. In addition, the characteristics of the heat source and sink, see Table 3.1, can also be regarded as fixed parameters. The values used for the simulation of simple and recuperated cycles are identical except for the recuperator specifications.

3.3.3 Degrees of freedom

The choice of degrees of freedom is not unique and some sets of degrees of freedom might be more computationally efficient than others. In this work, the choice of degrees of freedom for the cycle allows for the computation of all the thermodynamic states in a sequential manner without solving any system of algebraic equations. This leads to fast function evaluations and computationally inexpensive optimizations.

The simple cycle has 6 degrees of freedom and the recuperated cycle has 7. The degrees of freedom are summarized in Table 3.3 and they are defined as dimensionless, normalized parameters related to the cycle variables of the following list:

1. Outlet temperature of the heat source.
2. Temperature increase of the cooling fluid in the condenser.
3. Pressure at the inlet of the expander.
4. Pressure at the outlet of the expander.
5. Enthalpy at the inlet of the expander.
6. Enthalpy at the inlet of the evaporator.
7. Enthalpy at the outlet of the condenser (just for the recuperated cycle).

Choosing appropriate values for the reference minimum and maximum properties, the degrees of freedom take values between zero and one. Scaling the problem in this way reduces the numerical rounding error during the optimization and makes it easier to give a reasonable initial guess for the degrees of freedom.

The maximum and minimum reference parameters should cover all all possible states occurring in Rankine cycles and, ideally, they should not constraint the cycle optimization. The maximum and minimum reference parameters used in this work are summarized in Table 3.4. The minimum and maximum temperature increases of the cooling fluid in the condenser were arbitrarily set to 5 °C and 10 °C, respectively. The minimum pressure was set as the saturation pressure at ambient temperature and the maximum pressure as three times the critical pressure. The minimum enthalpy was set as the saturated liquid enthalpy at ambient temperature and the maximum enthalpy as the ideal gas (zero pressure) enthalpy at the inlet temperature of the heat source.

Table 3.3: Degrees of freedom for simple and recuperated cycles.

Simple cycle		**Recuperated cycle**	
$x_1 = \frac{T_{h_2} - T_{h_2,min}}{T_{h_1} - T_{h_2,min}}$	(3.11)	$x_1 = \frac{T_{h_2} - T_{h_2,min}}{T_{h_1} - T_{h_2,min}}$	(3.12)
$x_2 = \frac{\Delta T_c - \Delta T_{c,min}}{\Delta T_{c,max} - \Delta T_{c,min}}$	(3.13)	$x_2 = \frac{\Delta T_c - \Delta T_{c,min}}{\Delta T_{c,max} - \Delta T_{c,min}}$	(3.14)
$x_3 = \frac{p_{f_3} - p_{min}}{p_{max} - p_{min}}$	(3.15)	$x_3 = \frac{p_{f_4} - p_{min}}{p_{max} - p_{min}}$	(3.16)
$x_4 = \frac{p_{f_4} - p_{min}}{p_{max} - p_{min}}$	(3.17)	$x_4 = \frac{p_{f_5} - p_{min}}{p_{max} - p_{min}}$	(3.18)
$x_5 = \frac{h_{f_3} - h_{min}}{h_{max} - h_{min}}$	(3.19)	$x_5 = \frac{h_{f_4} - h_{min}}{h_{max} - h_{min}}$	(3.20)
$x_6 = \frac{h_{f_2} - h_{min}}{h_{max} - h_{min}}$	(3.21)	$x_6 = \frac{h_{f_3} - h_{min}}{h_{max} - h_{min}}$	(3.22)
		$x_7 = \frac{h_{f_1} - h_{min}}{h_{max} - h_{min}}$	(3.23)

Table 3.4: Minimum and maximum reference values for the cycle degrees of freedom.

Minimum reference values	Maximum reference values
$\Delta T_{c,min} = 5\,°\mathrm{C}$	$\Delta T_{c,max} = 10\,°\mathrm{C}$
$p_{min} = p_{sat}(T_o)$	$p_{max} = 3 \cdot p_{crit}$
$h_{min} = h_{liq}(T_o)$	$h_{max} = h(T_{h1}, p \to 0)$

3.3.4 Optimization constraints

As a result of the scaling presented in the previous section the lower bound is zero and the upper bound is one for all the degrees of freedom:

$$lb_i = 0 \leq x_i \leq 1 = ub_i \quad \text{for} \quad i = 1, 2, 3, 4, 5, 6, 7 \tag{3.24}$$

No equality constraints ($c_{eq} = 0$) were used for the optimization of thermodynamic cycles. Several inequality constraints ($c_{ineq} \leq 0$) were used in this work. Inequality constraints are essentially the same for the simple and the recuperated cycle and they are described in the following list:

1. The working fluid has to be subcooled at the inlet of the pump (avoid cavitation).
2. If the pressure is subcritical, the working fluid has to be subcooled at the inlet of the evaporator (avoid phase change in the recuperator).
3. If the pressure is subcritical, the working fluid has to be saturated or superheated at the outlet of the evaporator (avoid two phase expansion).
4. The working fluid has to be saturated or superheated at the outlet of the expander (avoid two phase expansion).
5. The pinch point in the evaporator has to be higher than the minimum temperature difference specified (avoid temperature crossing).
6. The pinch point in the condenser has to be higher than the minimum temperature difference specified (avoid temperature crossing).
7. The pinch point in the recuperator has to be higher than the minimum temperature difference specified (avoid temperature crossing).

These constraints are expressed mathematically in Table 3.5. Some of the constraints have a negative sign to accommodate inequalities of the type $c_{ineq}(x) \geq 0$.

The writer found that the equations of state of REFPROP might fail to converge for thermodynamic states very close to the critical point. For this reason the constraint given by Eq 3.25 was also considered. This is a constraint of OR type and it is not directly supported in MATLAB. However it can be accomodated with a non-linear constraint using the minimum of both constraints, as expressed by Eq 3.26.

$$\frac{p_{f_2}}{p_{crit}} \leq 0.95 \quad \text{OR} \quad \frac{p_{f_2}}{p_{crit}} \geq 1.05 \tag{3.25}$$

$$c_{crit} = \min\left(\frac{p_{f_2}}{p_{crit}} - 0.95, -\frac{p_{f_2}}{p_{crit}} + 1.05\right) \tag{3.26}$$

Table 3.5: Inequality constraints for the simple and recuperated cycles

Simple cycle		**Recuperated cycle**	
$c_1 = \frac{h_{f_1} - h_{liq}(p_{f_1})}{h_{max} - h_{min}}$	(3.27)	$c_1 = \frac{h_{f_1} - h_{liq}(p_{f_1})}{h_{max} - h_{min}}$	(3.28)
$c_2 = \frac{h_{f_2} - h_{liq}(p_{f_2})}{h_{max} - h_{min}}$	(3.29)	$c_2 = \frac{h_{f_3} - h_{liq}(p_{f_3})}{h_{max} - h_{min}}$	(3.30)
$c_3 = -\frac{h_{f_3} - h_{vap}(p_{f_3})}{h_{max} - h_{min}}$	(3.31)	$c_3 = -\frac{h_{f_4} - h_{vap}(p_{f_4})}{h_{max} - h_{min}}$	(3.32)
$c_4 = -\frac{h_{f_4} - h_{vap}(p_{f_4})}{h_{max} - h_{min}}$	(3.33)	$c_4 = -\frac{h_{f_5} - h_{vap}(p_{f_5})}{h_{max} - h_{min}}$	(3.34)
$c_5 = -\frac{\Delta T_{evap} - \Delta T'_{evap}}{\Delta T'_{evap}}$	(3.35)	$c_5 = -\frac{\Delta T_{evap} - \Delta T'_{evap}}{\Delta T'_{evap}}$	(3.36)
$c_6 = -\frac{\Delta T_{cond} - \Delta T'_{cond}}{\Delta T'_{cond}}$	(3.37)	$c_6 = -\frac{\Delta T_{cond} - \Delta T'_{cond}}{\Delta T'_{cond}}$	(3.38)
		$c_7 = -\frac{\Delta T_{recup} - \Delta T'_{recup}}{\Delta T'_{recup}}$	(3.39)

3.3.5 Optimization algorithm

The MATLAB function *fmincon* was used to perform the optimization. This function uses gradient-based optimization algorithms to find the minimum value of the objective function. There are several optimization algorithms available, including *interior-point*, *active-set*, and *sqp* algorithms. These three algorithms were tested and they were able to converge to the same optimal cycle configurations. The *active-set* algorithm was chosen because the computational time was slightly lower.

The flow-sheet of the cycle optimization algorithm is shown in figure Fig. 3.2 and it will be described in the remainder of this section. The algorithm is essentially the same for the simple and recuperated cycles. When the main MATLAB script is executed, the fixed parameters, degrees of freedom of the cycle, upper and lower limits for the degrees of freedom, and the parameters for the constraints are defined and supplied to the cycle simulation function.

Within the cycle simulation function, the degrees of freedom as defined in Table 3.3 are converted to the usual cycle variables such as enthalpy and pressure. All the thermodynamic states of the cycle are found using the REFPROP library using mostly enthalpy-pressure function calls to the equations of state. All the states are determined in a sequential manner without solving any system of algebraic equations. The pressure, temperature, density, enthalpy, and entropy are determined at each cycle point. In addition, the specific exergy of each state is computed according to Eq 3.40 and the exergy flow at as Eq 3.41.

$$e = (h - h_o) - T_o \cdot (s - s_o) \tag{3.40}$$

$$\dot{E} = \dot{m} \cdot e \tag{3.41}$$

The state at the outlet of the expander is determined using the polytropic efficiency and integrating the ODE defined by Eq 3.42 from the pressure at the inlet to the pressure at the outlet. The enthalpy at the inlet is used as initial condition. In this work, the MATLAB function ODE45 was used for the numerical integration. This is an automatic-stepsize-control solver that combines fourth and fifth order Runge-Kutta methods. The state at the outlet of the pump is determined in a similar manner solving the ODE defined by Eq 3.43.

$$\frac{\mathrm{d}h}{\mathrm{d}p} = \rho \cdot \eta_{exp} \tag{3.42}$$

$$\frac{\mathrm{d}h}{\mathrm{d}p} = \rho \cdot \frac{1}{\eta_{pump}} \tag{3.43}$$

The minimum temperature differences in heat exchangers is computed using the the enthalpy and pressure at the inlet and outlet of the hot and cold streams. Temperature crosses can occur, but such solutions will be rejected because they violate the optimization constraints. The pinch points are computed differently for subcritical and supercritical heat exchangers:

1. If both streams are subcritical the heat exchanger computes the temperature difference at the inlet, at the outlet, and at possible phase changes.

2. If at least one stream is supercritical the heat exchanger is discretized in 25 nodes and the temperature difference is computed at each node. The heat exchangers were discretized in 25 nodes because it was found to be a good compromise between accuracy and computational time.

Subcritical heat exchangers require thermodynamic property evaluations at 2-4 nodes instead of 25 and they are less computationally expensive. For this reason, the time required for the optimization of transcritical cycles is higher than that required for subcritical cycles.

The mass flow rate of working fluid and cooling fluid are determined using the energy balance in the primary heat exchanger and in the condenser, respectively. For the case of recuperated cycles, the energy balance in the recuperator is used to compute the enthalpy at the inlet of the condenser.

Once all cycle points are found, the constraints are evaluated and the objective function (second law efficiency) is computed. At this point, any other variable of interest can be computed. After this, the optimization algorithm in MATLAB checks if the maximum tolerance for the constraints is violated and, if this is the case, the degrees of freedom are modified and the cycle simulation function is called again.

If the constraints are not violated, the MATLAB algorithm checks if the solution is optimal. The solution will be considered as optimal if the norm of the change in the vector of degrees of freedom (step size), the value of the change in the objective function, and the first order optimality measure (as implemented in MATLAB) are less than the tolerances prescribed by the user. If the tolerances are violated the degrees of freedom are modified and the cycle simulation function is called again. If the tolerances are not violated the optimization is stopped and the optimal cycle is plotted (T–s, T–h, and T–$\dot{Q}$ diagrams) and saved as MATLAB (.mat) and Excel (.xmsl) files for further processing of the solution.

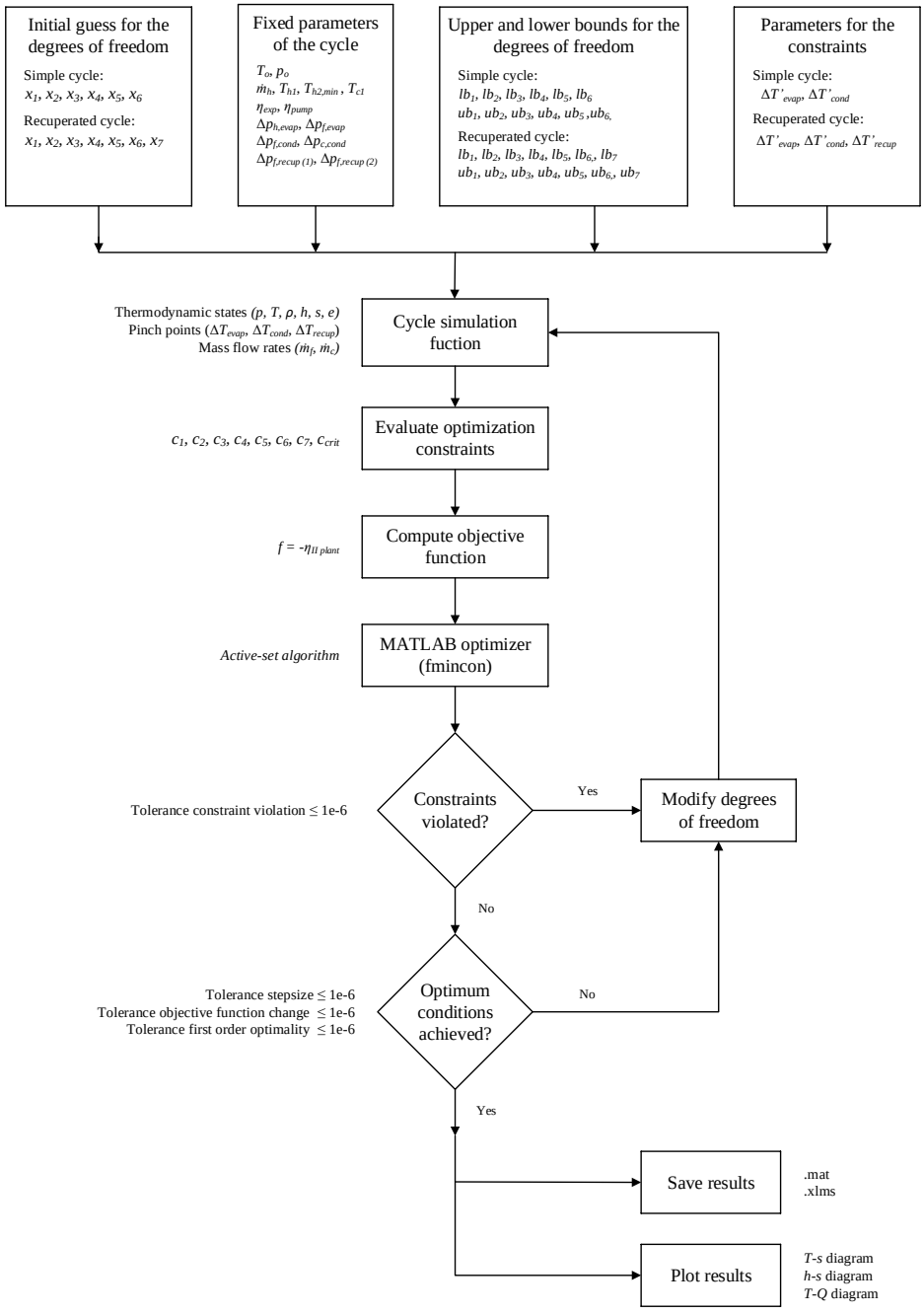

Figure 3.1: Cycle optimization algorithm.

3.4 Axial turbine optimization methodology

The axial turbine optimization methodology used in this work is described in this section. Axial turbines of any number of stages were considered and the algebraic mean-line optimization algorithm was implemented in MATLAB. The methods described in this section were applied to the case study presented in Section 3.1 and the results of the optimization are presented in Section 4.3.

3.4.1 Objective function

The turbine total-to-static efficiency was selected as the objective function:

$$\text{Maximize} \implies f = \eta_{ts} \tag{3.44}$$

Since the optimization algorithms of MATLAB are designed to minimize objective functions, the sign of the objective function is reversed:

$$\text{Minimize} \implies f = -\eta_{ts} \tag{3.45}$$

The total-to-static efficiency was preferred over the total-to-total efficiency because the former accounts for the kinetic energy lost at the outlet of the turbine. This is relevant because the use of a diffuser to recover the kinetic energy at the outlet of the turbine was not considered in this work.

3.4.2 Fixed parameters

In this work, the working fluid, mass flow rate, stagnation pressure and enthalpy at the inlet, and stagnation pressure at the outlet are considered as fixed parameters. These parameters are obtained from the optimization of the Rankine cycle.

The number of stages of the turbine could also be regarded as a fixed parameter because it is not varied during the optimization. The number of stages cannot be considered as an ordinary degree of freedom because it can only take integer values. The effect of this variable can be investigated independently of the optimization.

3.4.3 Degrees of freedom

In this work, the choice of degrees of freedom for the turbine allows for the computation of the velocity triangles, thermodynamic states, turbine geometry, and losses in a sequential manner without solving any system of algebraic equations. This leads to fast function evaluations and computationally inexpensive optimizations.

The axial turbine has 4 degrees of freedom plus another 6 degrees of freedom for each stage. In other words, the optimization algorithm uses $4 + 6\,n$ degrees of freedom, where n is the number of stages. All degrees of freedom are defined in a dimensionless way and they are included in the following list:

1. Flow coefficient.
2. Work coefficient.
3. Reaction ratio.
4. Specific speed of the turbine.
5. Pitch to chord ratio of the stator cascade (one for each stage).
6. Pitch to chord ratio of the rotor cascade (one for each stage).
7. Blade aspect ratio of the stator cascade (one for each stage).
8. Blade aspect ratio of the rotor cascade (one for each stage).
9. Ratio of stator-outlet to turbine-inlet entropy (one for each stage).
10. Ratio of rotor-outlet to turbine-inlet entropy (one for each stage).

The order of magnitude of all degrees of freedom is between 10^{-1} and 10^{1}. For this reason, it is not necessary to scale the problem to reduce numerical rounding errors during the optimization. The degrees of freedom are expressed in mathematical form in Table 3.6

Table 3.6: Degrees of freedom for axial turbines.

Global degrees of freedom		**Degrees of freedom for each stage**	
$x_1 = \phi$	(3.46)	$x_5 = (s/c)_S$	(3.47)
$x_2 = \psi$	(3.48)	$x_6 = (s/c)_R$	(3.49)
$x_3 = R$	(3.50)	$x_7 = (H/c)_S$	(3.51)
$x_4 = \omega_s$	(3.52)	$x_8 = (H/c)_R$	(3.53)
		$x_9 = s_2/s_{in}$	(3.54)
		$x_{10} = s_3/s_{in}$	(3.55)

3.4.4 Optimization constraints

The lower and upper bounds for the degrees of freedom are summarized in the next list:

$$lb_1 = 0.10 \leq \phi \leq 1.50 = ub_1 \tag{3.56}$$

$$lb_2 = 0.10 \leq \psi \leq 5.00 = ub_2 \tag{3.57}$$

$$lb_3 = 0.00 \leq R \leq 1.00 = ub_3 \tag{3.58}$$

$$lb_4 = 0.10 \leq \omega_s \leq 5.00 = ub_4 \tag{3.59}$$

$$lb_5 = 0.40 \leq (s/c)_S \leq 1.20 = ub_5 \tag{3.60}$$

$$lb_6 = 0.40 \leq (s/c)_R \leq 1.20 = ub_6 \tag{3.61}$$

$$lb_7 = 0.20 \leq (H/c)_S \leq 5.00 = ub_7 \tag{3.62}$$

$$lb_8 = 0.20 \leq (H/c)_R \leq 5.00 = ub_8 \tag{3.63}$$

$$lb_9 = 1.00 \leq s_2/s_{in} \leq s_{out}/s_{in} = ub_9 \tag{3.64}$$

$$lb_{10} = 1.00 \leq s_2/s_{in} \leq s_{out}/s_{in} = ub_{10} \tag{3.65}$$

Where s_{out} is the entropy at the outlet of the turbine if the isentropic efficiency was 50%.

The lower and upper bounds used in this work were selected based on some of the general recommendations given in Saravanamuttoo et al. (2009) and Dixon and Hall (2013). As there is no particular technical limitation for these degrees of freedom, the range within the lower and upper bounds should be wide enough in order to not constrain the optimization.

In general, the entropy increase given by the degrees of freedom, s_2 and s_3, will not match the entropy increase predicted by the loss correlations, $\tilde{s}_2$ and $\tilde{s}_3$. This difficulty is handled imposing equality constraints (c_{eq}) for the entropy computed from the degrees of freedom and loss correlations.

$$c_{eq,1} = s_2 - \tilde{s}_2 \tag{3.66}$$

$$c_{eq,2} = s_3 - \tilde{s}_3 \tag{3.67}$$

Several inequality constraints ($c_{ineq} \leq 0$) were used in this work and they are included in the following list:

1. Maximum Mach number (absolute or relative) within the turbine.
2. Minimum hub to tip ratio of any cascade.
3. Maximum hub to tip ratio of any cascade.
4. Maximum flaring angle of any cascade.
5. Minimum angle at the outlet of any stator (imposed by loss correlation).
6. Maximum angle at the outlet of any stator (imposed by loss correlation).
7. Minimum angle at the outlet of any rotor (imposed by loss correlation).
8. Maximum angle at the outlet of any rotor (imposed by loss correlation).

These constraints are expressed mathematically in Eqs. 3.68 to 3.75. Some of the constraints have a negative sign to accommodate inequalities of the type $c_{ineq}(x) \geq 0$.

$$c_1 = \mathrm{Ma} - \mathrm{Ma}_{max} \tag{3.68}$$

$$c_2 = -[(r_h/r_t) - (r_h/r_t)_{min}] \tag{3.69}$$

$$c_3 = (r_h/r_t) - (r_h/r_t)_{max} \tag{3.70}$$

$$c_4 = \delta_{fl} - \delta_{fl,max} \tag{3.71}$$

$$c_5 = -(\alpha_2 - \alpha_{2,min}) \tag{3.72}$$

$$c_6 = \alpha_2 - \alpha_{2,max} \tag{3.73}$$

$$c_5 = -(\beta_3 - \beta_{3,min}) \tag{3.74}$$

$$c_6 = \beta_3 - \beta_{3,max} \tag{3.75}$$

The three first constraints were not used for optimization results presented in Chapter 4, but they are included here to show the capabilities of the methodology. In order to skip these constraints the following values were used in this work: $\mathrm{Ma}_{max} = 10$, $(r_h/r_t)_{min} = 0$, and $(r_h/r_t)_{max} = 1$.

The maximum flaring angle allowed in this work was $20°$ as suggested by Ainley and Mathieson (1951b) and endorsed by Saravanamuttoo et al. (2009). The constraints for the angles were selected based on the limits of the Ainley-Mathieson correlations, see Fig. 2.29 and 2.30. In particular, $\alpha_{2,min} = 40°$, $\alpha_{2,max} = 70°$, $\beta_{3,min} = -70°$, and $\beta_{3,max} = -40°$.

3.4.5 Optimization algorithm

The MATLAB function *fmincon* was used to perform the optimization. This function uses gradient-based optimization algorithms to find the minimum value of the objective function. There are several optimization algorithms available, including *interior-point*, *active-set*, and *sqp* algorithms. These three algorithms were tested and they were able to converge to the same optimal turbine design. The *sqp* algorithm was chosen because the computational time was slightly lower.

The flow-sheet of the turbine optimization algorithm is shown in figure Fig. **??** and it will be described in the remainder of this section. When the main MATLAB script is executed, the fixed parameters, degrees of freedom of the turbine, upper and lower limits for the degrees of freedom, and the parameters for the constraints are defined and supplied to the turbine simulation function.

Within the turbine simulation function, the degrees of freedom of Table 3.6 are used to compute the velocity triangles, thermodynamic states, turbine geometry, and losses in a sequential manner without solving any system of algebraic equations. The procedure for the computation of one stage is described in the following paragraphs. The rest of the stages are computed in an identical manner, using the variables at the outlet of the previous stage as the variables at the inlet of the current stage.

In order to compute the velocity triangles, first, the enthalpy drop, number of stages, and work coefficient are used to determined the blade speed according to Eq. 3.76.

$$u = \sqrt{\frac{h_{0,in} - h_{0,out}}{n \cdot \psi}} \tag{3.76}$$

In addition, the angular speed and the mean radius can be calculated in an straightforward manner

$$\omega = \omega_s \cdot \frac{(h_{0,in} - h_{0,out,s})^{3/4}}{(\dot{m}_{out}/\rho_{out,s})^{1/2}} \tag{3.77}$$

$$r_m = u/\omega \tag{3.78}$$

Then, the definition of flow coefficient, Eq. 3.79, is used to compute the axial velocity.

$$v_x = \phi \cdot u \tag{3.79}$$

After this, the repeating stage relations, Eqs 3.80 to 3.83, are used to compute the flow angles. The computation of all absolute and relative velocities follows easily.

$$\tan(\alpha_2) = \frac{1}{\phi}\left(1 - R + \psi/2\right) \tag{3.80}$$

$$\tan(\alpha_3) = \frac{1}{\phi}\left(1 - R - \psi/2\right) \tag{3.81}$$

$$\tan(\beta_2) = -\frac{1}{\phi}\left(R - \psi/2\right) \tag{3.82}$$

$$\tan(\beta_3) = -\frac{1}{\phi}\left(R + \psi/2\right) \tag{3.83}$$

Once the velocity triangles are determined, the thermodynamic properties are computed. The enthalpy at the outlet of the stator is determined using the principle of conservation of energy, see Eq. 3.84. In a similar manner, the enthalpy at the outlet of the rotor is determined using the principle of conservation of rothalpy (relative stagnation enthalpy for an axial turbine), see Eq. 3.85.

$$h_2 = h_1 + \frac{v_1^2}{2} - \frac{v_2^2}{2} \tag{3.84}$$

$$h_3 = h_2 + \frac{w_2^2}{2} - \frac{w_3^2}{2} \tag{3.85}$$

The entropy (degree of freedom) and enthalpy determine the thermodynamic states at the outlet of the stator and rotor. However, enthalpy-entropy function calls to the equations of state employed by the REFPROP library might fail to converge. In order to overcome this challenge, a numerical trick was used to increase the robustness of the enthalpy-entropy function calls, at the cost of increased computational time.

A value for the pressure (unknown at this point) is guessed, $\widetilde{p}$, and density is computed using pressure-enthalpy, ρ_{ph}, and pressure-entropy, ρ_{ps}, function calls:

$$\rho_{ph} = \rho(\widetilde{p}, h) \tag{3.86}$$

$$\rho_{ps} = \rho(\widetilde{p}, s) \tag{3.87}$$

In general, the value of density obtained by both function calls will not match and new values of pressure are supplied until the computation of density converges. This is expressed mathematically as:

$$p = \widetilde{p} \quad \text{if} \quad \rho_{ph} - \rho_{ps} = 0 \tag{3.88}$$

Once the correct value of pressure is found, the rest of the thermodynamic properties are found using pressure-enthalpy function calls to the equations of state. This includes temperature, compressibility factor, and speed of sound.

$$T = T(p, h) \tag{3.89}$$

$$Z = Z(p, h) \tag{3.90}$$

$$a = a(p, h) \tag{3.91}$$

At this point, the absolute and relative mach numbers can be computed.

$$\mathrm{Ma}_1 = v_1/a_1 \tag{3.92}$$

$$\mathrm{Ma}_2 = v_2/a_2 \tag{3.93}$$

$$\mathrm{Ma}_{rel,2} = w_2/a_2 \tag{3.94}$$

$$\mathrm{Ma}_{rel,3} = w_3/a_1 \tag{3.95}$$

After all thermodynamic states have been found, the geometry of the turbine can be determined. The first step is to use the principle of conservation of mass to compute the blade height at the inlet and outlet of rotor and stator.

$$H_1 = \frac{1}{2\pi} \cdot \frac{\dot{m}}{r_m \, v_x \, \rho_1} \tag{3.96}$$

$$H_2 = \frac{1}{2\pi} \cdot \frac{\dot{m}}{r_m \, v_x \, \rho_2} \tag{3.97}$$

$$H_3 = \frac{1}{2\pi} \cdot \frac{\dot{m}}{r_m \, v_x \, \rho_3} \tag{3.98}$$

The mean blade height is then computed as the arithmetic mean between the inlet and the outlet of the cascade:

$$H_S = \frac{H_1 + H_2}{2} \tag{3.99}$$

$$H_R = \frac{H_2 + H_3}{2} \tag{3.100}$$

The chord of stator and rotor can be computed from the degrees of freedom and the mean blade heights:

$$c_S = \frac{H_S}{(H/c)_S} \tag{3.101}$$

$$c_R = \frac{H_R}{(H/c)_R} \tag{3.102}$$

The computation of the blade spacing follows directly from the blade chords:

$$s_S = c_S \cdot (s/c)_S \tag{3.103}$$

$$s_R = c_R \cdot (s/c)_R \tag{3.104}$$

The opening of the stator and rotor cascades is computed approximately from the outlet flow angle:

$$o_S = s_S \cdot (o/s)_S \approx s_S \cdot \cos(\alpha_2) \tag{3.105}$$

$$o_R = s_R \cdot (o/s)_R \approx s_R \cdot \cos(\beta_3) \tag{3.106}$$

The maximum blade thickness of stator and rotor blades is determined from the chord according to:

$$t_{max,S} = c_S \cdot (t_{max}/c)_S \tag{3.107}$$

$$t_{max,R} = c_R \cdot (t_{max}/c)_R \tag{3.108}$$

In this equation, the ratio of maximum blade thickness to chord is determined from the piecewise formula recommended in Kacker and Okapuu (1982):

$$(t_{max}/c) = \begin{cases} 0.15 & \text{for} \quad \theta \leq 40^\circ & (3.109) \\ 0.15 + \dfrac{0.25 - 0.15}{120 - 40} \cdot (\theta - 40) & \text{for} \quad 40^\circ \leq \theta \leq 120^\circ & (3.110) \\ 0.25 & \text{for} \quad \theta \geq 120^\circ & (3.111) \end{cases}$$

The deflection angle is $\theta = |\alpha_1 - \alpha_2|$ for stator blades and $\theta = |\beta_2 - \beta_3|$ for rotor blades.

The trailing edge thickness is defined as a fraction of the blade spacing and the tip clearance thickness is defined as a fraction of the mean radius. However, the minimum value of both parameters is limited to 0.2 mm because of manufacturing constraints. This value is also adopted in other works such as Astolfi and Macchi (2015).

$$t_{te} = \max(2 \cdot 10^{-4}\ \text{m},\ 0.02 \cdot s) \tag{3.112}$$

$$t_{cl} = \max(2 \cdot 10^{-4}\ \text{m},\ 0.001 \cdot r_m) \tag{3.113}$$

The optimization of the stagger angle requires detailed computations of the fluid flow around the blades and it is not part of a mean-line preliminary analysis. In this work, the stagger angle was determined using the simple formula suggested by Dixon and Hall (2013). This formula assumes that the camber line of the blades is a circular arc.

$$\xi_S = \frac{\alpha_1 + \alpha_2}{2} \tag{3.114}$$

$$\xi_R = \frac{\beta_2 + \beta_3}{2} \tag{3.115}$$

The axial chord are then determined from the blade chord and stagger angles:

$$b_S = c_S \cdot \cos(\xi_S) \tag{3.116}$$

$$b_R = c_R \cdot \cos(\xi_R) \tag{3.117}$$

Finally, the flaring angles or rotor and stator cascades are determined from the blade height differences and the axial chords:

$$\tan(\delta_{fl\,S}) = \frac{H_2 - H_1}{2\,b_S} \tag{3.118}$$

$$\tan(\delta_{fl\,R}) = \frac{H_3 - H_2}{2\,b_R} \tag{3.119}$$

Once the velocity triangles, thermodynamic properties and geometric parameters are determined the turbine losses can be computed. All the parameters required to use the Ainley-Mathieson, Dunham-Came, or Kacker-Okapuu loss correlations follow from the degrees of freedom and Eqs. 3.76 to 3.119. In this work, the Kacker-Okapuu method was used because it is an improvement of the other two loss systems. The equations used in order to compute the loss coefficients Y_S and Y_R have already been detailed in Section 2.10 and they will not be repeated here.

Once the enthalpy loss coefficients are computed, they can be used to determine the entropy increase predicted by the loss correlations. For the case of stator cascades:

$$h_{2s} = h_2 - Y_S \cdot \frac{1}{2} {v_2}^2 \tag{3.120}$$

$$\tilde{p}_2 = p(h_{2s}, s_1) \tag{3.121}$$

$$\tilde{s}_2 = s(\tilde{p}_2, h_2) \tag{3.122}$$

And for the case of rotor cascades:

$$h_{3s} = h_3 - Y_R \cdot \frac{1}{2} {w_3}^2 \tag{3.123}$$

$$\tilde{p}_3 = p(h_{3s}, s_2) \tag{3.124}$$

$$\tilde{s}_3 = s(\tilde{p}_3, h_3) \tag{3.125}$$

In general, $s_2 \neq \tilde{s}_2$ and $s_3 \neq \tilde{s}_3$ and the values of the entropy given by the degrees of freedom will be modified by the optimization algorithm to enforce the equality constraints given by Eqs. 3.66 and 3.67.

As mentioned in the last paragraph of Section 2.9, the enthalpy loss coefficients (not the stagnation pressure loss coefficients) were used to compute the losses. This is because computing $\tilde{s}_2$ or $\tilde{s}_3$ using the enthalpy loss coefficients involves just one enthalpy-entropy call to the equation of state, while using the stagnation pressure loss coefficients would require the numerical solution of an algebraic nonlinear equation. The solution of this equation involves an enthalpy-entropy call to the equation of state at each iteration, increasing significantly the computational cost of the optimization.

The procedure described to this point applies to one stage. The rest of the stages are computed in the same manner using the parameters at the outlet of one stage as the inlet for the next one. Once all the turbine parameters are found, the constraints are evaluated and the objective function (total-to-static efficiency) is computed. At this point, any other variable of interest can be computed. After this, the optimization algorithm in MATLAB checks if the maximum tolerance for the constraints is violated and, if this is the case, the degrees of freedom are modified and the cycle simulation function is called again.

If the constraints are not violated, the MATLAB algorithm checks if the solution is optimal. The solution will be considered as optimal if the norm of the change in the vector of degrees of freedom (step size), the value of the change in the objective function, and the first order optimality measure (as implemented in MATLAB) are less than the tolerances prescribed by the user. If the tolerances are violated the degrees of freedom are modified and the cycle simulation function is called again. If the tolerances are not violated the optimization is stopped and the optimal turbine design is plotted (loss breakdown, velocity triangles, thermodynamic diagrams, axial view, and cascade view) and saved as MATLAB (.mat) and Excel (.xmsl) files for further processing of the solution.

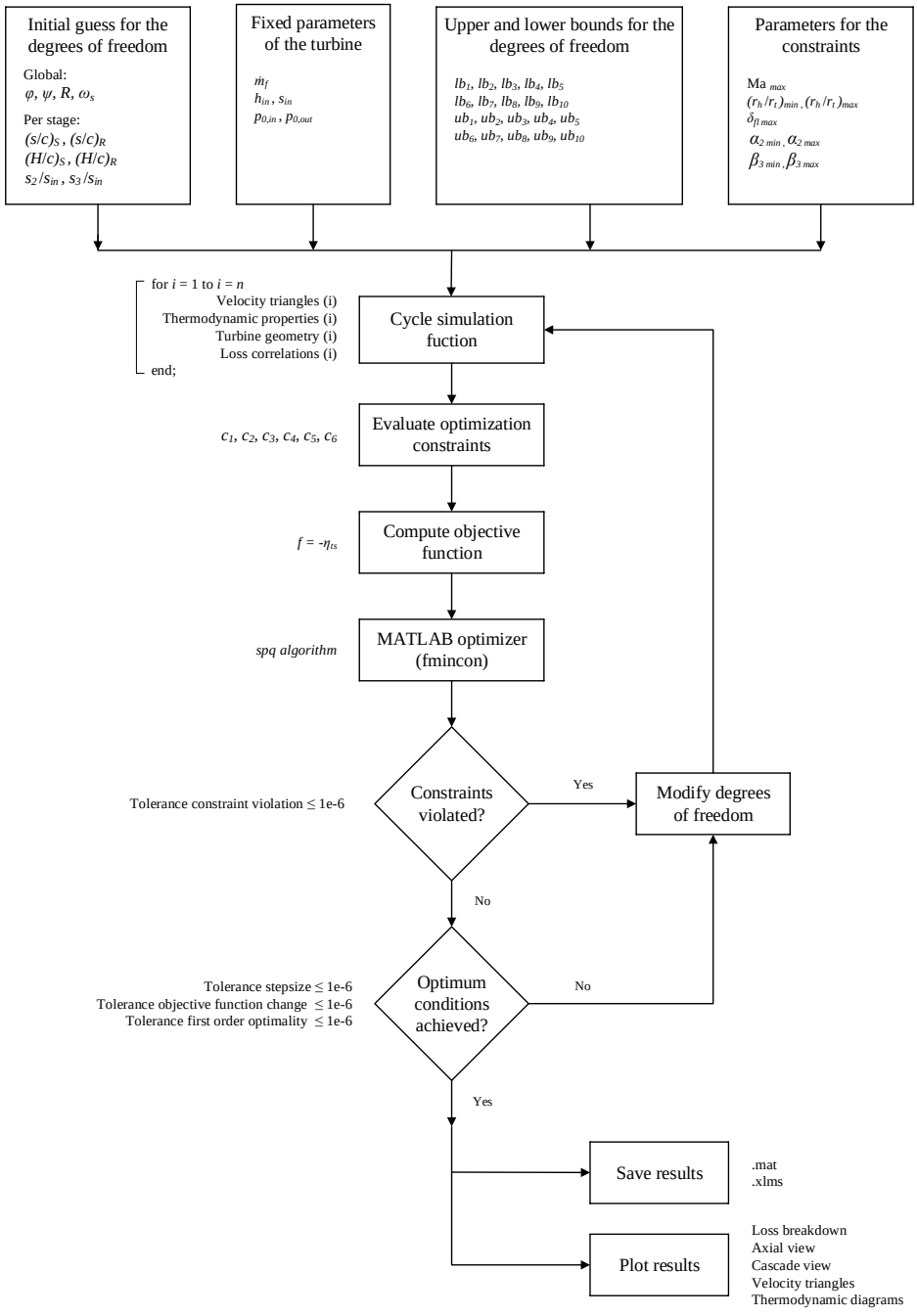

Figure 3.2: Turbine optimization algorithm.

Chapter 4

Results and conclusions

4.1 Fluid screening

From the 80 fluids originally considered in this work, only the 30 working fluids summarized in Table 4.1 met all of the screening criteria described in Section 3.2.

The list of working fluids is too large to perform an exhaustive Rankine cycle and turbine optimization for all of them. In addition, the objective of this work is not to carry a comprehensive analysis of the case study proposed in Section 3.1, but to develop a methodology for the fluid screening and optimization of Rankine cycles and axial turbines. For this reason, two representative fluid candidates were selected, R152a and hexane, in order to illustrate the methodologies described in Chapter 3. The molecular structures of these two fluid are shown in Fig. 4.1.

R152a, also known as difluoroethane, is an low-flammability hydrofluorocarbon with null ozone depletion potential and low global warming potential, $\mathrm{GWP} = 124$. As the critical temperature of R152a is lower than the temperature of the heat source, $T_{crit}/T_{hot\ source} = 0.739 < 1$, the optimal cycle configuration is expected to be transcritical.

Hexane is a flammable linear hydrocarbon with null ozone depletion and global warming potentials. The critical temperature of hexane is almost equal to the temperature of the heat source, $T_{crit}/T_{hot\ source} = 0.971 \approx 1$. For this reason, the optimal cycle configuration is expected to be subcritical. Whether this optimal configuration is saturated or superheated has to be determined optimizing the Rankine cycle.

The results of the power cycle and axial turbine optimization for these two fluids are presented in Section 4.2 and Section 4.3, respectively.

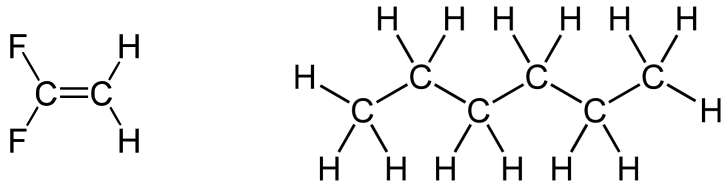

Figure 4.1: Molecular structures of R152a and hexane.

Table 4.1: Suitable working fluids after the screening.

Number	Chemical name	Alternative name	Class	$T_{crit}/T_{hot\ source}$
1	Ethane	R170	Alkane	0.584
2	Propane	R290	Alkane	0.707
3	n-Butane	R600	Alkane	0.813
4	2-Methylpropane	Isobutane - R600a	Alkane	0.780
5	Pentane	R601	Alkane	0.898
6	2-Methylbutane	Isopentane-R601a	Alkane	0.880
7	2,2-Dimethylpropane	Neopentane	Alkane	0.829
8	Hexane	-	Alkane	0.971
9	2-Methylpentane	Isohexane	Alkane	0.951
10	Heptane	-	Alkane	1.032
11	Propene	Propylene - R1270	Alkene	0.696
12	1-Butene	Butene	Alkene	0.801
13	Cis-2-butene	Cis-butene	Alkene	0.833
14	Trans-2-butene	Trans-butene	Alkene	0.819
15	2-Methyl-1-propene	Isobutene	Alkene	0.799
16	Cyclopentane	-	Cycloalkane	0.978
17	Cyclohexane	-	Cycloalkane	1.058
18	Methylcyclohexane	-	Cycloalkane	1.094
19	n-Propylcyclohexane	-	Cycloalkane	1.206
20	Benzene	-	Aromatic	1.074
21	Methylbenzene	Toluene	Aromatic	1.131
22	1,1-Difluoroethane	R152a	HFC	0.739
23	Hexamethyldisiloxane	MM	Linear Siloxane	0.991
24	Propanone	Acetone	Ketone	0.971
25	Ethyl alcohol	Ethanol	Alcohol	0.982
26	Methanol	Methanol	Alcohol	0.981
27	Methoxymethane	Dimethylether	Ether	0.765
28	Ammonia	R717	Inorganic	0.775
29	Carbon dioxide	R744	Inorganic	0.581
30	Water	R718	Inorganic	1.237

4.2 Cycle optimization

The Rankine cycle optimization methodology presented in Section 3.3 was applied for a recuperated cycle using R152a and for a simple cycle using hexane. The fixed parameters for the simulation were those discussed in Section 3.3.2, in particular the polytropic efficiency of the turbine was 75%.

The objective is not to find the optimal working fluid, but to give two examples of Rankine cycles optimized with the methodology described in Section 3.3 and to obtain the thermodynamic boundaries for the axial turbine optimization presented Section 4.3.

4.2.1 Recuperated cycle with R152a

The recuperated cycle layout was selected for R152a because the cycle was expected to be transcritical with a large superheating after the expansion. This is indeed the case as seen in the T–s diagram of Fig. 4.2. R152a is an isentropic–wet fluid, but this is not relevant in this case because the expansion occurs far away from the vapor saturation curve.

In addition to the common T–s diagram, the T–h diagram of the cycle is plotted in Fig. 4.3. This diagram is useful because the horizontal distances between cycle points represent heat flow for the case of heat exchangers and work for the case of turbomachinery. Observing the T–h diagram reveals that the back work ratio of the cycle is appreciable (ratio of horizontal distances from f_1 to f_2 and from f_4 to f_5). The numerical value of the back work ratio of the cycle is 13%. This is a relatively high value compared to the back work ratio of conventional steam cycles (<1%) and it indicates that the performance of the cycle is sensitive to the efficiency of the pump.

The heat exchange with the heat source and sink, as well as in the internal recuperator, is shown in Fig. 4.4. As a result of the supercritical pressure, there is no phase change in the primary heat exchanger and the heat transfer occurs at a gliding temperature. In addition, the minimum temperature difference occurs close the the cold end of the hear exchanger, but the pinch point is not clearly located.

It can also be observed that the internal heat exchanger in the recuperator is around one third of the heat rejected in the condenser. This heat exchange is possible due to the high superheating that exists at the outlet of the turbine. The pinch point of the recuperator is located in the cold end. This is because the heat capacity of the liquid leaving the condenser is higher than the heat capacity of the vapor leaving the turbine.

The first and second law efficiencies are summarized in Table 4.3. The recovery efficiencies are not 100% because of the limitation for the lowest temperature of the heat source. The first law efficiency of the plant might appear to be low[1], $\eta_{\mathrm{I}\,plant}$ = 13.91%. This is because the temperature of the heat source, and hence its exergy content, are low. On the other hand, the values of the second law efficiency are reasonably high and they can be compared to those of conventional power plants.

The thermodynamic states of all the cycle points, are summarized in Table 4.2.

[1] The efficiency of conventional steam cycles can be of the order of 40% (of the fuel heating value). Advanced combined cycles with several pressure levels can reach first law efficiencies higher than 60%.

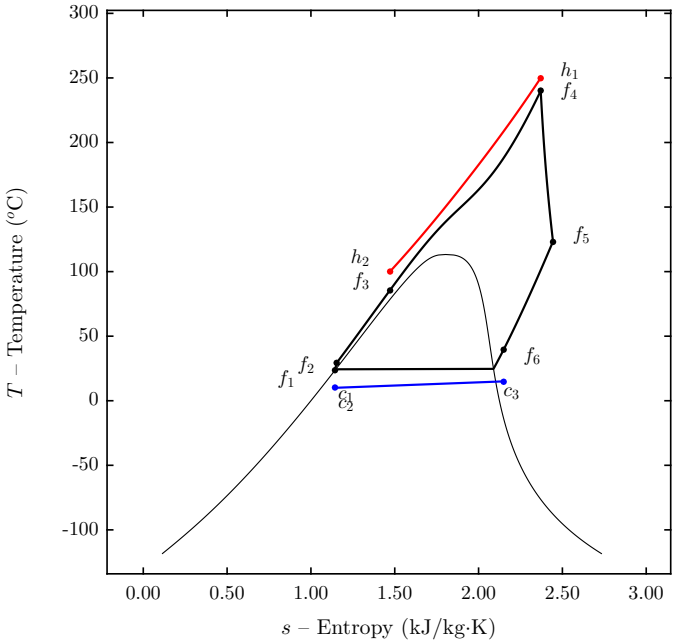

Figure 4.2: T–s diagram of the recuperated cycle using R152a.

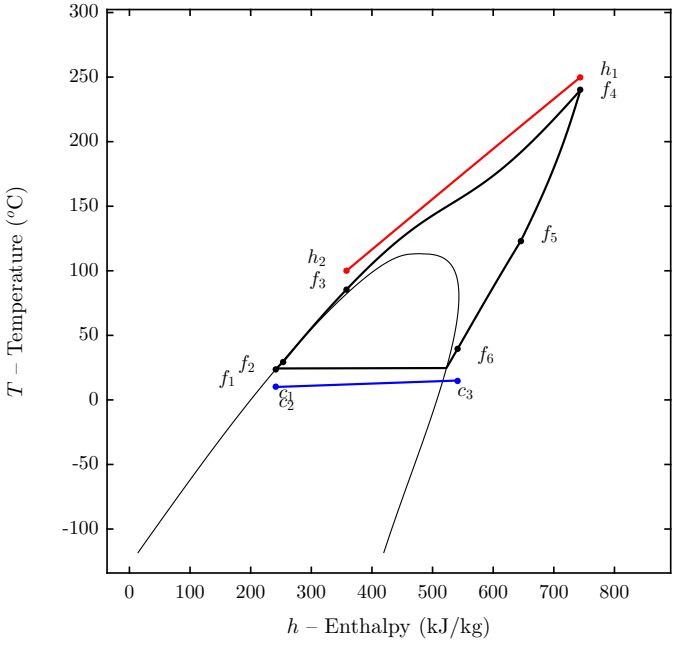

Figure 4.3: T–h diagram of the recuperated cycle using R152a.

Table 4.2: Thermodynamic points of the recuperated cycle using R152a.

Point	Fluid	T (°C)	p (bar)	$\rho\left(\frac{\text{kg}}{\text{m}^3}\right)$	$h\left(\frac{\text{kJ}}{\text{kg}}\right)$	$s\left(\frac{\text{kJ}}{\text{kg·K}}\right)$	$e\left(\frac{\text{kJ}}{\text{kg}}\right)$
f_1	R152a	23.356	5.851	903.678	240.774	1.142	44.628
f_2	R152a	29.519	87.113	915.946	253.532	1.155	53.768
f_3	R152a	85.518	86.242	768.899	358.029	1.471	68.671
f_4	R152a	240.000	85.380	172.767	743.973	2.371	199.920
f_5	R152a	123.299	5.970	12.541	645.751	2.444	80.964
f_6	R152a	39.519	5.910	16.934	541.254	2.149	59.872
h_1	Air	250.000	1.023	0.681	527.354	7.429	68.344
h_2	Air	100.000	1.013	0.946	374.094	7.087	11.957
c_1	Water	10.000	1.013	999.702	42.119	0.151	0.000
c_2	Water	10.000	1.023	999.703	42.120	0.151	0.001
c_3	Water	15.000	1.013	999.103	63.077	0.224	0.183

Table 4.3: Summary of efficiencies for the optimal cycle using R152a.

Fluid	$\eta_{\text{I}\,recov}$	$\eta_{\text{I}\,cycle}$	$\eta_{\text{I}\,plant}$	$\eta_{\text{II}\,recov}$	$\eta_{\text{II}\,cycle}$	$\eta_{\text{II}\,plant}$
R152a	0.6281	0.2214	0.1391	0.8251	0.6017	0.4965

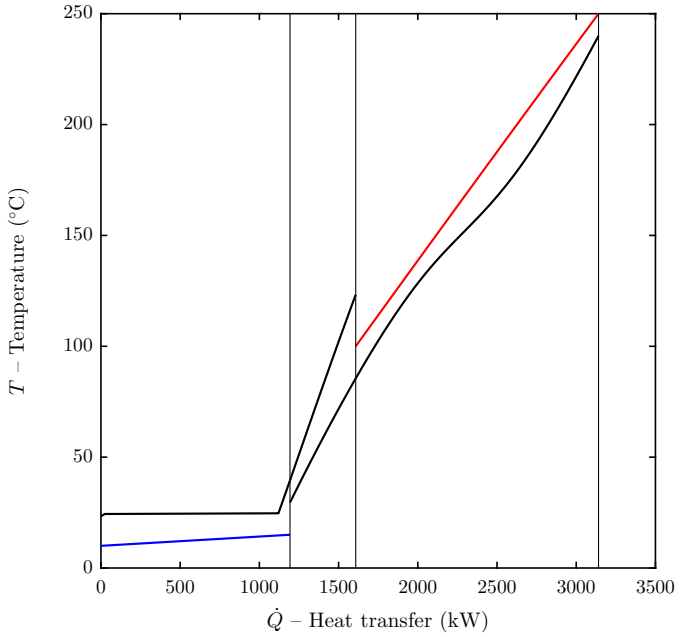

Figure 4.4: T–$\dot{Q}$ diagram of the recuperated cycle using R152a.

4.2.2 Simple cycle with hexane

The simple cycle layout was selected for hexane for the sake of illustration. The thermodynamic optimization revealed that the optimum cycle is saturated and the pressure is close to the critical pressure. As seen in the T–s diagram of Fig. 4.5, hexane is a dry fluid; the expansion starts at the saturation line and ends in the superheated vapor region.

The T–h diagram shown in Fig. 4.6 reveals that the back work ratio of the simple cycle using hexane is smaller than that of the recuperated cycle using R152a. This means that the performance of the cycle using hexane is less sensitive to the efficiency of the pump. The back work ratio of the simple hexane cycle is 3%. This value is still higher than that of conventional steam cycles because the pressure at the outlet of the pump is close to the critical pressure of the working fluid.

The heat exchange with the heat source and sink is shown in Fig. 4.7. Part of the heat exchange in the primary heat exchanger occurs at a constant temperature due to the phase change. In addition, it can be observed that the pinch point is located at the phase change.

As hexane is a dry fluid and the expansion ends in the superheated vapor region, part of the heat rejection in the condenser occurs at a high temperature difference, see Fig. 4.7. This leads to higher exergy destruction and a lower cycle efficiency. This thermal energy wasted in the condenser could be recovered using a recuperator as in the case of the R152a cycle. Adding a recuperator for the hexane cycle was not considered because the recuperated cycle was already illustrated with R152a.

The first and second law efficiencies are summarized in Table 4.5. The recovery efficiencies are lower than 100% because of the limitation for the lowest temperature of the heat source. The cycle efficiency of the simple hexane cycle is lower than that of the recuperated R152a cycle because the heat transfer exergy destruction is higher. The reasons for this are: 1) in the simple hexane cycle, some high quality heat is rejected in the condenser and 2) in the case of the transcritical R152a cycle, the heat transfer in the primary heat exchange occurs at a gliding temperature, minimizing the temperature differences.

The thermodynamic states of all the cycle points are summarized in Table 4.4.

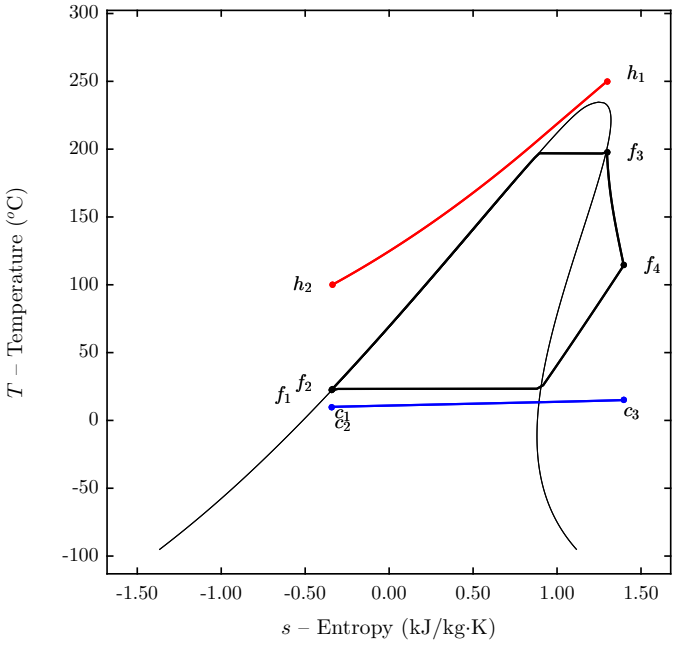

Figure 4.5: T–s diagram of the recuperated cycle using hexane.

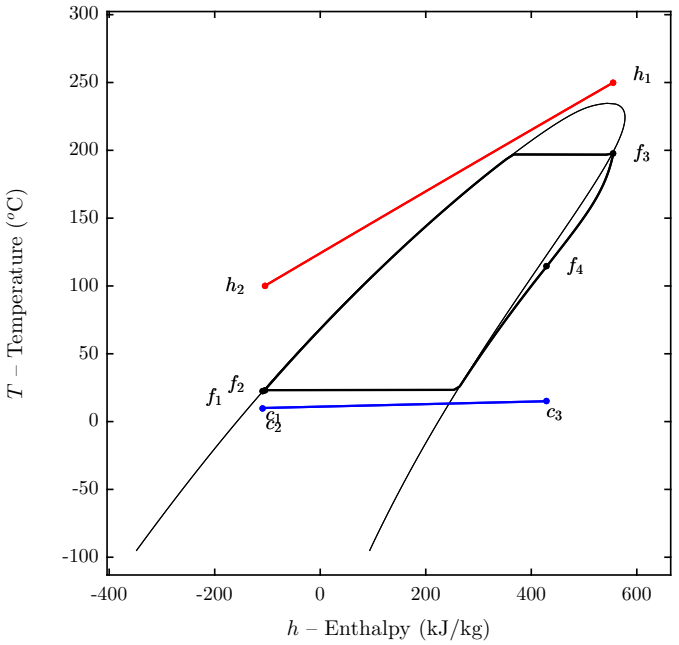

Figure 4.6: T–h diagram of the recuperated cycle using hexane.

Table 4.4: Thermodynamic points of the simple cycle using hexane.

Point	Fluid	T (°C)	p (bar)	$\rho\left(\frac{\text{kg}}{\text{m}^3}\right)$	$h\left(\frac{\text{kJ}}{\text{kg}}\right)$	$s\left(\frac{\text{kJ}}{\text{kg}\cdot\text{K}}\right)$	$e\left(\frac{\text{kJ}}{\text{kg}}\right)$
f_1	Hexane	22.201	0.187	657.26	-109.06	-0.342	0.44
f_2	Hexane	23.175	17.308	658.29	-105.34	-0.338	3.10
f_3	Hexane	197.780	17.135	58.61	555.52	1.297	200.86
f_4	Hexane	114.344	0.189	0.51	429.09	1.397	46.07
h_1	Air	250.000	1.023	0.68	527.35	7.429	68.34
h_2	Air	100.000	1.013	0.95	374.09	7.087	11.96
c_1	Water	10.000	1.013	999.70	42.12	0.151	0.00
c_2	Water	10.000	1.023	999.70	42.12	0.151	0.00
c_3	Water	15.000	1.013	999.10	63.08	0.224	0.18

Table 4.5: Summary of efficiencies for the optimal cycle using hexane.

Fluid	$\eta_{\text{I}\,recov}$	$\eta_{\text{I}\,cycle}$	$\eta_{\text{I}\,plant}$	$\eta_{\text{II}\,recov}$	$\eta_{\text{II}\,cycle}$	$\eta_{\text{II}\,plant}$
Hexane	0.6281	0.1856	0.1166	0.8251	0.5045	0.4163

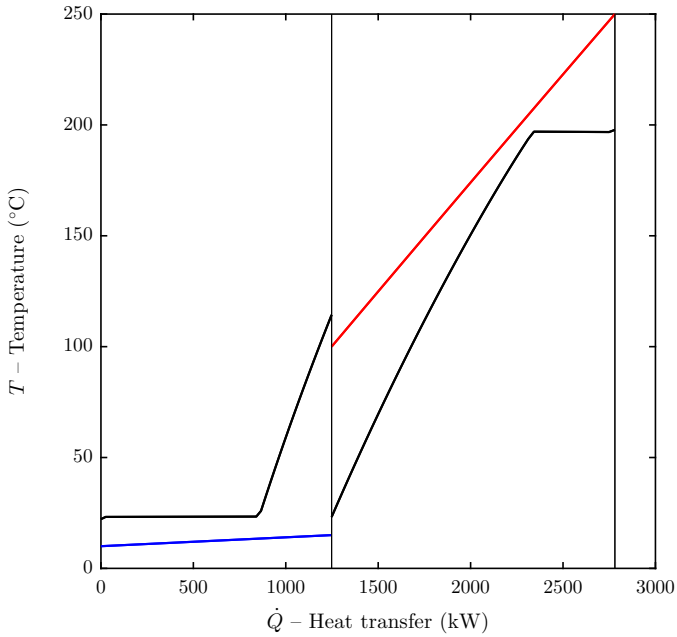

Figure 4.7: T–$\dot{Q}$ diagram of the simple cycle using hexane.

4.3 Axial turbine optimization

The axial turbine optimization methodology presented in Section 3.4 was applied to the optimal Rankine cycles presented in Section 4.2. The fixed parameters for the turbine optimization were obtained from the cycle optimization. In particular, two turbine designs are considered: a two-stage axial turbine for the recuperated cycle using R152a and a three stage axial turbine for the simple cycle using hexane.

Again, the objective is not to find the best turbine design, but to give two examples of axial turbines optimized with the methodology described in Section 3.4, to identify challenges in the turbine design, and to serve as a basis for more advanced turbine design methods in future works.

As there are more than one hundred variables involved in the optimization of each of these two axial turbines, the results and discussion of this section only cover the most important features of the design, to the opinion of this writer. In order to give a general outlook of both turbine designs, the breakdown of losses is shown in Fig. 4.8 and Fig. 4.9.

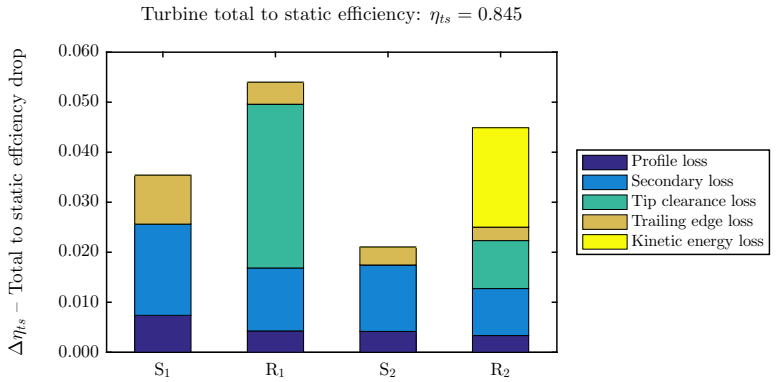

Figure 4.8: Loss distribution for the two-stage axial turbine using R152a.

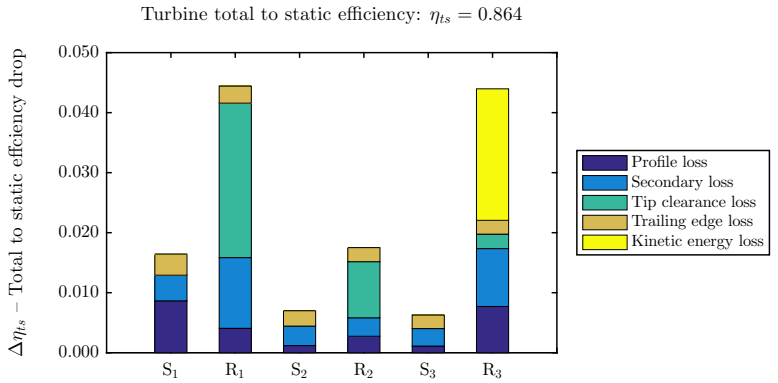

Figure 4.9: Loss distribution for the three-stage axial turbine using hexane.

4.3.1 Two-stage turbine for the recuperated R152a cycle

A two-stage axial turbine was optimized for the R152a recuperated cycle presented in Section 4.2.1. The cycle optimization was performed assuming a polytropic efficiency of 75% for the turbine, while the optimized two-stage turbine reached a total-to-static efficiency of 84.5%. This means that the performance of the cycle was underestimated assuming a low value for the polytropic efficiency.

The breakdown of the losses of the two-stage turbine is shown in Fig. 4.8. The clearance losses are appreciable in rotor cascades and zero in stator cascades. In addition, the clearance loss in the first rotor is much larger than in the second rotor. This is because the blades of the first rotor cascades are shorter and the same clearance gap leads to a larger efficiency drop. The second rotor stage includes the kinetic energy loss that is not recovered since there is no diffuser downstream the turbine.

The geometry of the turbine is shown in Fig. 4.10 (axial view) and in Fig. 4.11 (cascade view). The axial flaring is limited by the optimization constraints and the blade aspect ratios and pitch to chord ratios are within reasonable limits. A closer inspection into the numerical values, see Table 4.6, reveals that the dimensions of the turbine are very small: the mean radius is 2.46 cm and the axial length is 5.03 cm. The reason why the turbine is so small is that that the density at the inlet of the turbine is high (supercritical conditions), leading to very compact designs. In practice, it could be challenging to manufacture a turbine of such small size.

In addition, the angular speed of the turbine is very high, almost 10^5 rpm. The small dimensions and high angular speed will lead to high disk friction losses that could reduce the power output of the turbine by a large extent. These losses were not included in this work but they should be accounted to draw any definite conclusion from the optimization.

As seen in Fig. 4.11, the blades have axial (or almost axial entries) and they deflect the flow to a large extent. The velocity triangles of the turbine are shown in Fig. 4.12. As the repeating stage assumption was used in the optimization, the velocity triangles of all the stages are equal. It can be observed that the velocity triangles are not perfectly symmetric ($R < 0.50$), and that they are quite flat and skewed ($\phi < 0.50$). In addition, the velocity triangles overlap, which means that the work coefficient is smaller than unity ($\psi < 1.00$).

Regarding the thermodynamics of the expansion, real gas effects are moderate along most of the expansion, see Fig. 4.13. Despite the pressure at the inlet of the turbine is supercritical, the temperature is relatively high and real gas effects are not too strong ($Z \approx 0.80$). In addition, it can be observed that the compressibility factor approaches one as the pressure is reduced and that the expansion occurs far away from the saturation curve.

The speed of sound remains more or less constant along the expansion, see the blue solid line in Fig. 4.14. The speed of sound of R152a is lower than the ideal gas speed (red solid line) due to real gas effects along the expansion. In addition, the absolute velocity (solid green line) and relative velocity (dashed green line) are plotted in Fig. 4.14. It can be observed that the velocity at the inlet of stators and rotors is subsonic and that the flow is accelerated to slightly supersonic conditions at the outlet of the cascades. As seen in Table 4.6, the maximum value of the Mach number within the turbine is 1.132.

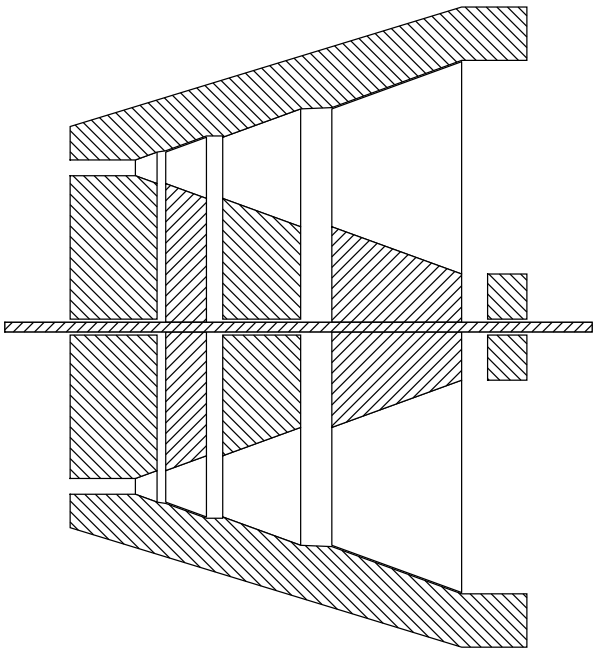

Figure 4.10: Axial view of the two-stage axial turbine using R152a. Horizontal and vertical axes are on the same scale.

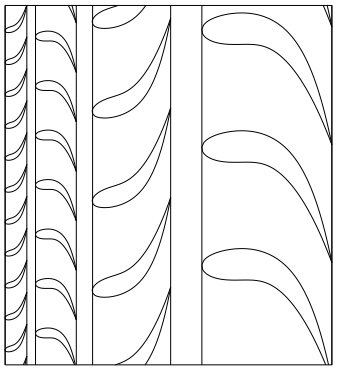

Figure 4.11: Cascade view of the two-stage axial turbine using R152a. Horizontal and vertical axes are on the same scale.

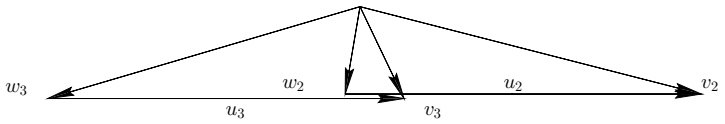

Figure 4.12: Velocity triangles of the two-stage axial turbine using R152a.

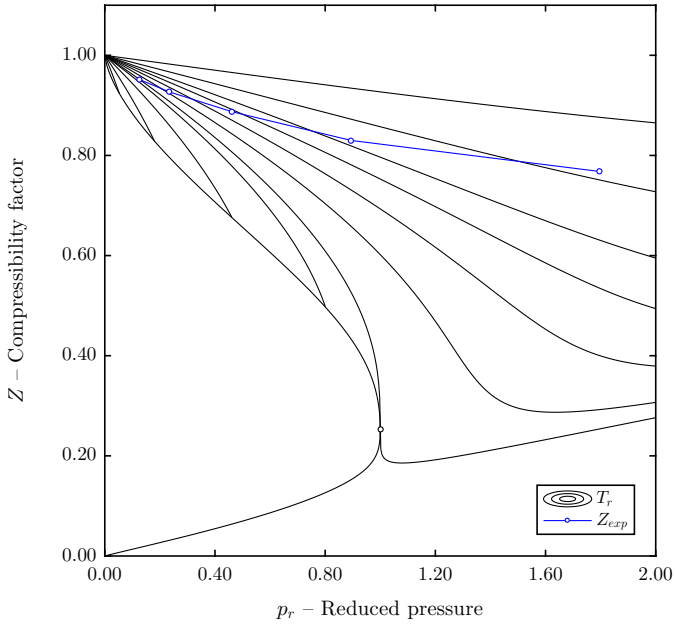

Figure 4.13: Compressibility factor along the expansion for the two-stage axial turbine using R152a.

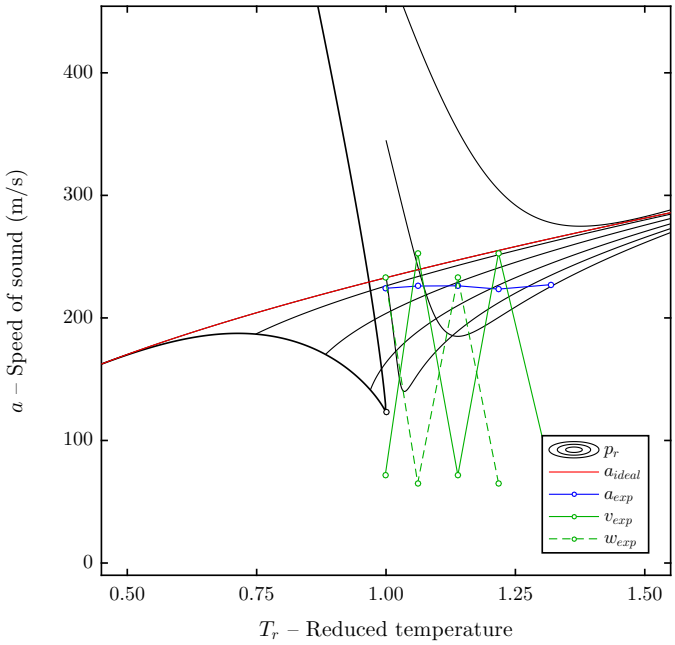

Figure 4.14: Speed of sound along the expansion for the two-stage axial turbine using R152a.

4.3.2 Three-stage turbine for the simple hexane cycle

A three-stage axial turbine was optimized for the hexane simple cycle presented in Section 4.2.2. The cycle optimization was performed assuming a polytropic efficiency of 75% for the turbine, while the optimized three-stage turbine reached a total-to-static efficiency of 86.4%. This means that the performance of the cycle was underestimated assuming a low value for the polytropic efficiency.

The breakdown of the losses of the two-stage turbine is shown in Fig. 4.9. It can be observed that the clearance loss dominates, specially in the first rotor. Clearance losses in the second rotor are less than half and the corresponding loss in third rotor is almost negligible. The clearance loss in the first rotor cascade is large because its dimensions are very small, see Fig. 4.15 or Fig. 4.16.

The reason why the first stage is so small is the high volume ratio across the expansion $V_r = \rho_{in}/\rho_{out} > 100$. This parameter is imposed by the cycle and it can not be influenced by the turbine design. As the repeating stage assumption requires the axial velocity to be constant, a high volume ratio implies that the the blade height of the first stages has to be much smaller than that of the last stages. This problem could be addressed if the constraint of using repeating stages was relaxed and the axial velocity could be varied along the turbine. Indeed, using a low axial velocity in the inlet stages would lead to longer blades and lower leakage losses.

Despite the first stage is too small, the numerical values shown in Table 4.6 indicate that the turbine dimensions are moderate: the mean radius is 9.47 cm and the axial length is 41.53 cm. In addition, the angular speed (ω = 27500 rpm) is much lower than for the transcritical R152a turbine.

Regarding the velocity triangles of the turbine, see Fig. 4.17, it can be seen that the nozzle entry is not axial and that the deflection is smaller than in the R152a two-stage turbine. In addition to this, the triangles are almost almost perfectly symmetrical ($R \approx$ = 0.50), very flat ($\phi <$ 0.50), and they overlap ($\psi <$ 1.00).

As seen in Fig. 4.18, there are strong real gas effects at the beginning of the expansion ($Z \approx 0.70$). This is because the pressure is close to the critical pressure ($p_r \approx 0.50$) and the expansion starts close to the vapor saturation line. At the end of the expansion, the pressure is very low and hexane behaves as an ideal gas ($Z \approx 1.00$).

Fig. 4.19 shows the fluid velocity (solid and dashed green lines) and the speed of sound (solid blue line) along the expansion. The flow is subsonic at the inlet of all stator and rotor cascades and it is accelerated to moderate supersonic conditions at the outlet. The maximum Mach number, Ma = 1.318, occurs at the outlet of the first stator. The reason for this is that the speed of sound is low at the inlet of the turbine due to the strong real gas effects close to the vapor saturation line.

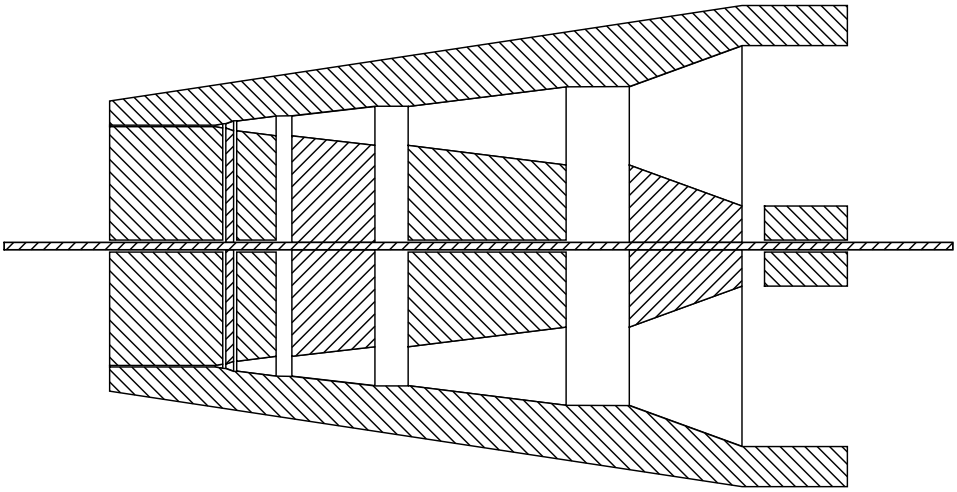

Figure 4.15: Axial view of the three-stage axial turbine using hexane. Horizontal and vertical axes are on the same scale.

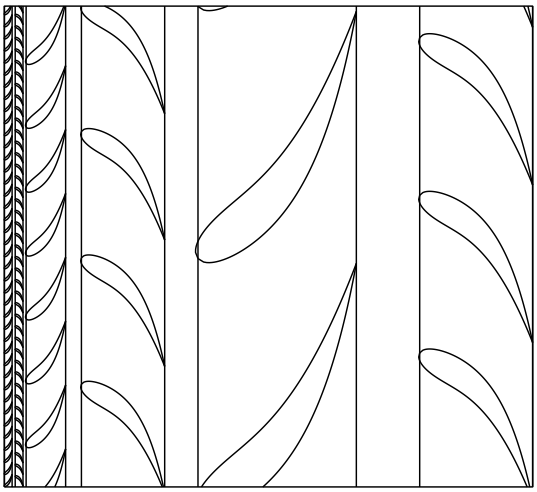

Figure 4.16: Casacade view of the three-stage axial turbine using hexane. Horizontal and vertical axes are on the same scale.

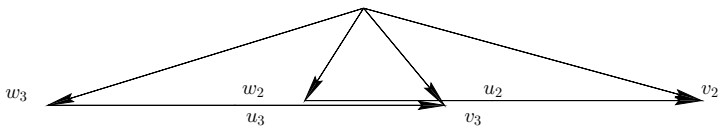

Figure 4.17: Velocity triangles of the three-stage axial turbine using hexane.

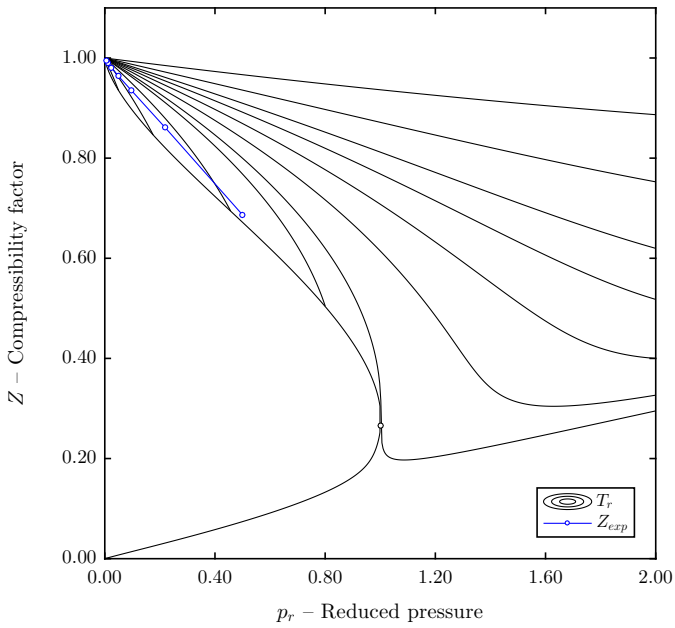

Figure 4.18: Compressibility factor along the expansion for the three-stage axial turbine using hexane.

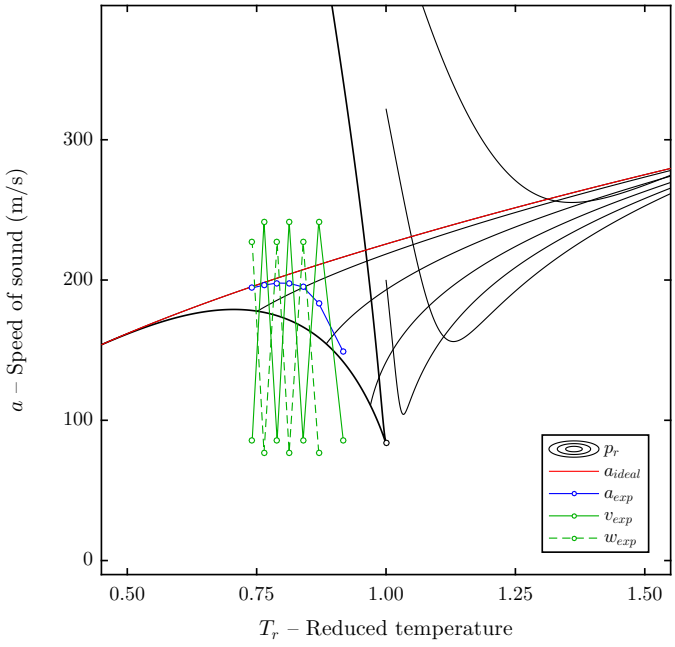

Figure 4.19: Speed of sound along the expansion for the three-stage axial turbine using hexane.

4.4 Sensitivity analysis

The two examples discussed in the previous sections, the recuperated R152a cycle with a two-stage axial turbine and the simple hexane cycle with a three-stage axial turbine, illustrated the cycle and turbine optimization methodology. The insight gained with these two examples is complemented with the sensitivity analysis presented in this section. The impact of turbine polytropic efficiency on the cycle performance and the impact of the number of stages on the turbine design is investigated. For that, the cycle optimization of Section 4.2 was repeated varying the turbine polytropic efficiency from 50% to 100% and the turbine optimization of Section 4.3 was repeated varying the number of stages from one to five.

Turbine polytropic efficiency

The second law efficiency of the power plant as a function of the turbine polytropic efficiency is plotted in Fig. 4.20. Both the simple hexane cycle and the recuperated R152a cycles are very sensitive to the turbine efficiency and, approximately, the second law efficiency halves when the turbine efficiency is halved from 100% to 50%. This sensitivity analysis highlights the importance of turbine design in the performance of Rankine cycles for waste heat recovery applications.

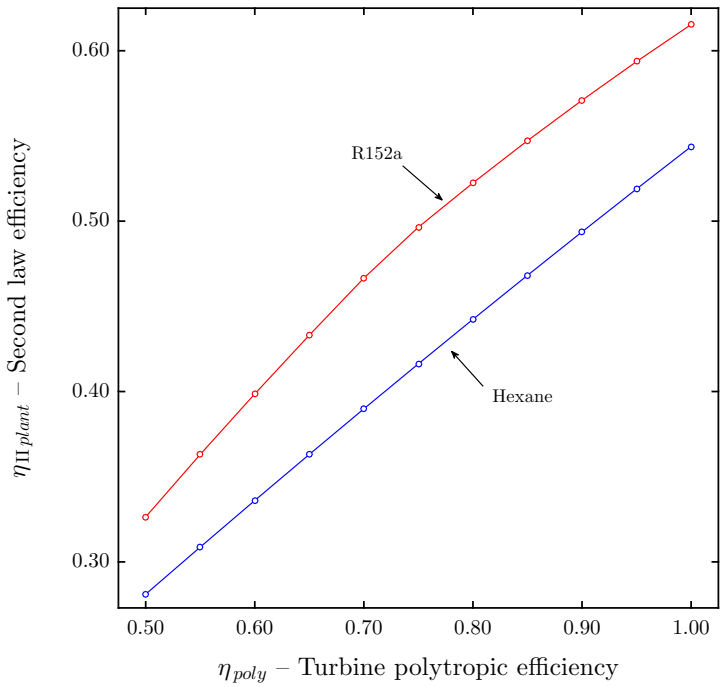

Figure 4.20: Second law efficiency as a function of the turbine polytropic efficiency for a recuperated-transcritical cycle using R152a and a simple-saturated cycle using hexane.

Table 4.6: Sensitivity analysis of the turbine design on the number of stages

Fluid	Stages	η_{ts}	η_{tt}	$\dot{W}$ (kW)	ω (rpm)	Ma_{max}	r_m (m)	L (m)
R152a	1	0.7850	0.8254	424.35	142656	1.521	0.0272	0.0542
R152a	2	0.8447	0.8618	432.25	99265	1.132	0.0246	0.0503
R152a	3	0.8682	0.8893	446.05	89805	0.971	0.0244	0.0526
R152a	4	0.8798	0.9004	451.67	82732	0.840	0.0252	0.0570
R152a	5	0.8878	0.9058	454.42	73212	0.753	0.0262	0.0625
Hexane	1	0.6873	0.7015	266.91	38489	1.771	0.0994	0.1894
Hexane	2	0.8019	0.8202	312.19	28938	1.536	0.0964	0.2871
Hexane	3	0.8643	0.8837	336.47	27530	1.318	0.0947	0.4153
Hexane	4	0.8748	0.8916	339.51	23921	1.185	0.0922	0.3110
Hexane	5	0.8847	0.9025	343.67	22323	1.119	0.0948	0.3420

Number of stages

The total-to-static efficiency of the turbine as a function of the number of stages is plotted in Fig. 4.21 for the hexane simple cycle and the recuperated R152a cycle. The simulations were performed for the optimal thermodynamic cycles assuming a turbine polytropic efficiency of 75%.

The turbine efficiency always increases with the number of stages. In addition, it can be observed that the efficiency is very sensitive when the number of stages is increased from one to two and from two to three (specially for the case of hexane). However, when the number of stages is further increased (four and five stages) the impact on the turbine efficiency is modest. As increasing the number of stages leads to more mechanically complex turbines, it seems reasonable to choose the lowest number of stages that yields a high value of efficiency.

Other variables of the turbine such as angular speed and maximum Mach number are also influenced by the number of stages, see Table 4.6. The angular speed as a function of the number of stages is plotted in Fig. 4.22 and it is seen that it is reduced as the number of stages increases. The angular speed of both the hexane and the R152a turbines is almost halved when the number of stages is increased from one to five. Reducing the angular speed is advantageous as it reduces disk friction losses that were not accounted in this work. Since disk friction losses are more or less proportional to the third power of angular speed, halving this variable would reduce the disk friction losses by a factor of eight.

The Mach number within the turbine is also reduced as the number of turbine increases. For the case of R152a, the maximum Mach number for a single stage turbine is larger than 1.50, while the maximum Mach number for a three-stage turbine is already lower than one. For the case of hexane, the Mach numbers are higher: the maximum Mach number of the single stage turbine is highly supersonic (1.771) while for a five-stage turbine the Mach number is almost sonic (1.119).

Finally, the data from Table 4.6 shows that the number of stages also affects the dimensions of the turbine (mean radius and axial length), but no clear trends can be analyzed.

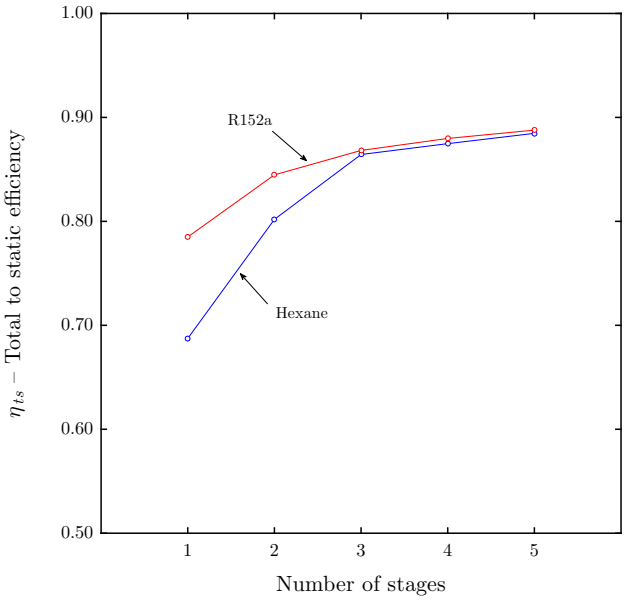

Figure 4.21: Total-to-static efficiency as a function of the number stages for R152a and hexane.

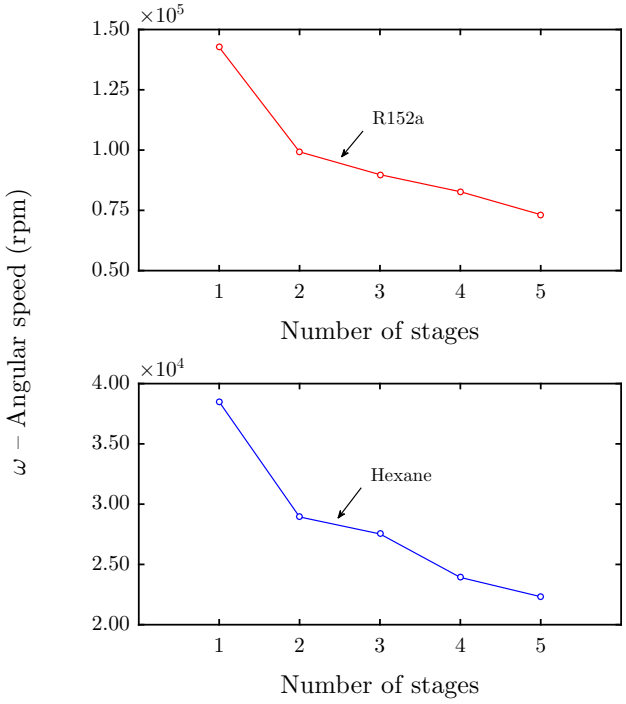

Figure 4.22: Angular speed as a function of the number stages for R152a and hexane.

4.5 Research challenges

Several research challenges related with Rankine cycle and axial turbine optimization were identified in this project and they are summarized in this section.

4.5.1 Equations of state

The optimization of Rankine cycles covers a wide range of thermodynamic conditions (liquid, two-phase, vapor, and gas) that the equations of state must be able to handle. In addition in transcritical cycles, it is possible to encounter states close to the critical point and the equations of state should be sufficiently accurate and robust to converge in these cases. The complex multiparameter equations of state contained in libraries like REFPROP cover all these thermodynamic conditions accurately and they are well suited for the optimization of Rankine cycles. In addition most of the function calls to the equations of state use pressure and enthalpy as independent variables. This type function calls are very robust and the computational time is relatively small. It is concluded that fluid libraries like REFPROP are an excellent option for the simulation of Rankine cycles using pure substances as working fluid.

For the case of turbine optimization, the only relevant states are gas and vapor. However, simple equations of state such as the ideal gas law or cubic equations of state are not recommended because it is usual to encounter strong real gas effects that limit the accuracy of these equations of state. Conversely, fluid libraries like REFPROP give very accurate properties of state. However, most of the function calls to the equations of state used during the turbine optimization used enthalpy and entropy as independent variables. This type of function calls are computationally expensive and they may not always converge (not robust). In this work, some numerical tricks had to be used to overcome the limitation of enthalpy-entropy calls in REFPROP, at the cost of higher computational time[2]. For this reason fluid libraries like REFPROP may not be the best option for the optimization of turbomachinery for Rankine cycles. Instead, other families of equations of state covered in Skaugen et al. (2016) may be better suited and they can be considered in future works.

4.5.2 Low speed of sound

As discussed in Section 2.6.4, the speed of sound of fluids used in Rankine cycles for waste heat recovery applications is lower than in conventional steam and gas turbines. The reasons for this are the relatively low temperature, low heat capacity ratios, high molecular mass, and presence of real gas effects.

As a consequence of the low speed of sound, it is relatively easy to reach Mach numbers higher than one at the outlet of stator (absolute Mach number) and rotor (relative Mach number) cascades. Supersonic flows are associated to higher losses due to the pressence of shock waves and the interaction of these shock waves with the boundary layers.

[2]This was not a big concern in this work because the computational time of each optimization was of the order of minutes. The computational time required by REFPROP would be prohibitive in more advanced simulations such as CFD analyses of blade design.

In addition, the losses in highly supersonic flows are not accurately predicted with the methods described in Section 2.9, adding uncertainty to the turbine optimization.

The challenges associated with supersonic flows can be addressed increasing the number of turbine stages, see Section 4.4, or accepting that the flow will be supersonic, carry out the detailed fluid dynamic analysis of supersonic blades, and try to minimize the losses with highly optimized blade geometries.

4.5.3 Repeating stage assumption

As discussed in Section 4.3.2, the repeating stage assumption described in Section 2.8.5 leads to unfeasible turbine designs when volume ratio across the expansion $V_r = \rho_{in}/\rho_{out}$ is high. The reason for this is that having repeating stages implies constant axial velocity and, due to conservation of mass, the blade height in the first stages becomes too small. This leads to unfeasible geometries and too large tip leakage losses.

If the repeating stage assumption is relaxed and the axial velocity is allowed to vary along the turbine it would be possible to use lower axial velocities in the first stages. This, in turn, would allow to have longer blades and lower leakage losses.

In addition, due to real gas effects, the speed of sound is usually lowest in the first stages and reducing the axial velocity in these sections would help to decrease the Mach number where it is most critical.

4.5.4 Integrated optimization

One of the limitations of this work is that the Rankine cycle and axial turbine optimizations were independent. The cycle optimization was based on a fixed value for the polytropic efficiency of the turbine and the turbine optimization based on the fixed boundary conditions from the cycle optimization.

The performance of the Rankine cycle and axial turbine could be improved if both systems were allowed to be optimized at the same time. If the optimization of both systems was integrated, the changes in the cycle optimization would affect the turbine design, and vice versa, leading to more efficient and plausible Rankine cycles and turbine designs.

4.6 Evaluation of objectives

The purpose of this section is to evaluate if the objectives set in Section 1.3 were accomplished and to what extent.

1. An extensive literature study of power cycles for waste heat recovery application including working fluid selection, possible cycle architectures and turbine technologies was performed in Chapter 2.
2. A fluid screening methodology involving thermodynamic and environmental criteria was developed in Section 3.2.
3. Simple and recuperated Rankine cycles were selected as thermodynamic cycles. A steady-state cycle optimization program was developed in MATLAB for each cycle layout, see Section 3.3.
4. Axial turbines were selected as the turbine architecture. A 1D mean-line turbine optimization program was developed in MATLAB, see Section 3.4.
5. A waste heat recovery case study was proposed, see Section 3.1. The methodologies for fluid screening (Section 4.1), cycle optimization (Section 4.2), and turbine optimization (Section 4.3) were applied to the proposed case study.

   In addition, a sensitivity analysis to study the effect of turbine polytropic efficiency on the performance of the cycle and the impact of the number of stages on the turbine design was conducted in Section 4.4.
6. Several research challenges were identified in this work and they were summarized and discussed in Section 4.5.

4.7 Further work

Possible research lines for future works in Rankine cycles for waste heat recovery applications include:

- Study other turbine architectures such as radial inflow, radial outflow, or hybrid.
- Develop software to optimize simultaneously the Rankine cycle and turbine.
- Develop an off-design turbine model.
- Carry out a detailed design and optimization of the blade and cascade geometry.

Bibliography

D. G. Ainley and C. R. Mathieson. An Examination of the Flow and Pressure Losses in Blade Rows of Axial-Flow Turbines. *Aeronautical Research Council reports And Memoranda*, 2891:1–33, 1951a.

D. G. Ainley and C. R. Mathieson. A Method of Performance Estimation for Axial-Flow Turbines. *Aeronautical Research Council reports And Memoranda*, 2974(2974):1–30, 1951b.

J. D. Anderson. *Fundamentals of Aerodynamics*. Tata McGraw-Hill Education, 5th edition, 2010.

G. D. Angelino and P. Colonna. Multicomponent working fluids for organics Rankine cycles. *Energy*, 23(6):449–463, 1998.

ASHRAE. Designation and safety classifications of refrigerants, 2000.

M. Astolfi and E. Macchi. Efficiency Correlations for Axial Flow Turbines Working With Non-Conventional Fluids. *ASME Orc 2015*, pages 1–12, 2015.

M. Astolfi, M. C. Romano, P. Bombarda, and E. Macchi. Binary ORC (Organic Rankine Cycles) power plants for the exploitation of medium-low temperature geothermal sources - Part A: Thermodynamic optimization. *Energy*, 66:423–434, 2014.

R. H. Aungier. *Turbine Aerodynamics*. ASME Press, 1st edition, 2006.

O. E. Balje. A Study on Design Criteria and Matching of Turbomachines: Part A – Similarity Relations and Design Criteria of Turbines. *Journal of Engineering for Power*, 84 (1):83–102, 1962.

M. P. Boyce. *Gas Turbine Engineering Handbook*. Elsevier, 4th edition, 2011.

H. Chen, D. Y. Goswami, and E. K. Stefanakos. A review of thermodynamic cycles and working fluids for the conversion of low-grade heat. *Renewable and Sustainable Energy Reviews*, 14(9):3059–3067, 2010.

Y. Chen. *Thermodynamic Cycles using Carbon Dioxide as Working Fluid*. PhD thesis, Royal Institute of Technology in Stockholm (KTH), 2011.

P. Colonna, E. Casati, C. Trapp, T. Mathijssen, J. Larjola, T. Turunen-Saaresti, and A. Uusitalo. Organic Rankine Cycle Power Systems: From the Concept to Current Technology, Applications, and an Outlook to the Future. *Journal of Engineering for Gas Turbines and Power*, 137(10):1–19, 2015.

H. R. M. Craig and H. J. A. Cox. Performance Estimation of Axial Flow Turbines. *Proceedings of the Institution of Mechanical Engineers*, 185(1):407–424, 1970.

J. S. Daniel and G. J. M. Velders. Scientific Assessment of Ozone Depletion, 2006.

J. D. Denton. The 1993 IGTI Scholar Lecture: Loss Mechanisms in Turbomachines. *Journal of Turbomachinery*, 115(4):621–656, 1993.

S. L. Dixon and C. Hall. *Fluid Mechanics and Thermodynamics of Turbomachinery*. Butterworth-Heinemann, 7th edition, 2013.

J. Dunham and P. M. Came. Improvements to the ainley-mathieson method of turbine performance prediction. *Journal of Engineering for Power*, 92(3):252–256, 1970.

P. Forster, V. Ramaswamy, P. Artaxo, T. Berntsen, R. Betts, D. W. Fahey, J. Haywood, J. Lean, D. C. Lowe, G. Myhre, J. Nganga, R. Prinn, G. Raga, M. Schultz, and R. Van Dorland. Climate change 2007: The physical science basis. Contribution of Working Group I to the Fourth Assessment Report of the Intergovernmental Panel on Climate Change, 2007.

R. W. Fox, P. J. Pritchard, and A. T. McDonald. *Fox and McDonald's Introduction to Fluid Mechanics*. John Wiley & Sons, Inc., 9th edition, 2011.

E. N. Jacobs, K. E. Ward, and R. M. Pinkerton. The characteristics of 78 related airfoil sections from tests in the variable-density wind tunnel, 1933.

S. C. Kacker and U. Okapuu. A mean line prediction method for axial flow turbine efficiency. *Journal of Engineering for Power*, 104(1):111–119, 1982.

J. Larjola. Electricity from industrial waste heat using high-speed organic Rankine cycle. *International Joumal of Production Economics*, 41(28):227–235, 1995.

S. Lecompte, H. Huisseune, M. van den Broek, and M. De Paepe. Methodical thermodynamic analysis and regression models of organic Rankine cycle architectures for waste heat recovery. *Energy*, 87:60–76, 2015a.

S. Lecompte, H. Huisseune, M. Van Den Broek, B. Vanslambrouck, and M. De Paepe. Review of organic Rankine cycle (ORC) architectures for waste heat recovery. *Renewable and Sustainable Energy Reviews*, 47:448–461, 2015b.

E. W. Lemmon, M. L. Huber, and M. O. McLinden. NIST Standard Reference Database 23: Reference Fluid Thermodynamic and Transport Properties-REFPROP, Version 9.1, National Institute of Standards and Technology, 2013.

C. Li and H. Wang. Power cycles for waste heat recovery from medium to high temperature flue gas sources from a view of thermodynamic optimization. *Applied Energy*, 180: 707–721, 2016.

E. Macchi and M. Astolfi. *Organic Rankine Cycle (ORC) Power Systems: Technologies and Applications*. Woodhead Publising, 1st edition, 2016.

M. J. Moran and H. N. Shapiro. *Fundamentals of Engineering Thermodynamics*. John Wiley & Sons, 7th edition, 2011.

L. O. Nord. *Pre-combustion CO_2 capture: Analysis of integrated reforming combined cycle*. PhD thesis, Norwegian University of Science and Technology (NTNU), 2010.

S. Quoilin. *Sustainable Energy Conversion Through the Use of Organic Rankine Cycles for Waste Heat Recovery and Solar Applications*. PhD thesis, University of Liège, 2011.

S. Quoilin, M. V. D. Broek, S. Declaye, P. Dewallef, and V. Lemort. Techno-economic survey of organic rankine cycle (ORC) systems. *Renewable and Sustainable Energy Reviews*, 22:168–186, 2013.

H. I. H. Saravanamuttoo, G. F. C. Rogers, and H. Cohen. *Gas Turbine Theory*. Pearson Education, 6th edition, 2009.

M. Schobeiri. *Turbomachinery Flow Physics and Dynamic Performance*. Springer, 2nd edition, 2012.

G. Skaugen, A. Aasen, B. Hagen, and T. Viksand. Thermodynamic framework for cycle and component analysis and optimisation, 2016. To be published.

B. Sternlicht. Waste energy recovery: An excellent investment opportunity. *Energy Conversion and Management*, 22(4):361–373, 1982.

The MathWorks Inc. MATLAB version R2016a, 2016.

U.S Energy Information Administration. International Energy Statistics, 2016.

M. G. Zabetakis. Flammability characteristics of combustible gases and vapors, 1965.

H. Zhai, Q. An, L. Shi, V. Lemort, and S. Quoilin. Categorization and analysis of heat sources for organic Rankine cycle systems. *Renewable and Sustainable Energy Reviews*, 64:790–805, 2016.

Glossary

Angle, blade inlet

Angle between the tangent of the camber line at the leading edge and the axial direction.

Angle, blade outlet

Angle between the tangent of the camber line at the trailing edge and the axial direction.

Angle, deviation

Flow outlet angle minus the blade outlet angle.

Angle, flaring

Angle defined by the increase of blade height in the axial direction. Turbine flaring is required to accommodate density changes within the turbine.

Angle, flow inlet

Angle between the velocity vector and the axial direction at the leading edge of the blades.

Angle, flow outlet

Angle between the velocity vector and the axial direction at the trailing edge of the blades.

Angle, incidence

Flow inlet angle minus the blade inlet angle.

Angle, setting

Same as the stagger angle.

Angle, stagger

Angle between the chord line and the turbine axial direction.

Annulus

Annular duct defined by the the shroud and the hub surfaces.

Aspect ratio

Ratio of the blade height to the chord length of the blades.

Aspect ratio, axial

Ratio of the blade height to the axial chord length of the blades.

Back work ratio

Ratio of the input to output powers of a thermodynamic cycle.

Blade

Component of the turbine that deflects the flow. Stator blades deflect the flow to accelerate it and rotor blades accelerate the flow to extract work from it.

Blade height

Difference between the blade radius at the tip and the blade radius at the root.

Blade root

Section of the blade attached to the casing for stator blades (shroud) and to the disks for rotor blades (hub)..

Blade tip

End section of the blade. Rotor-blade tip sections are at the shroud and stator-blade tip sections are at the hub.

Camber

Distance between the camber line and the chord line, measured perpendicular to the chord line.

Camber length

Arc length of the camber line.

Camber line

Locus of points halfway between the suction and pressure surfaces.

Casing

Stationary part of the turbine that contains the rest of the components.

Chord length

Distance from the leading to the trailing edge.

Chord length, axial

Projection of the chord length onto a line parallel to the turbine axis.

Chord line

Straight line connecting the leading and the trailing edges.

Diaphragm

Extension of the stator blades located between the disks.

Disk

Rotating element of the turbine attached to the shaft where the rotor blades are mounted.

Edge, leading

Most forward point of the camber line.

Edge, trailing

Most rearward point of the camber line.

Fluid, dry

Substance with positive slope for the vapor saturation curve in the T–s diagram.

Fluid, isentropic

Substance with infinite slope for the vapor saturation curve in the T–s diagram.

Fluid, wet

Substance with negative slope for the vapor saturation curve in the T–s diagram.

Hub

Surface defining the inner diameter the flow, see shroud.

Hub to tip ratio

Ratio of the blade radius at the hub to the blade radius at the tip.

Pitch

Same as spacing.

Rankine cycle

Closed thermodynamic cycle where the working fluid is continuously vaporized and expanded to convert thermal energy into work.

Rankine cycle, organic

Rankine cycle that uses an organic substance as working fluid.

Rankine cycle, saturated

Rankine cycle in which the fluid at the inlet of the expander is a saturated vapor.

Rankine cycle, superheated

Rankine cycle in which the fluid at the inlet of the expander is a superheated vapor.

Rankine cycle, transcritical

Rankine cycle in which the fluid at the inlet of the expander is a supercritical gas.

Rotor

Ensemble of the rotating blades of the stage.

Shaft

Rotating element of the turbine that transmits the power from the rotor stages to the coupling with the load (electrical generator or propulsion system).

Shroud

Surface defining the outer diameter the flow, see hub.

Solidity

Inverse of the spacing to chord ratio.

Spacing

Distance in the circumferential direction between corresponding points of adjacent blades.

Spacing to chord ratio

Ratio of the axial chord to the spacing between blades of one cascade.

Spacing to chord ratio

Ratio of the chord to the spacing between blades of one cascade.

Stage

Combination of the stator and the rotor sections.

Stage spacing

Axial distance between the outlet of the stator stage and the inlet of the rotor stage.

Stator

Ensemble of the stationary blades of the stage. Stator blades are also known as nozzles.

Surface, pressure

Surface of the blade where pressure is high and velocity is low. The flow tends to be stable on this surface.

Surface, suction

Surface of the blade where the pressure is low and the velocity is high. The flow can be unstable in this region and separation may occur.

Thickness

Distance between the pressure and suction surfaces, measured perpendicular to the camber line.

Thickness, disk–casing clearance gap

Axial spacing that exists between the rotor disks and the stator diaphragms.

Thickness, maximum

Maximum the distance between the pressure and suction surfaces, measured perpendicular to the camber line.

Thickness, rotor clearance gap

Radial spacing that exists between the rotor tip and the casing.

Thickness, stator clearance gap

Radial spacing that exists between the diaphragm and the shaft.

Thickness, trailing edge

Distance between the pressure and suction surfaces at the trailing edge, measured perpendicular to the camber line.

Turbine

Machine that extracts energy from a fluid flow and converts it into useful work.

Turbine, axial

Turbine in which the flow is parallel to the shaft.

Turbine, hybrid

Turbine architecture that integrates radial inflow or outflow stages followed by one of more axial stages.

Turbine, radial inflow

Turbine in which the flow is in the radial inward direction.

Turbine, radial outflow

Turbine in which the flow is in the radial outward direction.

Waste heat

Thermal energy that cannot be use in any direct application that can be potentially transformed into work.

Appendix A

Working fluid characteristics

In this appendix, the characteristics of the working fluids considered in this work are summarized. The following information is presented for each fluid:

- Chemical name and alternative common name, as well as the chemical classification of the working fluid (organic-inorganic and class of organic fluid).
- The Ozone Depletion Potential (ODP) with respect to R11, as defined in the Montreal Protocol. The reported values were found in Daniel and Velders (2006) and Forster et al. (2007). If the ODP is not reported, it can be assumed to be negligible.
- The Global Warming Potential (GWP) over 100 years with respect to carbon dioxide. The reported values were found in Daniel and Velders (2006) and Forster et al. (2007). If the GWP is not reported, it can be assumed to be small.
- The flammability of the fluid, reporting the autoignition temperature (AIT) in case it is flammable. The values of autoignition temperatures were obtained from Zabetakis (1965) except for siloxanes that were obtained from *Dow Corning* safety reports.
- The ASHRAE safety classification for those fluids used in the refrigeration industry. This information was found in ASHRAE (2000).
- Thermophysical information of the fluids obtained from REFPROP, Lemmon et al. (2013), including: the molecular mass of the fluid, the critical temperature and pressure of the fluid, the melting temperature of the working fluid at an atmospheric pressure of 101.325 kPa, the saturation pressure of the fluid at an ambient temperature of 10 °C, and the temperature and pressure limits of the equations of state used by REFPROP.

Table A.1: Classification of working fluids according to their composition - First part.

Number	Chemical name	Alternative name	Class [a]	ODP	GWP	Flammability	Safety
1	Methane	R50	Alkane	n.a.	21.0	540.0	A3
2	Ethane	R170	Alkane	n.a.	5.5	515.0	A3
3	Propane	R290	Alkane	n.a.	3.3	450.0	A3
4	n-Butane	R600	Alkane	n.a.	4.0	405.0	A3
5	2-Methylpropane	Isobutane - R600a	Alkane	n.a.	n.a.	460.0	A3
6	Pentane	R601	Alkane	n.a.	n.a.	260.0	A3
7	2-Methylbutane	Isopentane-R601a	Alkane	n.a.	n.a.	420.0	A3
8	2,2-Dimethylpropane	Neopentane	Alkane	n.a.	n.a.	450.0	n.a.
9	Hexane	-	Alkane	n.a.	n.a.	225.0	n.a.
10	2-Methylpentane	Isohexane	Alkane	n.a.	n.a.	306.0	n.a.
11	Heptane	-	Alkane	n.a.	n.a.	215.0	n.a.
12	Octane	-	Alkane	n.a.	n.a.	220.0	n.a.
13	Nonane	-	Alkane	n.a.	n.a.	205.0	n.a.
14	Decane	-	Alkane	n.a.	n.a.	210.0	n.a.
15	Dodecane	-	Alkane	n.a.	n.a.	205.0	n.a.
16	Ethene	Ethylene - R1150	Alkene	n.a.	3.7	490.0	A3
17	Propene	Propylene - R1270	Alkene	n.a.	1.8	460.0	A3
18	1-Butene	Butene	Alkene	n.a.	n.a.	385.0	n.a.
19	Cis-2-butene	Cis-butene	Alkene	n.a.	n.a.	325.0	n.a.
20	Trans-2-butene	Trans-butene	Alkene	n.a.	n.a.	325.0	n.a.
21	2-Methyl-1-propene	Isobutene	Alkene	n.a.	n.a.	465.0	n.a.
22	Propyne	-	Alkyne	n.a.	n.a.	n.a.	n.a.
23	Cyclopropane	-	Cycloalkane	n.a.	n.a.	500.0	n.a.
24	Cyclopentane	-	Cycloalkane	n.a.	n.a.	n.a.	n.a.
25	Cyclohexane	-	Cycloalkane	n.a.	n.a.	245.0	n.a.
26	Methylcyclohexane	-	Cycloalkane	n.a.	n.a.	250.0	n.a.
27	n-Propylcyclohexane	-	Cycloalkane	n.a.	n.a.	n.a.	n.a.
28	Benzene	-	Aromatic	n.a.	n.a.	560.0	n.a.
29	Methylbenzene	Toluene	Aromatic	n.a.	2.7	480.0	n.a.
30	Trichlorofluoromethane	R11	CFC	1.000	4750.0	non flammable	A1
31	Dichlorodifluoromethane	R12	CFC	1.000	10890.0	non flammable	A1
32	Chlorotrifluoromethane	R13	CFC	1.000	14420.0	non flammable	A1
33	1,1,2-Trichloro-1,2,2-trifluoroethane	R113	CFC	0.800	6130.0	non flammable	A1
34	1,2-Dichloro-1,1,2,2-tetrafluoroethane	R114	CFC	1.000	10040.0	non flammable	A1
35	Chloropentafluoroethane	R115	CFC	0.600	7370.0	non flammable	A1
36	Dichlorofluoromethane	R21	HCFC	0.040	151.0	non flammable	B1
37	Chlorodifluoromethane	R22	HCFC	0.055	1810.0	non flammable	A1
38	2,2-Dichloro-1,1,1-trifluoroethane	R123	HCFC	0.020	77.0	non flammable	B1
39	1-Chloro-1,2,2,2-tetrafluoroethane	R124	HCFC	0.022	609.0	non flammable	A1
40	1,1-Dichloro-1-fluoroethane	R141b	HCFC	0.110	725.0	n.a.	n.a.
41	1-Chloro-1,1-difluoroethane	R142b	HCFC	0.065	2310.0	low flamability	A2
42	Trifluoromethane	R23	HFC	0.000	14760.0	non flammable	A1
43	Difluoromethane	R32	HFC	0.000	675.0	low flamability	A2
44	Fluoromethane	R41	HFC	0.000	92.0	n.a.	n.a.
45	Pentafluoroethane	R125	HFC	0.000	3500.0	non flammable	A1
46	1,1,1,2-Tetrafluoroethane	R134a	HFC	0.000	1430.0	non flammable	A1
47	1,1,1-Trifluoroethane	R143a	HFC	0.000	4470.0	low flamability	A2
48	1,1-Difluoroethane	R152a	HFC	0.000	124.0	low flamability	A2
49	Fluoroethane	R161	HFC	0.000	12.0	n.a.	n.a.
50	1,1,1,2,3,3,3-Heptafluoropropane	R227ea	HFC	0.000	3220.0	non flammable	A1
51	1,1,1,2,3,3-Hexafluoropropane	R236ea	HFC	0.000	1370.0	n.a.	n.a.
52	1,1,1,3,3,3-Hexafluoropropane	R236fa	HFC	0.000	9810.0	non flammable	A1
53	1,1,2,2,3-Pentafluoropropane	R245ca	HFC	0.000	693.0	n.a.	n.a.
54	1,1,1,3,3-Pentafluoropropane	R245fa	HFC	0.000	1030.0	non flammable	A1
55	1,1,1,3,3-Pentafluorobutane	R365mfc	HFC	0.000	794.0	n.a.	n.a.
56	2,3,3,3-Tetrafluoroprop-1-ene	R1234yf	HFO	0.000	4.0	n.a.	n.a.
57	Trans-1,3,3,3-tetrafluoropropene	R1234ze	HFO	0.000	6.0	n.a.	n.a.
58	Tetrafluoromethane	Perfluoromethane - R14	PFC	0.000	7390.0	non flammable	A1
59	Hexafluoroethane	Perfluoroethane - R116	PFC	0.000	12200.0	non flammable	A1
60	Octafluoropropane	Perfluoropropane - R218	PFC	0.000	8830.0	non flammable	A1
61	Octafluorocyclobutane	Perfluorocyclobutane - RC318	PFC	0.000	10030.0	n.a.	n.a.
62	Decafluorobutane	Perfluorobutane	PFC	0.000	8860.0	n.a.	n.a.
63	Dodecafluoropentane	Perfluoropentane	PFC	0.000	9160.0	n.a.	n.a.
64	Hexamethyldisiloxane	MM	Linear Siloxane	n.a.	n.a.	340.0	n.a.
65	Octamethyltrisiloxane	MDM	Linear Siloxane	n.a.	n.a.	340.0	n.a.
66	Decamethyltetrasiloxane	MD2M	Linear Siloxane	n.a.	n.a.	350.0	n.a.
67	Dodecamethylpentasiloxane	MD3M	Linear Siloxane	n.a.	n.a.	350.0	n.a.
68	Tetradecamethylhexasiloxane	MD4M	Linear Siloxane	n.a.	n.a.	350.0	n.a.
69	Octamethylcyclotetrasiloxane	D4	Cyclid siloxane	n.a.	n.a.	370.0	n.a.
70	Decamethylcyclopentasiloxane	D5	Cyclid siloxane	n.a.	n.a.	372.0	n.a.
71	Dodecamethylcyclohexasiloxane	D6	Cyclid siloxane	n.a.	n.a.	370.0	n.a.
72	Propanone	Acetone	Ketone	n.a.	0.5	465.0	n.a.
73	Ethyl alcohol	Ethanol	Alcohol	n.a.	n.a.	365.0	n.a.
74	Methanol	Methanol	Alcohol	n.a.	2.8	385.0	n.a.
75	Dimethyl ester carbonic acid	Dimethyl carbonate	Carbonate ester	n.a.	n.a.	n.a.	n.a.
76	Trifluoroiodomethane	-	Haloalkane	n.a.	n.a.	n.a.	n.a.
77	Methoxymethane	Dimethylether	Ether	n.a.	n.a.	350.0	n.a.
78	Ammonia	R717	Inorganic	0.000	0.0	low flamability	B2
79	Carbon dioxide	R744	Inorganic	0.000	1.0	non flammable	A1
80	Water	R718	Inorganic	0.000	0.0	non flammable	A1

[a] Chlorofluorocarbon (CFC), hydrochlorofluorocarbon (CFC), hydrofluorocarbon (HFC), hydrofluoroolefin(HFO), perfluorocarbon (PFC).

Table A.2: Classification of working fluids according to their composition - Second part.

Number	Alternative name	MW (kg/kmol)	T_{crit} (K)	p_{crit} (kPa)	T_{melt} (K)	p_{sat} (kPa)	T_{min} (K)	T_{max} (K)	p_{max} (MPa)
1	R50	16.04	190.56	4599.20	90.72	n.a.	90.69	625.00	1000.00
2	R170	30.07	305.32	4872.20	90.38	3017.25	90.37	675.00	900.00
3	R290	44.10	369.89	4251.20	85.53	636.60	85.53	650.00	1000.00
4	R600	58.12	425.13	3796.00	134.91	148.45	134.90	575.00	69.00
5	Isobutane - R600a	58.12	407.81	3629.00	113.77	220.61	113.73	575.00	35.00
6	R601	72.15	469.70	3370.00	143.48	37.83	143.47	600.00	100.00
7	Isopentane-R601a	72.15	460.35	3378.00	112.66	52.31	112.65	500.00	1000.00
8	Neopentane	72.15	433.74	3196.00	256.60	103.15	256.60	550.00	200.00
9	-	86.18	507.82	3034.00	177.83	10.11	177.83	600.00	100.00
10	Isohexane	86.18	497.70	3040.00	119.60	14.60	119.60	550.00	1000.00
11	-	100.20	540.13	2736.00	182.55	2.75	182.55	600.00	100.00
12	-	114.23	569.32	2497.00	216.37	0.75	216.37	600.00	100.00
13	-	128.26	594.55	2281.00	219.70	0.21	219.70	600.00	800.00
14	-	142.28	617.70	2103.00	243.50	0.06	243.50	675.00	800.00
15	-	170.33	658.10	1817.00	263.60	0.00	263.60	700.00	700.00
16	Ethylene - R1150	28.05	282.35	5041.80	104.00	n.a.	103.99	450.00	300.00
17	Propylene - R1270	42.08	364.21	4555.00	87.96	778.60	87.95	575.00	1000.00
18	Butene	56.11	419.29	4005.10	87.80	183.52	87.80	525.00	70.00
19	Cis-butene	56.11	435.75	4225.50	134.30	127.97	134.30	525.00	50.00
20	Trans-butene	56.11	428.61	4027.30	n.a.	141.72	167.60	525.00	50.00
21	Isobutene	56.11	418.09	4009.80	132.40	188.42	132.40	550.00	50.00
22	-	40.06	402.38	5626.00	n.a.	369.25	273.00	474.00	32.00
23	-	42.08	398.30	5579.70	n.a.	472.18	273.00	473.00	28.00
24	-	70.13	511.69	4515.00	179.72	22.61	179.72	600.00	200.00
25	-	84.16	553.64	4075.00	279.52	6.35	279.47	700.00	80.00
26	-	98.19	572.20	3470.00	146.70	2.87	146.70	600.00	500.00
27	-	126.24	630.80	2860.00	178.20	0.21	178.20	650.00	50.00
28	-	78.11	562.02	4906.30	278.67	6.07	278.70	750.00	500.00
29	Toluene	92.14	591.75	4126.30	178.00	1.67	178.00	700.00	500.00
30	R11	137.37	471.11	4407.64	162.68	60.68	162.68	625.00	30.00
31	R12	120.91	385.12	4136.10	116.10	422.67	116.10	525.00	200.00
32	R13	104.46	302.00	3879.00	92.00	2515.36	92.00	403.00	35.00
33	R113	187.38	487.21	3392.20	236.93	23.93	236.93	525.00	200.00
34	R114	170.92	418.83	3257.00	n.a.	128.57	273.15	507.00	21.00
35	R115	154.47	353.10	3129.00	173.75	597.02	173.75	550.00	60.00
36	R21	102.92	451.48	5181.20	n.a.	105.88	200.00	473.00	138.00
37	R22	86.47	369.30	4990.00	115.73	680.95	115.73	550.00	60.00
38	R123	152.93	456.83	3661.80	166.00	50.57	166.00	600.00	40.00
39	R124	136.48	395.43	3624.30	n.a.	234.14	120.00	470.00	40.00
40	R141b	116.95	477.50	4212.00	n.a.	43.50	169.68	500.00	400.00
41	R142b	100.50	410.26	4055.00	142.72	207.21	142.72	470.00	60.00
42	R23	70.01	299.29	4832.00	118.02	3243.84	118.02	475.00	120.00
43	R32	52.02	351.26	5782.00	n.a.	1106.91	136.34	435.00	70.00
44	R41	34.03	317.28	5897.00	129.82	2658.95	129.82	425.00	70.00
45	R125	120.02	339.17	3617.70	172.52	908.75	172.52	500.00	60.00
46	R134a	102.03	374.21	4059.28	169.85	414.61	169.85	455.00	70.00
47	R143a	84.04	345.86	3761.00	161.34	836.28	161.34	650.00	100.00
48	R152a	66.05	386.41	4516.75	154.56	372.77	154.56	500.00	60.00
49	R161	48.06	375.30	5091.00	130.00	600.57	130.00	400.00	50.00
50	R227ea	170.03	374.90	2925.00	146.35	279.57	146.35	475.00	60.00
51	R236ea	152.04	412.44	3501.98	n.a.	118.02	242.00	500.00	60.00
52	R236fa	152.04	398.07	3200.00	179.52	159.72	179.52	500.00	40.00
53	R245ca	134.05	447.57	3925.00	n.a.	54.68	200.00	500.00	60.00
54	R245fa	134.05	427.16	3651.00	171.05	82.04	171.05	440.00	200.00
55	R365mfc	148.07	460.00	3266.00	239.00	29.76	239.00	500.00	35.00
56	R1234yf	114.04	367.85	3382.20	220.00	437.53	220.00	410.00	30.00
57	R1234ze	114.04	382.52	3636.25	168.62	308.33	168.62	420.00	20.00
58	Perfluoromethane - R14	88.01	227.51	3750.00	n.a.	n.a.	120.00	623.00	51.00
59	Perfluoroethane - R116	138.01	293.03	3048.00	173.10	2385.31	173.10	425.00	50.00
60	Perfluoropropane - R218	188.02	345.02	2640.00	125.45	566.36	125.45	440.00	20.00
61	Perfluorocyclobutane - RC318	200.04	388.38	2777.50	n.a.	187.82	233.35	623.00	60.00
62	Perfluorobutane	238.03	386.33	2323.40	n.a.	160.76	189.00	500.00	30.00
63	Perfluoropentane	288.03	420.56	2045.00	n.a.	45.67	148.36	500.00	30.00
64	MM	162.38	518.70	1939.39	n.a.	2.44	273.00	673.00	30.00
65	MDM	236.53	564.09	1415.00	187.20	0.1735	187.20	673.00	30.00
66	MD2M	310.69	599.40	1227.00	205.20	0.0160	205.20	673.00	30.00
67	MD3M	384.84	628.36	945.00	n.a.	0.0015	192.00	673.00	30.00
68	MD4M	458.99	653.20	877.47	n.a.	n.a.	300.00	673.00	30.00
69	D4	296.62	586.49	1332.00	n.a.	n.a.	300.00	673.00	30.00
70	D5	370.77	619.23	1161.46	n.a.	n.a.	300.00	673.00	30.00
71	D6	444.92	645.78	961.00	270.20	0.0007	270.20	673.00	30.00
72	Acetone	58.08	508.10	4700.00	178.50	15.45	178.50	550.00	700.00
73	Ethanol	46.07	513.90	6148.00	n.a.	3.18	250.00	650.00	280.00
74	Methanol	32.04	513.38	8215.85	175.63	7.44	175.61	620.00	800.00
75	Dimethyl carbonate	90.08	557.38	4835.08	n.a.	3.24	277.06	400.00	60.00
76	-	195.91	396.44	3953.00	120.00	315.56	120.00	420.00	20.00
77	Dimethylether	46.07	400.38	5336.85	n.a.	373.35	131.65	525.00	40.00
78	R717	17.03	405.40	11333.00	195.50	615.05	195.50	700.00	1000.00
79	R744	44.01	304.13	7377.30	n.a.	4502.18	216.59	2000.00	800.00
80	R718	18.02	647.10	22064.00	n.a.	1.23	273.16	2000.00	1000.00